

NORTHWESTERN UNIVERSITY

Growth, Structure and Catalytic Properties of  
Pd Nanoparticles Supported on SrTiO<sub>3</sub> Nanopolyhedra

A DISSERTATION

SUBMITTED TO THE GRADUATE SCHOOL  
IN PARTIAL FULFILLMENT OF THE REQUIREMENTS

for the degree

DOCTOR OF PHILOSOPHY

Field of Materials Science and Engineering

By

Bor-Rong Chen

EVANSTON, ILLINOIS

April 2017

© Copyright by Bor-Rong Chen 2017

All Rights Reserved

## ABSTRACT

### **Growth, Structure and Catalytic Properties of Pd Nanoparticles Supported on SrTiO<sub>3</sub> Nanopolyhedra**

Bor-Rong Chen

The influence of the “metal-support interaction” on catalytic activity has received much attention during the past decades. This interest in the metal-support interaction is driven by the potential to increase the catalytic activity and reduce the amount of metal required to carry out the catalysis effectively. The primary objective of this dissertation is to employ single crystal SrTiO<sub>3</sub> (STO) nanoparticles with atomically-flat facets and sufficiently high surface-to-volume ratio as catalyst supports. This will bridge the gap between surface science studies and practical catalytic studies, and allow these studies to be carried out simultaneously. Specifically, this work compares Pd nanoparticles grown by atomic layer deposition (ALD) on three types of STO nanopolyhedra supports: TiO<sub>2</sub>-(001)-terminated nanocuboids, SrO-(001)-terminated nanocuboids, and (110)-terminated nanododecahedra. In particular, this dissertation focuses on using an X-ray mediated approach to study the structure of the Pd nanoparticles at the atomic level. This allows the structures of the Pd nanoparticles to be related to their catalytic performance.

Transmission electron microscopy (TEM) and small-angle X-ray scattering (SAXS) show that the ALD-Pd nanoparticles decorating the STO surfaces have an average diameter ranging from 2 to 5 nm and interparticle distance ranging from 3 to 5 nm, depending on the number of

ALD cycles. With increased Pd loading, the Pd nanoparticles grow in number on the SrO-(001)-STO and (110)-STO surfaces and grow in size on the TiO<sub>2</sub>-(001)-STO surface. The Pd nanoparticles exhibit a lower degree of wetting on the SrO-(001)-STO surface than on the TiO<sub>2</sub>-(001)-STO and (110)-STO surfaces.

CO oxidation was employed as a probe reaction to establish the relationship between the surface morphology and catalytic activity for Pd supported on TiO<sub>2</sub>-(001)-terminated nanocuboids and (110)-terminated nanododecahedra. CO turnover frequency (TOF) and diffuse reflectance infrared Fourier transform spectroscopy (DRIFTS) show that regardless of the shape, relatively large Pd nanoparticles (~ 3 nm) have lower TOF because of CO poisoning on the facets. In contrast, smaller nanoparticles (~ 2 nm) with more edge and corner sites exhibit two to three times higher TOF. Overall, this dissertation demonstrates that the ensemble of Pd on STO nanopolyhedra can bridge the materials gap between single crystal and powder catalyst supports. Thereby, this research is able to establish the influence of the support effect on the morphology of Pd nanoparticles and catalytic activity.

## ACKNOWLEDGEMENTS

To begin, I would like to thank my advisor, Prof. Michael Bedzyk, for being patient and supportive. Mike is an excellent teacher, and I thank him for guiding me over the past five years at Northwestern University. I am especially grateful for the flexibility and patience he has shown towards me. I have been privileged to be able work with my collaborators and committee members: Prof. Peter Stair, Prof. Laurence Marks and Prof. Kenneth Poepelmeier. I would like to thank them for spending time and effort in my project. My discussions with them are always fruitful, and I really appreciate their feedback and suggestions.

I also want to acknowledge my funding sources. My thesis work was funded by the Institute for Catalysis in Energy Process (ICEP) at Northwestern University under US Department of Energy (DOE) grant DE-FG02-03ER15457. I personally received the Study Abroad Fellowship from Ministry of Education of Taiwan from 2013 to 2015. I am thankful to have been well-funded during my graduate research.

The research discussed in this thesis would not have been possible without my collaborators. I thank Lawrence Crosby, Dr. Cassie George, Dr. Yuyuan Lin, Dr. Linha Hu, Dr. Robert Kennedy, Dr. Aidan Mouat, and Cassey Whitford. I appreciate their effort in helping me synthesize high quality samples and collecting electron microscope images. I would like to acknowledge the support from the staff at DND-CAT during my beamtimes: Dr. Denis Keane, Dr. Qing Ma, and Dr. Steve Weigand. I also thank Prof. Neil Schweitzer for training me on instruments at the Clean Catalysis Core Facility.

It has been a great journey with the members in the Bedzyk's Group for my five years here. I am glad to have had Dr. Jon Emery, Dr. Curtis Leung, Dr. Sven Stoltz, and Dr. Sumit Kewalramani as mentors while starting my PhD life. They gave me so much advice on research

and career development. I have greatly benefited from Gavin Campbell, Stephanie Moffitt, Kathy Harmon, Liane Moreau, Kurinji Krishnamoorthy, Li Zeng, Xiao Chen, Changrui Gao, Boris Harutyunyan, Bo-Hong Liu, and Guenna Evmenenko, for their friendships and discussions. Words cannot describe how grateful I am to Stephanie, Kathy, Kurinji, Gavin, Sumit, Bo-Hong and Liane, for their continuous support and encouragement during thesis writing and editing.

I met so many wonderful people in Evanston. It was a pleasure to play volleyball every Saturday morning for three years with Chieh-Chao, Wei-Tsung, Yun-Chu, Chia-Yun, Wei-Shin, Chi-Shiang and other teammates. I cannot thank my roommate Yu-Han enough for taking care of me like my big sister since my first year here. It was a pleasure to share the joys and sorrows with Chya-Yen and Che-Ning. My time at Northwestern was also enriched by Matt, Cam, Lauren, Emily, Sarah, and other folks in MatSci. It was such an interesting experience hanging out and learning American cultures from them.

Finally, I would thank my husband Jia-Hong, I am really happy that I had met him ten years ago in the lab as an REU student. I am so grateful to him for encouraging me to pursue this PhD degree overseas. I am looking forward to the life together with him.

**LIST OF ABBREVIATIONS**

ALD	atomic layer deposition
DRIFTS	diffuse reflectance infrared spectroscopy
EXAFS	extended X-ray absorption fine structure
HAADF	high angle annular dark field
PGM	Platinum group metal
STO	SrTiO <sub>3</sub> , Strontium titanate
TEM	transmission electron microscopy
SAXS	Small-angle X-ray scattering
XAS	X-ray absorption spectroscopy
XANES	X-ray absorption near edge spectroscopy
XRF	X-ray fluorescence
XPS	X-ray photoelectron spectroscopy

**TABLE OF CONTENTS**

<b>ABSTRACT</b> .....	3
<b>ACKNOWLEDGEMENTS</b> .....	5
<b>LIST OF ABBREVIATIONS</b> .....	7
<b>LIST OF FIGURES</b> .....	15
<b>LIST OF TABLES</b> .....	31
Chapter 1: Introduction .....	33
1.1 Motivation.....	33
1.2 Outline.....	35
Chapter 2: Background .....	36
2.1 Metal-Oxide Support Interface in Heterogeneous Catalysis .....	36
2.1.1 Introduction of Catalysis.....	36
2.1.2 Importance of the Metal-Oxide Support Interface in Heterogeneous Catalysts ..	41
2.1.3 Model Catalysts and Materials Gap.....	43
2.2 Materials .....	44
2.2.1 Introduction.....	44
2.2.2 Overview of SrTiO <sub>3</sub> .....	45

2.2.3 Faceted Shapes of Pd (Pt) Nanocrystals on STO Single Crystal Surfaces .....	47
2.2.4 STO Nanopolyhedra Supports .....	50
2.2.5 Atomic Layer Deposition (ALD) Growth of Metals.....	54
2.2.6 ALD-Pt on STO Single Crystal Surfaces and Nanopolyhedra Supports .....	56
2.3 Correlating Nanoparticle Shape with Catalytic Performance .....	58
2.3.1 Winterbottom Construction Shapes .....	58
2.3.2 CO Oxidation as an Activity Probe.....	62
Chapter 3: Synthesis and Characterization Techniques .....	65
3.1 Hydrothermal Synthesis.....	65
3.2 Atomic Layer Deposition (ALD) .....	66
3.3 X-ray Characterization Techniques.....	66
3.3.1 Introduction.....	66
3.3.2 Small Angle X-ray Scattering (SAXS) .....	67
3.3.3 X-ray Absorption Spectroscopy (XAS) .....	70
3.3.4 X-ray Fluorescence (XRF).....	76
3.3.5 X-ray Photoelectron Spectroscopy (XPS) .....	77
3.4 Other Characterization Techniques .....	79

3.4.1 Transmission electron microscopy (TEM) and high resolution electron microscopy (HREM).....	79
3.4.2 Diffuse Reflectance Infrared Fourier Transform Spectroscopy (DRIFTS) .....	79
3.4.3 Metal Dispersion of Pd Nanoparticles .....	81
3.4.4 Turnover Frequency of the CO Oxidation Reaction .....	83
Chapter 4: Morphological and Chemical Evolution of Pd Nanoparticles Supported on SrTiO <sub>3</sub> Nanocuboids .....	85
4.1 Introduction.....	85
4.2 Experimental Methods .....	85
4.2.1 Sample Preparation .....	85
4.2.2 Morphology and Loading of Pd.....	87
4.2.3 XANES and EXAFS Measurements .....	88
4.2.4 X-ray Photoelectron Spectroscopy Analysis.....	89
4.3 Results and Discussion .....	90
4.3.1 Morphology.....	90
4.3.2 Pd Loading and Effective Coverage .....	94
4.3.3 Chemical State and Local Structure Analysis .....	97

4.3.4 In-situ EXAFS Measurements of $N_{Pd-Pd}$ under Reduction Conditions .....	103
4.3.5 Mechanism of ALD-Pd Nanoparticle Growth on TiO <sub>2</sub> - and SrO-STO Surfaces .....	107
4.3.6 In-situ XANES Measurements of Pd/STO under Redox Environment.....	111
4.4 Summary.....	112
Chapter 5: Morphology and CO Oxidation Activity of Pd Nanoparticles Supported on SrTiO <sub>3</sub>	
Nanopolyhedra.....	114
5.1 Introduction.....	114
5.2 Materials and Methods.....	115
5.2.1 Sample Preparation .....	115
5.2.2 Electron Microscopy .....	115
5.2.3 Small-Angle X-ray Scattering (SAXS).....	116
5.2.4 Inductively Coupled Plasma Atomic Emission Spectroscopy (ICP-AES) and X-ray fluorescence (XRF).....	116
5.2.5 X-ray Absorption Near Edge Structure (XANES).....	117
5.2.6 Metal Dispersion and CO Oxidation Reaction Measurements .....	117
5.2.7 Diffuse Reflectance Infrared Fourier Transform Spectroscopy (DRIFTS) .....	118

	12
5.3 Results and Discussions.....	119
5.3.1 Morphology of ALD-Pd.....	119
5.3.2 Loading and Coverage of Pd.....	126
5.3.3 XANES Determination of the Pd <sup>0</sup> Atomic Fraction .....	129
5.3.4 CO Oxidation Activity .....	131
5.4 Summary .....	137
Chapter 6: Synthesis and Characterization of the STO Nanopolyhedra.....	139
6.1 Introduction.....	139
6.2 Acetic Acid-Assisted Synthesis of TiO <sub>2</sub> -(001)-STO Nanocuboids.....	140
6.2.1 Background and Synthesis.....	140
6.2.2 Characterization and Discussion.....	140
6.3 Oleic Acid-Assisted Synthesis of SrO-(001)-STO Nanocuboids .....	143
6.3.1 Background and Synthesis.....	143
6.3.2 Characterization .....	143
6.4 Alternative Methods for Synthesizing Surfactant-Free SrO-(001)-STO Nanocuboids	144
6.4.1 Background .....	144
6.4.2 Short Carboxylic Acid Synthesis .....	145

	13
6.4.3 Octanoic Acid-Butanol Synthesis .....	149
6.5 Glycerol-Assisted Synthesis of (110)-STO Nanododecahedra.....	154
6.5.1 Background .....	154
6.5.2 Synthesis .....	155
6.5.3 Characterization .....	156
6.5.4 Results and Discussion .....	156
6.6 Summary .....	162
Chapter 7: In-situ XAS Study of the Reduction of Pd Surface Complex Supported on $\gamma$ -Al <sub>2</sub> O <sub>3</sub>	163
7.1 Introduction.....	163
7.2 Synthesis .....	165
7.3 Characterization Methods .....	165
7.4 Results and Discussion .....	166
7.5 Summary .....	168
Chapter 8: Conclusions and Future Directions .....	169
8.1 Conclusions.....	169
8.2 Future Directions .....	171
8.2.1 Pd Supported on SrTiO <sub>3</sub> Single Crystal Surface .....	171

	14
8.2.2 Various Metal/ABO <sub>3</sub> Nanopolyhedra Catalytic System .....	172
APPENDIX.....	173
Appendix A: An Operation Manual for XAS Measurements .....	173
A.1 XAS Measurement at the 5BM-D Beamline at the APS .....	173
A.2 Data Reduction Procedures .....	180
A.3 In-situ Flow Cells and the Gas Manifold System .....	184
Appendix B: Data Analysis and Calculations .....	188
B.1 XRF Determined Pd/Sr Atomic Ratio .....	188
B.2 Pd/STO Surface Composition Determined from XPS .....	191
B.3 XAS Determined Pd to PdO Ratio .....	192
B.4 SAXS Determined Pd Interparticle Distance .....	193
B.5 Metal Dispersion of Pd Nanoparticles .....	195
B.6 CO Oxidation Turnover Frequency Calculation .....	197
REFERENCES .....	199

## LIST OF FIGURES

Figure 2.1 Schematic diagram illustrating the progress of a chemical reaction with and without the presence of a catalyst. (Source: adapted from Ref. [57]).....	38
Figure 2.2 The Price history of Pt and Pd from March 2008 to March 2017. (Source: <a href="http://www.apmex.com/spotprices/">http://www.apmex.com/spotprices/</a> [62]).....	41
Figure 2.3 Evolution of model catalyst systems with increasing complexity towards the real-world catalysts (Source: adapted from Ref. [23]).....	44
Figure 2.4 A unit cell of cubic SrTiO <sub>3</sub> . The green, red, and blue balls represent Sr, O, and Ti atoms, respectively.....	46
Figure 2.5 From Silly and Castell [37], 140 x 140 nm <sup>2</sup> scanning tunneling microscopy (STM) images with insets showing 3D renderings of the NP shapes (a-c) and the models (d-f) of the Pd nanocrystals supported on the (001)-STO single crystal surface. (a, d) Hut-shaped Pd grown on a (2 × 1) surface at room temperature followed by 650 °C annealing. (b, e) Hexagonal-shaped Pd grown on a c(4 × 2) substrate at room temperature followed by 650 °C annealing. (c, f) Pyramid-shaped Pd grown on a c(4 × 2) substrate at 460 °C followed by 650 °C annealing. (Source: (a-c) adapted from Ref. [37], and (d-f) adapted from Ref. [38].).....	48

Figure 2.6 Scanning electron microscopy (SEM) images of Pt nanocrystal arrays supported on (a) (100), (b) (110), and (c) (111) single crystal surfaces of STO. Insets on the right are close-up top and side views, and insets on the left are the 3D models of the Pt nanocrystal. The Pt nanocrystals are located on 200 nm square lattices. (Source: adapted from Ref. [30]) ..... 49

Figure 2.7 An example of the metal/oxide nanopolyhedra catalytic system. (a) The SrTiO<sub>3</sub> nanopolyhedra under scanning electron microscopy (Hitachi SU8030). (b) Pd nanoparticles supported on SrTiO<sub>3</sub> nanopolyhedra under transmission electron microscopy (Hitachi 2300A S/TEM). (c) Close-up of a facet in (b), showing that the facet resembles the surface of a single crystal support catalyst. (TEM images in (b) and (c) were provided by L.A. Crosby. The electron microscopy works made use of the EPIC facility in NUANCE Center of Northwestern University.)52

Figure 2.8 TEM images of various types of STO nanopolyhedra. (a) TiO<sub>2</sub>-terminated (001)-STO nanocuboids, (b) SrO-terminated (001)-STO nanocuboids (Source: Ref. [44]), (c) Mix-terminated (001)-STO nanocuboids (Source: Ref. [70]), and (d) (110)-STO nanododecahedra (Source: Ref. [45]). More details of the synthesis of nanopolyhedra are presented in Chapter 6..... 53

Figure 2.9 A schematic model of a general ALD binary reaction sequence. Two precursors are sequentially introduced to a substrate surface with inert gas purging in between. (a) Pulsing of the first precursor and formation of active sites reaction byproducts, (b) Purging of byproducts and unreacted precursors, (c) Pulsing of the second precursor, and (d) Purging of by-products and the second precursor, which are unreacted. The process of (a-d) is referred to as an "ALD cycle." ..... 56

Figure 2.10 (a) SEM images of 15, 20, 30, 40, and 80 cycles of Pt ALD on an STO(001) single crystal support. Pt nanoparticles nucleate, grow and coalesce with increasing ALD cycles. Film closure occurs at 40 ALD cycles. (b) SEM images of TiO<sub>2</sub>-(001)-STO nanocuboids before and after 3 cycles of Pt ALD deposition. Pt disperses uniformly on all exposed surfaces of the STO nanocuboids. (Source: (a) and (b) adapted from Ref. [31] and [24], respectively.)..... 58

Figure 2.11 (a) Diagram for generating the Wulff shape of a crystal. Each red vector is constructed along an  $hkl$  surface normal direction with a length proportional to the surface energy. The dashed lines are vector end points in variable directions. The inner envelope (thin blue lines) of these perpendicular planes defines the thermodynamic equilibrium crystal shape (thick black lines).  $\gamma_{(001)}$  and  $\gamma_{(111)}$  are

the surface energies of Pd (001) and (111). (Source: adapted from Refs. [93] and [94]). (b) A 3D model of the Wulff shape of Pd generated by Wulff Maker [95] based on the surface energies of Pd calculated in Ref. [96] (1.64 and 1.86 J/m<sup>2</sup> for Pd(111) and (001)). ..... 59

Figure 2.12 (a) Schematic of the variation in the shape of a Pd (or Pt) nanoparticle with (001) epitaxy on the surface, as a function of effective interfacial free energy ( $\gamma_{Int}$ ). From left to right is the nanoparticle shows dewetting to wetting. The (111) and (001) facets of Pd are marked by orange and purple, respectively (Source: adapted from Ref. [93]). (b) HREM image of Pt nanoparticles supported on STO(001) surface of a TiO<sub>2</sub>-(001)-STO nanocuboid. The red frame shows the Winterbottom shape of the Pt nanoparticles. (Source: adapted from Ref. [69])... 61

Figure 2.13 The objective of this dissertation..... 62

Figure 2.14 Schematic illustrations of the steps of CO oxidation over PGM surface: (a)  $\text{CO(g)} + * \rightleftharpoons \text{CO(ads)}$ . (b)  $\text{O}_2\text{(g)} + 2* \rightleftharpoons 2\text{O}^*\text{(ads)}$ . (c)  $\text{O}^*\text{(ads)} + \text{CO}^*\text{(ads)} \rightleftharpoons \text{CO}_2^*\text{(ads)}$ . (d)  $\text{CO}_2^*\text{(ads)} \rightleftharpoons \text{CO}_2\text{(g)}$  (Source: adapted from [57]). ..... 63

Figure 3.1 (a) Schematic diagram explaining the principle of XAS. The solid circle represents the wave function of the photoelectron produced during X-ray

absorption. The dashed circles represent a further contribution when the photoelectron being scattered by the neighboring atoms. The interference between the initial and the scattered wave functions causes the oscillations in the EXAFS region. (b) A typical XAFS spectrum of a Pd foil at the Pd K-edge (24.35 keV).

The XANES and EXAFS regions are identified in the figure. .... 71

Figure 3.2 Schematic illustrations of the top-views of the two measurement modes of XAS. (a) Transmission mode and (b) Fluorescence mode. The monochromator consists of a pair of Si(111) single crystals that are scanned at an incident angle to scan the desired XAS energy range. Note that in the fluorescence mode, the X-ray fluorescence is collected in a direction parallel to the polarization direction to minimize the count-rate of elastic and inelastic scattered X-rays in the fluorescence detector. Because the synchrotron radiation is polarized in the horizontal plane, the X-ray fluorescence detector is set up at  $90^\circ$  angle to the incident beam in the horizontal plane to minimize the intensity from elastically scattered X-rays. Additionally, the sample is placed such that the beam incidence and exit angles are both  $45^\circ$ . .... 75

Figure 3.3 The schematic illustration of the interaction between an incident X-ray and an atom producing an emitted photoelectron followed by an X-ray fluorescent photon. ....	77
Figure 3.4 A schematic diagram of IR interacting with powder and generating diffuse reflection (Source: adapted from Ref. [112])......	81
Figure 3.5 Setup of the CO oxidation reaction: (a) The BenchCAT 4000 reactor system. (b) Schematic illustration of the plug flow reactor. ....	84
Figure 4.1 (a, b) Size distribution and (c, d) BET absorption curve for TiO <sub>2</sub> -terminated and SrO-terminated STO nanocuboids. ....	86
Figure 4.2 TEM and HAADF images of TiO <sub>2</sub> -terminated (a-e) and SrO-terminated SrTiO <sub>3</sub> (f-i) nanocuboids before and after ALD Pd deposition. Pd nanoparticles can be clearly seen from the images. HRTEM images in (j) and (k) show the details of the faceted Pd nanoparticles on TiO <sub>2</sub> -terminated and SrO-terminated STO surfaces. A better wetting between Pd and the TiO <sub>2</sub> -STO surface can be observed. (Images were taken by: (a-e) Yuyuan Lin, (f-i) Linhua Hu, (j, k) Lawrence A. Crosby.) .....	91

Figure 4.3 (a) Definition of the aspect ratio of a schematic Pd nanoparticle. (b-e)

Distribution of the aspect ratio of Pd nanoparticles on TiO<sub>2</sub>-terminated STO surface (b, c) and on SrO-terminated STO surface (d, e). ..... 92

Figure 4.4 Histograms of Pd nanoparticle diameters extracted from TEM images: size

distribution of 5c Pd/TiO<sub>2</sub>-STO (a), 10c Pd/TiO<sub>2</sub>-STO (b), 5c Pd/SrO-STO (d), and 10c Pd/SrO-STO (e). The mean diameter (d) and standard deviation (SD) values are included in the figure. Schematic representations of the morphology and evolution of Pd nanoparticles on TiO<sub>2</sub>- and SrO-terminated STO surface are shown in (c) and (f), respectively..... 94

Figure 4.5 Effective Pd coverage ( $\theta$ ) increases almost linearly as the number of ALD

cycles increases. One monolayer ( $\theta = 1\text{ML}$ ) coverage is defined as the 2D density of Sr atom in a SrO (001) atomic plane of STO ( $6.56 \text{ nm}^{-2}$ ). ..... 95

Figure 4.6 The Pd 3d core level peak of the Pd/STO samples along with the reference

spectra of Pd<sup>0</sup> and Pd<sup>2+</sup>, showing the position of Pd 3d shifts to the low BE region as the Pd loading increases. .... 97

Figure 4.7 (a) The Pd K-edge X-ray absorption spectra for the ALD-Pd/STO samples

with different numbers of ALD cycles. The Pd K-edge of a Pd foil (Pd<sup>0</sup>) and PdO

(Pd<sup>2+</sup>) powder references are shown for comparison. (b) Fourier transform magnitudes of  $k^2$ -weighted Pd K-edge EXAFS spectra, along with the corresponding first shell fit (red lines). Pd–O and Pd–Pd first shell coordination numbers can be extracted from the best fit of the EXAFS data. (c) The unit cells of face-centered cubic metallic Pd and tetragonal Pd oxide (PdO) as determined by X-ray crystallography. The scattering paths (Pd–Pd and Pd–O) used in EXAFS fitting are indicated by the green arrows..... 99

Figure 4.8 Atomic phase fraction of Pd<sup>0</sup> ( $fPd0$ ) in Pd nanoparticles with the number of ALD cycles.  $fPd0$  increases monotonically as the number of ALD cycles increases; and  $fPd0$  is higher on the SrO-STO surface at the same number of ALD cycles. .... 101

Figure 4.9 First shell coordination number of Pd ( $N_{Pd-Pd}$ ) extracted from the *in-situ* EXAFS measurement as a function of the number of ALD cycles. The measurements were performed after the residual Pd oxide on the Pd/STO samples was removed under flowing H<sub>2</sub> at 300 °C for 30 min. .... 104

Figure 4.10 Fourier transform magnitudes of  $k^2$ -weighted Pd K-edge EXAFS spectra of the reduced Pd/STO samples, along with the corresponding first shell fit (red

lines). Pd–O and Pd–Pd first shell coordination numbers can be extracted from the best fit of the EXAFS data (Table 4.5). ..... 105

Figure 4.11 (a) X-ray photoelectron spectra of F 1s peaks of the Pd/TiO<sub>2</sub>-STO and Pd/SrO-STO samples. (b) The atomic ratio between F and surface Sr atoms. The inserted image in 7(b) shows the structure of a Pd(hfac)<sub>2</sub> molecule, which has 12 fluorine atoms. .... 108

Figure 4.12 Schematic representations of the growth of ALD Pd nanoparticles on the TiO<sub>2</sub>- and SrO-terminated STO surfaces. On the TiO<sub>2</sub>-STO surface, Pd follows the "nucleation and growth model," in which Pd atoms are able to migrate across the surface to form nuclei because the hfac species on the surface weakly bounded (i). The nucleus grows from the migration of the Pd atoms in the subsequent ALD cycles (ii). On the SrO-STO surface, Pd follows the "trapped Pd model," in which the migration of Pd is hindered by the strongly bonded hfac species (iii). In the subsequent ALD cycles, Pd forms secondary nuclei on hfac free area (iv)..... 110

Figure 4.13 Pd K-edge *in-situ* XAFS measurements of 0.8 ML Pd on the TiO<sub>2</sub>- and SrO-terminated STO surfaces. The measurements were performed at 300 °C under H<sub>2</sub>/O<sub>2</sub> redox conditions and were shown to be reversible. .... 112

Figure 5.1 TEM images of ALD-Pd deposited on STO nanopolyhedra supports. The left-hand column shows the images of (a) 0c (blank STO), (b) 1c, (c) 5c, and (d) 10c of Pd loaded on the TiO<sub>2</sub>-(001)-STO nanocuboid support. The right-hand column shows (e) 0c, (f) 1c, (g) 5c, and (h) 10c of Pd loaded on the (110)-STO nanododecahedra support. (Figure (e-h) were provided by Lawrence A. Crosby)

..... 120

Figure 5.2 Histograms of Pd nanoparticle diameters obtained from multiple representative TEM images: (a) 1c, 5c, and 10c Pd/TiO<sub>2</sub>-(001)-STO nanocuboids, and (b) 1c, 5c, and 10c Pd/(110)-STO nanododecahedra. The mean diameters ( $d$ ) and standard deviations (SD) are included. .... 121

Figure 5.3 Background subtracted SAXS data of (a) Pd/TiO<sub>2</sub>-(001)STO and (b) Pd/(110)-STO samples (offset for clarity). The interference between neighboring Pd nanoparticles leads to a broad peak in the range of  $q = 0.1 - 0.3 \text{ \AA}^{-1}$ . The position of the interference peak ( $q_p$ ) is obtained by fitting the peak with a Gaussian function on a power-law background (see Appendix B.4 for details in fitting).  $q_p$  shifts to lower  $q$  region as the number of ALD cycles increases, as indicated by the arrows. .... 123

Figure 5.4 Atomic resolution annular bright field (ABF) (a, b), TEM (d), and high angle annular dark field (HAADF) (c, e, and f) images of Pd supported on (a) (b)  $\text{TiO}_2$ -(001)-STO and (c) (d) (110)-STO surfaces. The Pd nanoparticles are single-crystalline, as the arrangement of Pd atoms can be clearly seen in the images. (e) (f) HAADF images show twinned Pd nanoparticles on  $\text{TiO}_2$ -(001)-STO and (110)-STO surfaces, respectively. The dashed line in yellow represents the twin plane. (Images provided by Lawrence A. Crosby) ..... 125

Figure 5.5 Wt% loading of Pd and (b) Pd surface coverage as a function of the number of ALD cycles calculated from both XRF and ICP measurements. The red line and the blue line represent Pd/ $\text{TiO}_2$ -(001)-STO, and Pd/(110)-STO, respectively. The coverage is defined as the surface density of Pd atoms and assumes all Pd are on the STO support surface. The numerical data of wt% and coverage are presented in Table 5.2..... 127

Figure 5.6 Pd K-edge XANES of (a) Pd/ $\text{TiO}_2$ -(001)-STO nanocuboids and (b) Pd/(110)-STO nanododecahedra. The Pd foil ( $\text{Pd}^0$ ) and PdO(II) ( $\text{Pd}^{2+}$ ) spectra are shown as references. Comparing the data to the references reveals that the chemical state of supported Pd NPs gradually shifts from  $\text{Pd}^{2+}$  to  $\text{Pd}^0$  as the

loading increases. (c) The atomic fraction of metallic Pd ( $f_{Pd0}$ ) obtained from linear combination fitting.  $f_{Pd0}$  is higher on (110)-STO than on  $\text{TiO}_2$ -(001)-STO surface at the same number of ALD cycles. .... 130

Figure 5.7 The turnover frequency (TOF) of the CO oxidation reaction at 80, 100, and 120 °C. The 1c Pd / $\text{TiO}_2$ -(001)-STO sample is more active than the others at 80 and 100 °C, as seen from the higher TOF. .... 131

Figure 5.8 DRIFTS showing CO absorption intensity as a function of  $\text{O}_2$  exposure time at room temperature for (a) 1c Pd/ $\text{TiO}_2$ -(001)-STO nanocuboids, (b) 10c Pd/ $\text{TiO}_2$ -(001)-STO nanocuboids, and (c) 1c Pd/(110)-STO nanododecahedra. (d-f) The evolution of normalized CO adsorption peak areas over time. The area denoted as L sites is the linear absorption branch ( $\sim 2000\text{-}2100\text{ cm}^{-1}$ ) and the bridge-multiple branch ( $\sim 1800\text{-}2000\text{ cm}^{-1}$ ) is denoted as B-M sites. .... 136

Figure 5.9 Evolution of the B-M to L area ratios with  $\text{O}_2$  exposure time. The B-M to L ratios stay constant for the three samples, indicating the redistribution of CO absorption sites as CO is removed. .... 137

Figure 6.1 (a) Low resolution SEM image, (b) TEM image, (c) wide angle X-ray scattering (WAXS) pattern, and (d) statistics of the  $\text{TiO}_2$ -(001)-STO nanocuboids.

The WAXS were collected at the 5ID-D beamline at the APS with an incident X-ray energy of 16 keV.....	141
Figure 6.2 TEM images showing the STO nanoparticles before and after the thermal treatment. (a) Round nanoparticles formed after NaOH addition. (b) Close-up of the yellow frame in (a), showing that there are no Kirkendall voids in the particles. (c) STO nanocuboids and Kirkendall voids formed after a 240 °C, 48 h thermal treatment. ....	142
Figure 6.3 (a) TEM image of SrO-(001)-STO nanocuboids. (Adapted from Ref. [44]) (b) Statistics of the edge length of SrO-(001)-STO nanocuboids from (a).....	144
Figure 6.4 TEM images of C3 to C7 carboxylic acids substituted for the original acetic acid-assisted synthesis. ....	147
Figure 6.5 TEM images of the three types of particles resulting from the C5 acid substituted for the original acetic acid-assisted synthesis: 1. sharp cuboids, 2. rough cuboids, and 3. rod-like structures.....	148
Figure 6.6 Results of replacing the 1.1M acetic acid in the TiO <sub>2</sub> -(001)-STO synthesis with (a) pure water and (b) 1.1M HCl in the original acetic acid-assisted synthesis. ....	149

- Figure 6.7 Ternary phase diagram of water/butanol/sodium octanoate (caprylate) at room temperature (Source: copied from page 113 of Ref. [143].) L and D are the micelle and lamellar regions, respectively. Note that the unit of the phase diagram is wt% instead of molar%. ..... 150
- Figure 6.8 Preliminary results of the octanoic acid-butanol synthesis. The compositions and the corresponding results are shown accordingly. The TEM images marked with A-F are the nanoparticles synthesized based on the chemical composition listed in Table 6.2. (Image D and F provided by Lawrence A. Crosby) ..... 154
- Figure 6.9 (a) Low-magnification SEM and (b) HAADF images demonstrating the dodecahedral shape of the nanoparticles. The three-dimensional characters are evident in (a), and are shown in (b) via intensity changes at the corners. The geometry of a dodecahedron is illustrated in (c). (Source: (a) and (b) were provided by Lawrence A. Crosby and were published in Ref. [45].) ..... 157
- Figure 6.10 XRD pattern for the STO nanodecahedra..... 159
- Figure 6.11 XRD peaks of (a) the (110) peak of the STO dodecahedra and (b) the (111) peak of the 325 mesh Si powder. By applying the modified Scherrer equation

(6.1), the mean crystallite size in the [hkl] direction can be determined from the broadening of the (hkl) diffraction peak. .... 159

Figure 6.12 (a) Experimental images down the [001] zone and the simulated result (red box) for a  $(3 \times 1)$  reconstruction. The inset images below shows the simulations for the  $(3 \times 1)$  and  $(4 \times 1)$  reconstructions with the atomic structures superimposed. (b) Experimental images down the [110] zone and the simulated result (red box) for a  $(4 \times 1)$  reconstruction. The inset images below shows the simulations for the  $(3 \times 1)$  and  $(4 \times 1)$  reconstructions with the atomic structures superimposed. The  $(3 \times 1)$  gave the best fit to experiment for this area, although in other regions it was the  $(4 \times 1)$ . (Source: Ref. [45], HREM images and the analysis provided by Lawrence A. Crosby) ..... 161

Figure 7.1 Synthesis and proposed structure of the  $(-\text{AlO}_x)\text{Pd}(\text{acac})$  complex. (Image provided by Aidan R. Mouat) ..... 164

Figure 7.2 Histograms of Pd nanoparticle diameters extracted from TEM images: size distributions when the  $(-\text{AlO}_x)\text{Pd}(\text{acac})$  complex reduced in 1-octene at room temperature for (a) 24 h (b) 72 h and (c) 120 h. (TEM and image analysis provided by Aidan R. Mouat and Cassandra L. Whitford.) ..... 164

- Figure 7.3 (a) XANES and (b) EXAFS data at the Pd K-edge of the  $(-\text{AlO}_x)\text{Pd}(\text{acac})$  complex under ethylene reduction from 0 to 9 h. .... 167
- Figure 7.4 The evolution of  $f_{\text{Pd}0}$  and  $f_{\text{Pd}2+}$  with the ethylene reduction time. The phase fraction of Pd was obtained from the linear combination fitting of the  $\text{Pd}(\text{acac})_2$  and Pd foil reference XANES spectra. .... 167

## LIST OF TABLES

Table 2.1 Comparison between single crystal and powder catalyst supports. ....	44
Table 2.2 A summary of different growth conditions of Pd deposited onto STO(001) surfaces with various reconstructions. (Adapted from Ref. [38]).....	49
Table 2.3 Surface reconstructions of STO nanopolyhedra (Source: adapted from [45,70]).....	54
Table 4.1 The average aspect ratios of the 5c and 10c Pd nanoparticles. ....	93
Table 4.2 The atomic percentage ratio of Pd and Sr can be directly measured from both ICP-AES (inductively coupled plasma atomic emission spectroscopy) and XRF (X-ray fluorescence). Pd loading and the effective Pd coverage ( $\theta_{\text{Pd}}$ ) can then be calculated by assuming that the atomic ratio of Sr:Ti:O in the SrTiO <sub>3</sub> nanocuboids is exactly 1:1:3.....	96
Table 4.3 Atomic phase fraction of Pd <sup>0</sup> phase determined from both XANES and EXAFS analysis described in Figure 4.8. ....	101
Table 4.4 Fitting parameters of Pd K-edge EXAFS of as-deposited Pd/SrTiO <sub>3</sub> nanocuboids, including the first nearest neighbor coordination numbers ( $N$ ), bond	

distances ( $R$ ), EXAFS Debye-Waller factors ( $\sigma$ ), and energy shifts ( $\Delta E$ ) for Pd–Pd and Pd–O scattering paths.....	102
Table 4.5 Fitting parameters of Pd K-edge EXAFS of Pd/SrTiO <sub>3</sub> nanocuboids reduced in H <sub>2</sub> at 300 °C for 30 min. The fitting parameters include the first nearest neighbor coordination numbers ( $N$ ), bond distances ( $R$ ), EXAFS Debye-Waller factors ( $\sigma$ ), and energy shifts ( $\Delta E$ ). Notice that the error bar is large in the Pd–O path because the Pd–O contribution presumably only comes from the interface bonding between Pd and the oxygen in the SrTiO <sub>3</sub> lattice. ....	106
Table 5.1 Fitted interparticle spacing ( $D$ ) from the SAXS results in Figure 5.3. ....	123
Table 5.2 Atomic ratio of Pd to Sr, Pd loading (wt%), and Pd coverage.....	128
Table 5.3 The CO oxidation turnover frequency (TOF) at 80 - 120 °C for the Pd/STO catalysts. TOF was calculated from ICP obtained wt% and TEM estimated metal dispersion (see Appendix B.6 for details).....	132
Table 6.1 List of the carboxylic acids used in the short carboxylic acid synthesis.....	146
Table 6.2 The table shows the volumes of Sr(OAc) <sub>2</sub> , Ti(OBu) <sub>4</sub> , octanoic acid, butanol, and water used in the octanoic-butanol synthesis. Samples A-F were prepared by varying the chemical composition as described.....	152

## Chapter 1: Introduction

### 1.1 Motivation

Oxide-supported metallic nanoparticle catalysts have been extensively studied to improve their activity, selectivity, and durability. One major factor that influences catalytic activity is the interaction between the nanoparticle and its support material. Metal-support interaction is described by the multi length-scale morphological and electronic changes, including the encapsulation of metal nanoparticles by the migration of support atoms [1,2], partial embedment of metal nanoparticles [3,4], redistribution of interfacial charges [5,6], participation of surface lattice oxygen in reactions [7–9], and stabilization of non-interacting metal nanoparticles [10,11]. In order to address the support effects, the complexity of poorly-defined metal/oxide interfaces in real-world powder catalysts has to be reduced by using well-defined single crystal oxide substrate surfaces [12–23]. However, the relatively low surface area of a single crystal substrate limits the measurable sensitivity to chemical reactions.

To bridge the materials gap [18,19,21] between conventional single crystal surface science studies and catalytic reaction studies on powder samples, this dissertation introduces the designed ensemble of mono-dispersed, single-crystal “nanopolyhedra catalyst supports.” The nanopolyhedra catalyst supports are oxides of well-defined, orientation-specific facets. Each facet resembles a single crystal surface, while the nano-size of the nanopolyhedra provides enough surface area for reactivity measurement by using lab-scale reactors [10,24–26].

The Pd/SrTiO<sub>3</sub> (STO) nanopolyhedra system described in this dissertation is inspired by earlier work on Pt [27–35] and Pd [36–38] nanoparticles grown on STO single crystal surfaces. The shapes and orientations of the Pt or Pd NPs predicted by thermodynamics using the

Winterbottom construction [39] can be affected by the STO chemical termination [28,40], crystalline orientation [29,30], and surface reconstruction [37,38]. However, studying the influence of the shapes of Pd (Pt) nanoparticles on the catalytic performance is not easy due to the low surface areas of single crystal supports, which result in a lower measurement sensitivity. STO single crystal nanopolyhedras with controllable  $\text{TiO}_2$ -(001), SrO-(001), or (110) surface terminations [41–45] was synthesized due to recent advances in hydrothermal synthesis. This enables the influence of the nanoparticle morphology on its catalytic activity to be studied directly, as demonstrated in previous studies of Pt on  $\text{TiO}_2$ -(001)-STO nanocuboids [10,24,26].

This dissertation presents the relationship between morphology and catalytic activity of ALD-grown Pd nanoparticles on three types of STO nanopolyhedra:  $\text{TiO}_2$ -(001)-terminated nanocuboids, SrO-(001)-terminated nanocuboids, and (110)-terminated nanododecahedra. The size and coverage of the Pd nanoparticles were controlled by the number of ALD cycles, as demonstrated in previous studies on ALD-Pt [10,24,26,31,33,46]. Multiple characterization methods were employed to analyze the physical and chemical properties of the Pd nanoparticles, including Transmission electron microscopy (TEM), small-angle X-ray scattering (SAXS), X-ray fluorescence (XRF), X-ray photoelectron spectroscopy (XPS), and X-ray absorption spectroscopy (XAS).

To compare the catalytic performance of Pd on different types of STO nanopolyhedra, CO oxidation is employed as a probe reaction. The CO oxidation catalytic activity of the free-standing Pd (Pt) nanoparticles depends upon the exposed crystal facets, as studies have shown that (111) facets of Pd (Pt) are significantly more active than (001) facets [47,48]. By combining the Pd/STO nanopolyhedra catalytic system with the CO oxidation reaction, this

dissertation aims to establish the relationship between the Pd/STO interface morphology and its resulting influence on catalytic activity.

## 1.2 Outline

This dissertation is organized into eight chapters. **Chapter 2** serves as a background review of the Pd/SrTiO<sub>3</sub> catalytic system. The synthetic and analytical characterization techniques employed in this dissertation is introduced in **Chapter 3**. **Chapter 4** compares Pd supported on TiO<sub>2</sub>-(001)-STO and SrO-(001)-STO nanocuboids. Additionally, the morphology, structure, and oxidation states of Pd as a function of the number of ALD cycles will be established. **Chapter 5** extends the STO support to (110)-STO nanododecahedra supports. The correlation between the Pd morphology and CO oxidation activity will be discussed in detail. **Chapter 6** presents the synthesis works of various types of STO nanopolyhedra. **Chapter 7** presents the characterization of small and mono-dispersed Pd nanoparticles synthesized from a newly developed grafting reaction of Pd(acac)<sub>2</sub> on  $\gamma$ -Al<sub>2</sub>O<sub>3</sub>. The growth of Pd is probed by using in-situ X-ray absorption spectroscopy. **Chapter 8** is a summary of the main findings in this dissertation as well as future directions.

## Chapter 2: Background

### 2.1 Metal-Oxide Support Interface in Heterogeneous Catalysis

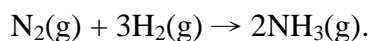
#### 2.1.1 Introduction of Catalysis

Catalysts are substances added to a chemical reaction that increases the rate of the reaction by providing another reaction pathway with lower activation energy, but without itself undergoing permanent chemical change (Figure 2.1). The earliest concept of catalysis can be traced back to 1794 in the book "*An Essay on Combustion*" written by Scottish chemist Elizabeth Fulhame [49,50]. Fulhame reported that the water participating in oxidation-reduction reactions was regenerated at the end of the reactions, which "*formed a new quantity of water equal to that decomposed* [51]."

However, a clearer definition of a modern catalyst was not established until 40 years later. In 1835, Swedish chemist Jöns Jacob Berzelius stated the following [52,53]: "*It is shown that several simple and compound bodies, soluble and insoluble, have the property of exercising on other bodies and action very different from chemical affinity. The body effecting the changes does not take part in the reaction and remains unaltered through the reaction. This unknown body acts by means of an internal force, whose nature is unknown to us... I will therefore call it the "Catalytic Force" and I will call "Catalysis" the decomposition of bodies by this force.*" With this statement, Berzelius started a new era of systematic catalysis research, including the discovery of new catalytic processes, and the enhanced perception of the nature of chemical reactions [52].

The study of catalysis was then continued over the 19<sup>th</sup> century along with the development of several important concepts in chemical reactions that served as the foundation of modern

chemistry. The development of industrial scale catalytic reactions started at the beginning of the 20<sup>th</sup> century. German chemist Fritz Haber and Carl Bosch developed a new method for converting atmospheric nitrogen (N<sub>2</sub>) into ammonia (NH<sub>3</sub>) through the reaction



Ammonia is a widely used compound in nearly every aspect of human life, including the production of antimicrobial agents, nitrogenous compounds, and artificial fertilizers. Before the new method was introduced, it was extremely difficult to convert N<sub>2</sub> molecules into NH<sub>3</sub>. Extreme conditions of temperature and pressure were required to destabilize the N-N triple bond, as well as to increase the probability of bringing gaseous N<sub>2</sub> and H<sub>2</sub> molecules together. To reduce the energy/pressure input and increase the rate of the reaction, Haber and Bosch introduced osmium (Os) metal as a catalyst to fix and dissociate N<sub>2</sub> gas on the surface of Os. The addition of Os dramatically increased the rate of the reaction because the N<sub>2</sub> dissociation is the rate-determining step of the N<sub>2</sub> fixation process [54,55]. Later, Os was substituted by less expensive Fe<sub>3</sub>O<sub>4</sub> to meet the industrial processing requirements. This substitution further yielded an inexpensive and efficient ammonia production method on an industrial scale. The Haber-Bosch ammonia synthesis tremendously changed the world with its impacts on agriculture, industry and economics. The synthesis is still in service today [56].

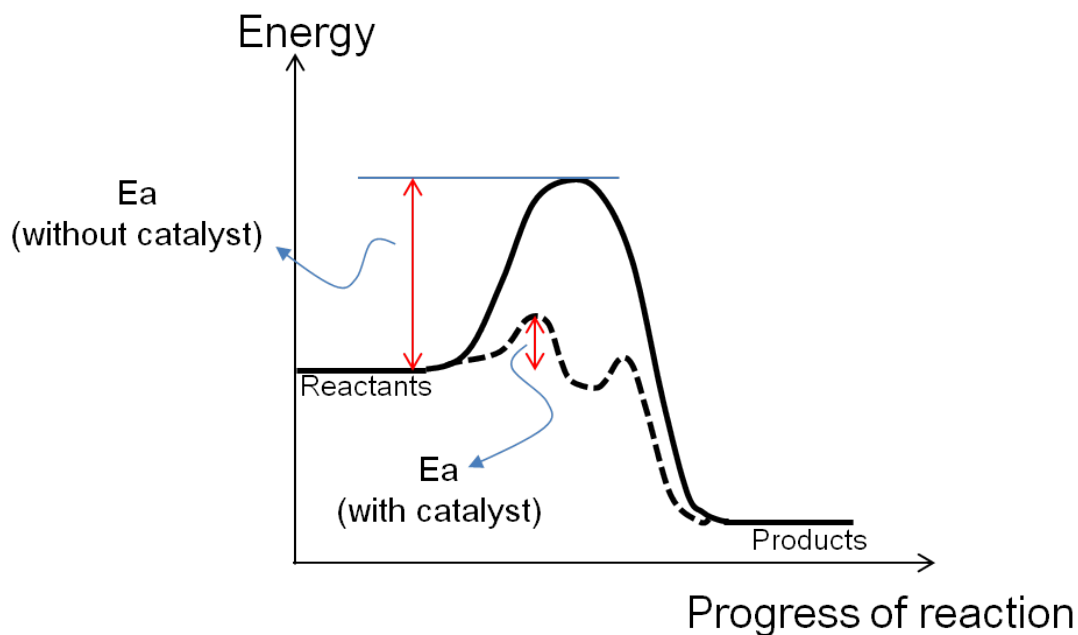


Figure 2.1 Schematic diagram illustrating the progress of a chemical reaction with and without the presence of a catalyst. (Source: adapted from Ref. [57])

Nowadays, there are various forms of catalysts playing critical roles in every aspect of the modern chemical industry [58]. Though the forms of catalysts vary, they can be divided into two major categories: homogeneous catalysts and heterogeneous catalysts. The former involves catalytic reactions in which the catalyst is in the same phase with the reactants, while the latter possesses a different phase compared to the reactants. The Haber-Bosch method is a typical example of a heterogeneous catalysis, which involves gaseous reactants ( $\text{N}_2$  and  $\text{H}_2$ ) and a solid state catalyst ( $\text{Fe}_2\text{O}_3$ ). A great majority of practical heterogeneous catalysts are solid catalysts interacting with gaseous and/or liquid reactants.

A heterogeneous catalytic reaction involves the adsorption of reactant molecules onto the catalyst surface, surface reaction of the adsorbed species, and desorption of the products [59]. The adsorbed molecule-surface complex creates a transition state that allows the chemical reaction to take a reaction path with a lower energy barrier, as shown in Figure 2.1. Scientists and engineers have invested a significant amount of effort towards understanding the catalytic reaction mechanisms, the identity of the adsorption sites, and the intermediate species at the transition state. Understanding the nature of catalytic reactions helps us gain fundamental knowledge about catalysis and provides insights into the development of next-generation catalysts with improved performance. Over the past 100 years, many Nobel Prizes have been awarded for catalysis-related achievements in both scientific understanding and practical development. Nobel Laureates in this field include: Wilhelm Ostwald (1909), Fritz Haber (1918), Carl Bosch (1931), Irving Langmuir (1932), William S. Knowles/Ryoji Noyori (2001), Gerhard Ertl (2007), Richard F. Heck/Ei-ichi Negishi/Akira Suzuki (2010), and many others.

One of the challenges in catalyst research is reducing the cost and increasing the activity of the catalysts, especially for expensive platinum group metal (PGM)-based catalysts. The PGMs, including Ru, Rh, Pd, Pt, Ir and Os, are transition metals with similar physical and chemical properties and high catalytic activity. Pt, Pd, and Rh are the most commonly used catalysts in automobile catalytic converters to convert CO and NO<sub>x</sub> to relatively harmless CO<sub>2</sub>, N<sub>2</sub>, and H<sub>2</sub>O. Up to 90% of toxic substances from automobile exhausts can be removed by catalytic converters [60]. On average, for a small car, the recoverable amount of PGM is 1-2 grams, and that for a large truck is 12-15 grams in the US [61]. According to another statistic from 2010, the total value of Pt, Pd and Rh reclaimed from used catalytic converters was \$3 billion.

Although this technology is an environmental necessity, a major challenge of the PGM-based catalyst is the high cost and limited supply. As shown in Figure 2.2, the average prices of Pt and Pd in the recent 10 years is approximately \$1500/oz and \$600/oz, respectively. Finding alternative materials to replace PGMs is a possible option to reduce the cost of catalytic converters. However, the high catalytic activity that can be achieved with PGMs will be sacrificed. An alternative approach that could be developed is to redesign the geometry of the catalysts to achieve the same activity with a smaller amount of PGMs. To reach this goal, a deeper understanding of the reaction mechanism and the identity of active sites in PGM-based heterogeneous catalysts becomes crucial.

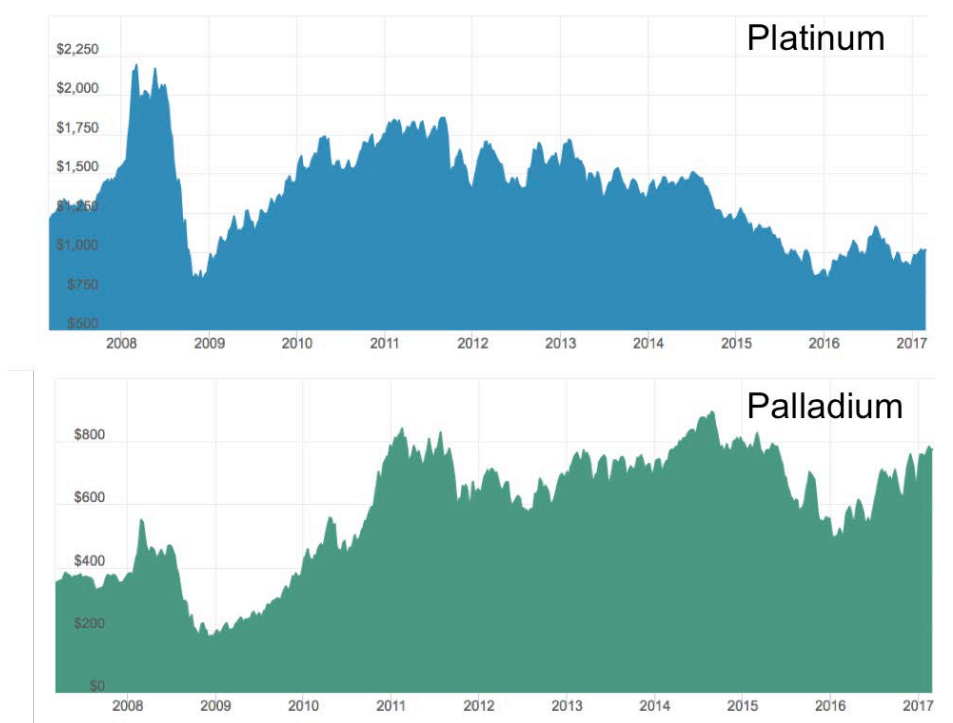


Figure 2.2 The Price history of Pt and Pd from March 2008 to March 2017. (Source: <http://www.apmex.com/spotprices/> [62]).

### 2.1.2 Importance of the Metal-Oxide Support Interface in Heterogeneous Catalysts

In heterogeneous catalysts, the active phase (metal phase) is dispersed upon a “catalyst support,” which is usually an oxide with high surface area. This metal/oxide support enhances the dispersion of the catalytically active phase and thermal stability [17,63]. Commonly used catalyst supports include alumina, silica, titania, zirconia, and zeolites [64]. In the past, supports were assumed to be inert. However, this assumption is an oversimplification because of non-negligible interactions between the metal catalyst and support. In the 1980s, Tauster

observed that the chemisorption of H<sub>2</sub> or CO on group VIII metals was dramatically suppressed when the metals were supported on titanium oxide supports [1]. This phenomenon was contradictory to the common understanding that group VIII metals absorb H<sub>2</sub> or CO strongly. The reason is that titanium oxide support migrates and masks a significant portion of the metal surface. As a consequence, the surface of the metal is covered and the gas adsorption is inhibited. This effect is called the “strong-metal-support-interaction (SMSI) [1,2].” SMSI is not the only type of the metal-support-interactions. The interactions also involve multi length-scale morphological and electronic changes of metal nanoparticle and interface, including the partial embedment of metal nanoparticles [3,4], redistribution of interfacial charge [5,6], participation of the surface lattice oxygen in reactions [7–9], and stabilization of isolated non-interacting metal NPs [10,11].

Metal-support interactions also influence the rate of catalytic reactions such as CO oxidation or water-gas-shift (WGS) reactions [5,7,65–67]. As summarized by Cuenya et al. [68], the support effects influence the performance of catalytic reactions in the following ways:

- Changing the structure and shape of the supported nanoparticles.
- Introducing charge transfer across the interface.
- Providing additional reactions sites.
- Stabilizing the supported nanoparticles against coarsening.
- Encapsulating the surface of the nanoparticles.

### 2.1.3 Model Catalysts and Materials Gap

The poorly-defined surfaces on real-world catalyst supports have made the investigation of atomic and electronic structure at the metal/support interface difficult, thereby inhibiting the development of a fundamental understanding of the interface. To overcome the challenge presented by the real-world catalysts, well-defined single crystal surfaces with reduced interface complexity were introduced as “model catalyst supports [12–23].” Model catalysts are metals deposited on well-ordered single crystal substrate surfaces that can be prepared with various levels of complexity [23] to simulate real-world catalysts on a lab-scale, as shown in Figure 2.3.

However, the relatively low specific surface area of a single crystal surface limits the measurable sensitivity to chemical reactions. An ultra high vacuum (UHV) environment is therefore required to utilize surface-sensitive spectroscopies and to guarantee a clean single crystal surface. In contrast, industrial catalysts are typically high surface area powders, which are operated at pressures greater than 1 atm [22]. Table 2.1 summarizes the differences between single crystal and powder catalyst supports. The huge difference in the material structures and operation pressures between the two types of supports thereby leads to the so-called “materials gap” and “pressure gap,” [18,19,21] which prevents experimental results obtained from single crystal supports and powder supports translating to each other.

Several approaches are used in order to bridge the materials gap and pressure gap, including increasing the sensitivity of the analytical tools [19] and developing surface sensitive techniques with high pressure capabilities [18,21]. Another strategy established by our research team at Northwestern University is to employ oxide “nanopolyhedra supports” with well-defined single

crystal facets. This “nanopolyhedra approach” and the materials system studied in this dissertation will be elaborated in detail in Section 2.2.

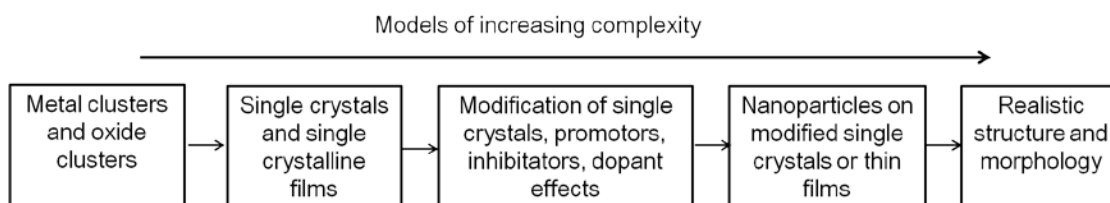


Figure 2.3 Evolution of model catalyst systems with increasing complexity towards the real-world catalysts (Source: adapted from Ref. [23]).

Table 2.1 Comparison between single crystal and powder catalyst supports.

	<b>Single crystal support</b>	<b>Powder support</b>
<b>Support surface</b>	Well-defined	Poorly-defined
<b>Surface area</b>	Low	High
<b>Complexity</b>	Simple	Complex
<b>Operation pressure</b>	Ultra high vacuum ( $10^{-7}$ - $10^{-9}$ Torr)	> 760 Torr
<b>Applicability</b>	Fundamental surface science studies on a lab scale	Practical application on an industrial scale

## 2.2 Materials

### 2.2.1 Introduction

Inspired by the earlier work on Pt [27–35] and Pd [36–38] nanoparticles grown on SrTiO<sub>3</sub> (STO) single crystal substrates, this dissertation focuses on studying the Pd/SrTiO<sub>3</sub> oxide

nanopolyhedra system. The research team at Northwestern University studied Pt [10,24,26,69] and Pd [40] nanoparticles grown on STO single crystal nanopolyhedra with predominantly (001) surfaces and controllable  $\text{TiO}_2$  or SrO surface terminations, which were produced by hydrothermal synthesis. Recently, the hydrothermal synthesis was further extended to yield (110)-terminated nanododecahedra [45]. This advance in synthesis allows direct comparisons of morphology and activity between metal nanoparticles grown on atomically-flat and distinct STO nanopolyhedra surfaces [45,70]. This approach opens up opportunities to investigate the metal/oxide interface correlation at the atomic-scale, while the high surface-to-volume ratios of the nanopolyhedra supports enable practical catalytic reactions [10,25], similar to the case of powder catalysts.

This chapter is organized in the following way: In Section 2.2.2, a general introduction of STO is presented. Section 2.2.3 reviews earlier works of Pd and Pt supported on STO single crystal surfaces that motivates the present research. In Section 2.2.4, various types of STO nanopolyhedra supports are introduced. Section 2.2.5 introduces atomic layer deposition (ALD) as a novel method to grow catalytic Pd (Pt) nanoparticles. Section 2.2.6 reviews previous works of ALD-Pd (Pt) on STO single crystal and nanopolyhedra supports.

### **2.2.2 Overview of $\text{SrTiO}_3$**

$\text{SrTiO}_3$  (STO) is a representative of the  $\text{ABO}_3$  perovskite family. A unit cell of the  $\text{ABO}_3$  structure consists of an alkaline or alkaline earth metal cation in the A site, and a transition metal cation in the B site. Figure 2.4 shows a unit cell of STO, which is simple cubic structure with a lattice constant of 3.905 Å. STO consists of alternating layers of  $\text{TiO}_2$  and SrO.

STO is one of the most studied  $ABO_3$  materials because of its outstanding dielectric properties [71], high-temperature superconductivity [37], and applicability as a substrate for thin film growth [72,73]. In the fields of catalysis, STO was investigated as a photocatalyst in water splitting [74,75] and CO reduction [76,77] reactions. Recently, much interest has been focused on Pd and Pt nanocrystals supported on STO because the surface faceting of Pd (Pt) is shown to be selectable through the modification of STO surface structures [28–30,37,38,40].

The surface structures of STO can be very different from that of the bulk due to surface reconstruction. On the surface, the atoms rearrange themselves from their original positions in the bulk structure and form new periodic structures to minimize the surface free energy. The surface reconstruction of STO is strongly dependent on annealing conditions, such as temperature and time. Much work has been devoted to establishing the atomic models of STO surface reconstructions [78–86], which influence the growth of crystalline materials on the surfaces. Section 2.2.3 will introduce several examples of the shapes and exposed crystalline facets of Pd (Pt) nanocrystals being influenced by STO surface reconstructions.

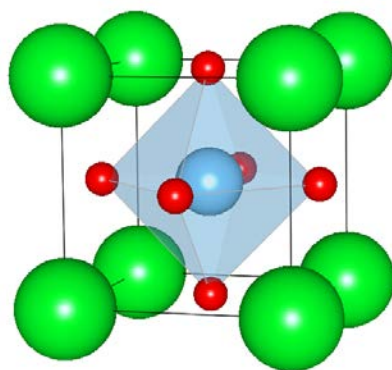


Figure 2.4 A unit cell of cubic  $SrTiO_3$ . The green, red, and blue balls represent Sr, O, and Ti atoms, respectively.

### 2.2.3 Faceted Shapes of Pd (Pt) Nanocrystals on STO Single Crystal Surfaces

Pt [27–35] and Pd [36–38] nanocrystals supported on STO single crystal surfaces has been the subject of much research throughout the past decade. As two key members of the PGM family, Pd and Pt are widely studied for their high catalytic activity. In addition, very close lattice matching is exhibited between STO and both Pd and Pt. Pd and Pt demonstrate face-centered cubic (FCC) structures with lattice constants of 3.890 Å and 3.920 Å, respectively. Their lattice constants only differ from that of STO (3.905 Å) by 0.4%. Given such small lattice mismatches, strain-relaxed cube-on-cube epitaxy is expected between Pd (Pt) and STO.

The shape of Pd nanoparticles can be designed by careful control of the STO surface reconstruction. As shown in Figure 2.5, the crystallographic interface of Pd is able to be selected by utilizing different annealing conditions to modify the STO(001) surface reconstructions, resulting in distinctive Pd nanocrystal shapes (huts, hexagons, and truncated pyramids). The growth conditions of Pd/STO as well as the corresponding interfacial crystalline orientations and shapes are summarized in Table 2.2.

In addition to the surface reconstruction of STO, the thermodynamically predicted Winterbottom shapes [39] and the orientations of the Pd (Pt) can also be affected by the STO chemical termination [28] and crystalline orientation [29,30]. Polli et al. demonstrated that Pt orientations were strongly dependent on the chemical termination of STO(001) surface, i.e., TiO<sub>2</sub>- and SrO-terminations [28]. Cube-on-cube epitaxy of Pt was predominant on TiO<sub>2</sub>-terminated STO(001) surface, whereas a mixture of Pt(100) and (111) was shown on SrO-terminated surface. The Pt shape is also influenced by the crystalline orientation of the STO support, as shown by Komanicky et al. [30]. When Pt is deposited on STO(001), (110) and (111)

surfaces, the growth orientation of Pt follows that of the STO support, leading to distinctive shapes, as shown in Figure 2.6.

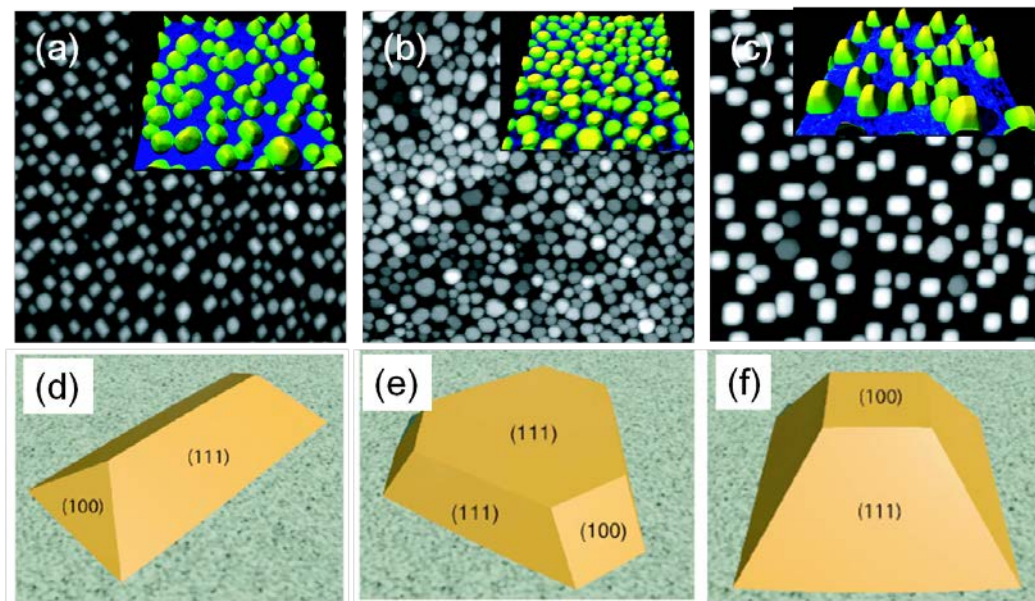


Figure 2.5 From Silly and Castell [37],  $140 \times 140 \text{ nm}^2$  scanning tunneling microscopy (STM) images with insets showing 3D renderings of the NP shapes (a-c) and the models (d-f) of the Pd nanocrystals supported on the (001)-STO single crystal surface. (a, d) Hut-shaped Pd grown on a  $(2 \times 1)$  surface at room temperature followed by  $650 \text{ }^\circ\text{C}$  annealing. (b, e) Hexagonal-shaped Pd grown on a  $c(4 \times 2)$  substrate at room temperature followed by  $650 \text{ }^\circ\text{C}$  annealing. (c, f) Pyramid-shaped Pd grown on a  $c(4 \times 2)$  substrate at  $460 \text{ }^\circ\text{C}$  followed by  $650 \text{ }^\circ\text{C}$  annealing. (Source: (a-c) adapted from Ref. [37], and (d-f) adapted from Ref. [38].)

Table 2.2 A summary of different growth conditions of Pd deposited onto STO(001) surfaces with various reconstructions. (Adapted from Ref. [38])

	<b>STO surface reconstruction</b>	<b>Pd growth conditions</b>	<b>Interfacial crystallography</b>
<b>Hut</b>	$(2 \times 1)$	deposited at room temperature, followed by 650 °C annealing	$(011)_{\text{Pd}} \parallel (001)_{\text{SrTiO}_3}$ $[110]_{\text{Pd}} \parallel [100]_{\text{SrTiO}_3}$
<b>Hexagonal</b>	$c(4 \times 2)$	deposited at room temperature, followed by 650 °C annealing	$(111)_{\text{Pd}} \parallel (001)_{\text{SrTiO}_3}$ $[110]_{\text{Pd}} \parallel [110]_{\text{SrTiO}_3}$
<b>Pyramid</b>	$c(4 \times 2)$	deposited at 460 °C, followed by 650 °C annealing.	$(001)_{\text{Pd}} \parallel (001)_{\text{SrTiO}_3}$ $[100]_{\text{Pd}} \parallel [100]_{\text{SrTiO}_3}$

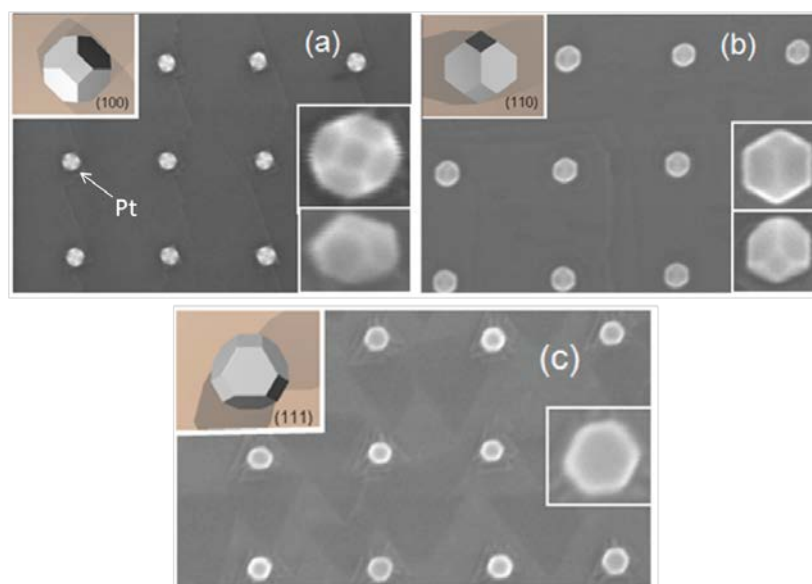


Figure 2.6 Scanning electron microscopy (SEM) images of Pt nanocrystal arrays supported on (a) (100), (b) (110), and (c) (111) single crystal surfaces of STO. Insets on the right are close-up top and side views, and insets on the left are the 3D models of the Pt nanocrystal. The Pt nanocrystals are located on 200 nm square lattices. (Source: adapted from Ref. [30])

Because the interface structure influences the growth of Pd (Pt) nanocrystals tremendously, constructing an atomic-level model of the interface is a necessary step to understand the metal deposition process. To achieve the goal, element-specific, atomic level imaging techniques are required to analyze the interface, such as X-ray standing wave (XSW). By using XSW, Feng et al. showed that the interfacial bonding between Pt and (2 × 1) STO(001) surface is coverage dependent [34]. At low (0.17 ML) coverage, Pt prefers to bond on top of the O atoms, while at high coverage (0.60 ML), Pt favors bonding to the Ti atoms. The experimental results obtained by XSW were further verified by density functional theory (DFT) calculations [35,87].

#### **2.2.4 STO Nanopolyhedra Supports**

While Pd and Pt nanocrystals display various shapes on STO single crystal surfaces, little is known about the correlation between the shapes and catalytic performance. However, it is difficult to measure catalytic activity on single crystal surfaces due to its limited measurable sensitivity, as discussed in Section 2.1.3.

The research team at Northwestern University is devoted to developing STO “nanopolyhedra supports” to bridge the materials gap between single crystal and power catalyst supports since 2008 [24]. The nanopolyhedra supports are oxide single crystals synthesized with well-defined and controllable facets, as shown in Figure 2.7. This approach provides an opportunity to investigate the metal/oxide interface correlation at the atomic-scale, while the high surface-to-volume ratios of the nanopolyhedra enable practical catalytic reactions [10,25]. A successful nanopolyhedra catalyst support exhibits the following characteristics:

- Distinguishable low-index crystallographic facets, ideally belong to the same family of planes
- Well-defined surface structure on the facets
- High surface-to-volume-ratio
- Good control of the shape and size distribution, preferably mono-dispersed
- Small particle size, preferably  $< 1,000$  nm to enable high resolution electron microscopy imaging at the interface
- Good reproducibility
- Ability to be synthesized in large scale ( $\sim$  several grams) for catalytic reactions

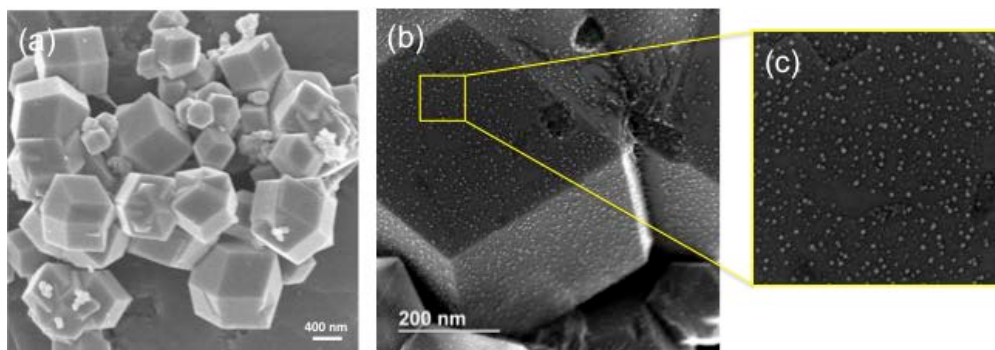


Figure 2.7 An example of the metal/oxide nanopolyhedra catalytic system. (a) The  $\text{SrTiO}_3$  nanopolyhedra under scanning electron microscopy (Hitachi SU8030). (b) Pd nanoparticles supported on  $\text{SrTiO}_3$  nanopolyhedra under transmission electron microscopy (Hitachi 2300A S/TEM). (c) Close-up of a facet in (b), showing that the facet resembles the surface of a single crystal support catalyst. (TEM images in (b) and (c) were provided by L.A. Crosby. The electron microscopy works made use of the EPIC facility in NUANCE Center of Northwestern University.)

Currently, four types of STO nanopolyhedra supports with distinctive surface chemical terminations and crystalline orientations have been created through hydrothermal synthesis, as displayed in Figure 2.8:

- $\text{TiO}_2$ -terminated (001) STO nanocuboids [41,42]
- SrO-terminated (001) STO nanocuboids [43,44]
- (110)-terminated STO nanododecahedra [45]
- Mix-terminated STO nanocuboids [70]

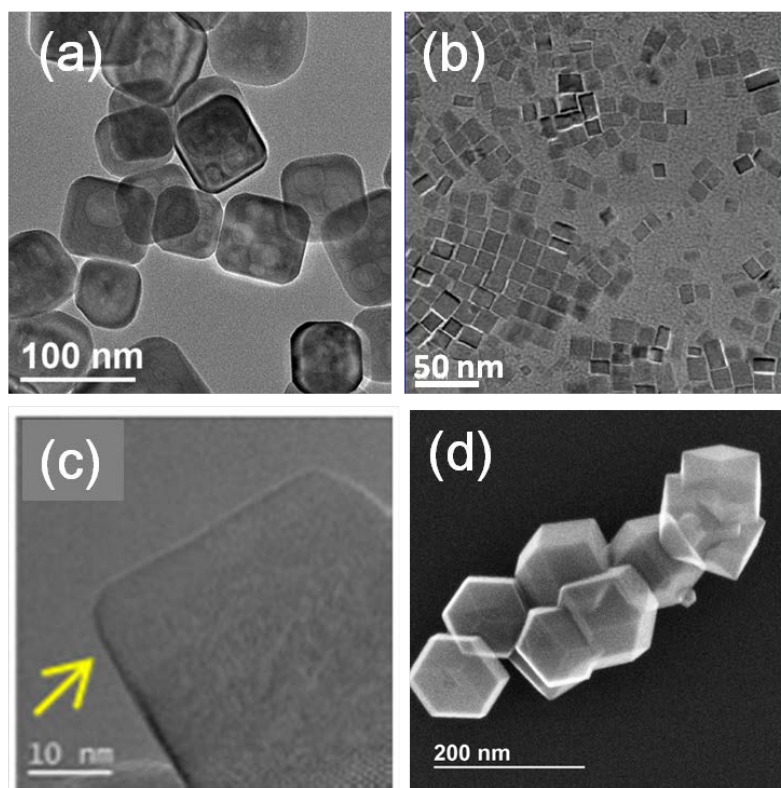


Figure 2.8 TEM images of various types of STO nanopolyhedra. (a) TiO<sub>2</sub>-terminated (001)-STO nanocuboids, (b) SrO-terminated (001)-STO nanocuboids (Source: Ref. [44]), (c) Mix-terminated (001)-STO nanocuboids (Source: Ref. [70]), and (d) (110)-STO nanododecahedra (Source: Ref. [45]). More details of the synthesis of nanopolyhedra are presented in Chapter 6.

Structure at surfaces the of the four types of STO nanopolyhedra were examined by high resolution electron microscopy (HREM) [45,70]. The results showed that the distinctive surface reconstructions also exist on the surface of the STO nanopolyhedra.

Table 2.3 Surface reconstructions of STO nanopolyhedra (Source: adapted from [45,70])

<b>Types of STO nanopolyhedra</b>	<b>Surface reconstructions</b>
TiO <sub>2</sub> -(001) STO nanocuboids	TiO <sub>2</sub> glass on top of (1×1) TiO <sub>2</sub> subsurface
SrO-(001) STO nanocuboids	(1×1) SrO
Mix-terminated STO nanocuboids	(3×3) and SrO
(110)-STO nanododecahedra	(3×1) and (4×1)

### 2.2.5 Atomic Layer Deposition (ALD) Growth of Metals

To grow Pd (Pt) nanoparticles on STO nanopolyhedra, conventional e-beam evaporation used in depositing metals on single crystal surfaces is not applicable because of the incompatibility of UHV conditions with powder catalyst supports. Although solution-based synthesis is applicable to powder-based catalyst supports, it usually has poor control over the size distribution and loading of the metal nanoparticles. Atomic layer deposition (ALD) is an ideal technique to deposit metal nanoparticles on various oxide powders or single crystals with control over its structure at the atomic level [88]. Pt, Pd, and Rh are common catalytically active noble metals that can be synthesized by ALD on oxide supports such as TiO<sub>2</sub>, Al<sub>2</sub>O<sub>3</sub>, ZrO<sub>2</sub>, CeO<sub>2</sub>, and SrTiO<sub>3</sub> [88–91].

A typical ALD process involves alternating self-limiting surface chemical reactions in a sequential manner on the surface. The ALD process consists of the following steps, as shown in Figure 2.9:

1. Expose the surface to the first precursor, which chemisorbs onto the adsorption sites on the surface (hydroxyl groups (-OH)).
2. Purge the reaction chamber with inert gas (nitrogen) to clean up the unreacted precursor and by-products.
3. Expose the surface to the second precursor, which reacts with the first precursor on the surface and forms the product.
4. Purge the reaction chamber again with the inert gas to clean up the unreacted precursor and by-products.

The repetition of steps 1 to 4 is called an "ALD cycle." The desired product can be precisely constructed on the surface by this cycle-by-cycle, bottom up approach [88].

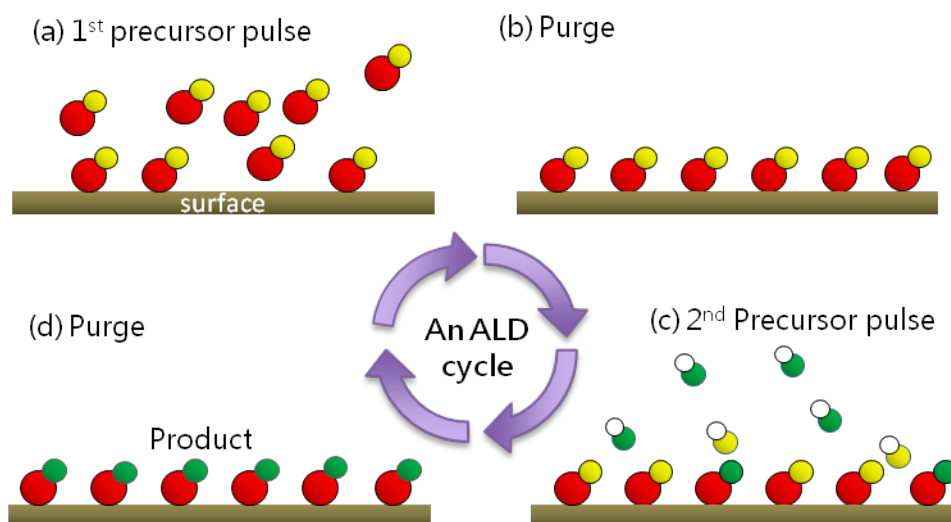


Figure 2.9 A schematic model of a general ALD binary reaction sequence. Two precursors are sequentially introduced to a substrate surface with inert gas purging in between. (a) Pulsing of the first precursor and formation of active sites reaction byproducts, (b) Purging of byproducts and unreacted precursors, (c) Pulsing of the second precursor, and (d) Purging of by-products and the second precursor, which are unreacted. The process of (a-d) is referred to as an "ALD cycle."

### 2.2.6 ALD-Pt on STO Single Crystal Surfaces and Nanopolyhedra Supports

Recent work exploring ALD-Pt on STO supports has demonstrated control over both the morphology and loading of Pt by tuning the number of ALD cycles. Christensen et al. observed that Pt formed discrete, uniform-sized nanoparticles with an average diameter ranging from 2 - 8

nm and an interparticle spacing ranging from 2-9 nm depending on the number of ALD cycles [31]. The Pt nanoparticles grow and coalesce with increasing number of ALD cycles, ultimately resulting in a continuous film after 40 cycles, as shown in Figure 2.10(a). A later study by Feng et al. [33] showed that there is cube-on-cube epitaxy between the Pt nanocrystalline islands and the STO(001) support after annealing in UHV at 800 °C for 10 min.

Following the case of Pt/STO(001), Christensen et al. were the first to demonstrate that ALD-Pt also disperses uniformly on all the exposed surfaces of TiO<sub>2</sub>-(001)-STO nanocuboids [24], as shown in Figure 2.10(b). Over 1 to 5 cycles of ALD, the Pt nanoparticles grow to 2 - 3 nm in diameter and have an interparticle spacing of 4 - 8 nm. The growth of ALD-Pt on the STO nanocuboids follows the nucleation and growth model, as observed by Christensen et al. [24] and Wang et al. [26,46]. Most importantly, the loading, crystalline size, interparticle distance, and chemical states of the Pt nanoparticles can be controlled as a function of the number of ALD cycles. High resolution electron microscopy showed that ALD-Pt exhibits a thermodynamically stable shape and cube-on-cube epitaxy on the TiO<sub>2</sub>-(001)-STO nanocuboids [69].

The ensemble of Pt/STO nanocuboids allows the system to be tested under catalytic reaction conditions in lab-scale reactors. In the past, propane oxidation [10], acrolein hydrogenation [25], and CO oxidation [26] reactions have been carried out over the Pd/STO catalyst. Enterkin et al. showed Pt maintained a very narrow size distribution after the propane oxidation reaction [10]. The particles only grew slightly from 3 - 4 nm to 4 - 5 nm in size. Additionally, in the propane oxidation reaction, Pt on STO nanocuboid supports generally showed higher activity and improved stability compared to Pt on commercial  $\gamma$ -Al<sub>2</sub>O<sub>3</sub> supports. This increased activity and stability is attributed to the strong epitaxy between Pt and STO.

Compared to ALD-Pt, however, less is known about the growth of ALD-Pd on STO

surfaces, especially at the initial growth stages. The growth and morphology evolution of ALD-Pd will be discussed in Chapter 4 and 5. In addition, the influence of Pd morphology on the CO oxidation catalytic activity will be presented in Chapter 5.

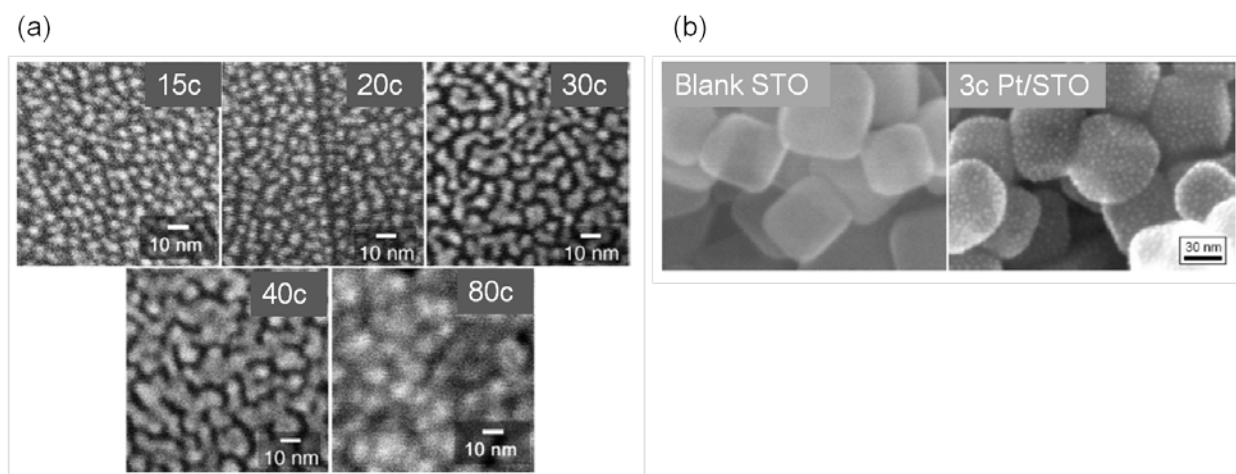


Figure 2.10 (a) SEM images of 15, 20, 30, 40, and 80 cycles of Pt ALD on an STO(001) single crystal support. Pt nanoparticles nucleate, grow and coalesce with increasing ALD cycles. Film closure occurs at 40 ALD cycles. (b) SEM images of TiO<sub>2</sub>(-001)-STO nanocuboids before and after 3 cycles of Pt ALD deposition. Pt disperses uniformly on all exposed surfaces of the STO nanocuboids. (Source: (a) and (b) adapted from Ref. [31] and [24], respectively.)

## 2.3 Correlating Nanoparticle Shape with Catalytic Performance

### 2.3.1 Winterbottom Construction Shapes

The equilibrium shape of a supported nanocrystal on a substrate can be predicted by the Winterbottom construction [39], which is an extension of the Wulff construction [92,93] with the consideration of the nanoparticle/substrate interface. Based on Wulff construction, the

equilibrium shape of free-standing nanocrystals can be identified by the minimization of surface free energy, as shown by the schematic diagram in Figure 2.11 (a). Figure 2.11 (b) shows the three dimensional Wulff shape of a Pd nanocrystal determined by minimizing the surface energy. The construction demonstrates the predominant (001) and (111) facets, which is consistent with the Pd nanocrystal observed in experiments [94].

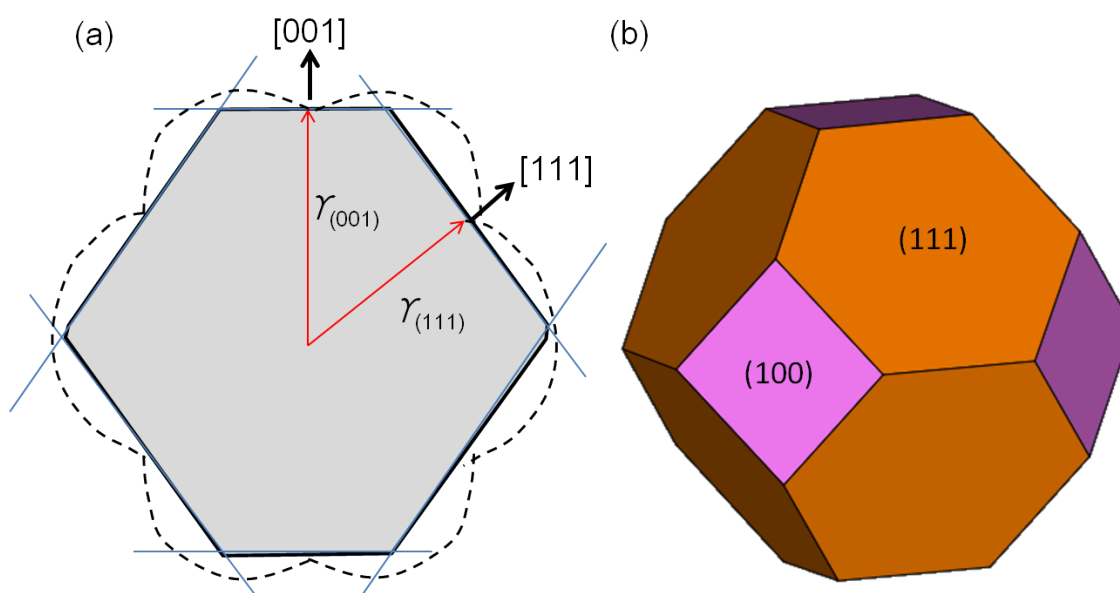


Figure 2.11 (a) Diagram for generating the Wulff shape of a crystal. Each red vector is constructed along an  $hkl$  surface normal direction with a length proportional to the surface energy. The dashed lines are vector end points in variable directions. The inner envelope (thin blue lines) of these perpendicular planes defines the thermodynamic equilibrium crystal shape (thick black lines).  $\gamma_{(001)}$  and  $\gamma_{(111)}$  are the surface energies of Pd (001) and (111). (Source: adapted from Refs. [93] and [94]). (b) A 3D model of the Wulff shape of Pd generated by Wulff Maker [95] based on the surface energies of Pd calculated in Ref. [96] (1.64 and 1.86 J/m<sup>2</sup> for Pd(111) and (001)).

The interface between the nanoparticle and support produces an additional interfacial energy term ( $\gamma_A$ ) caused by adhesion. Thus, the effective interfacial free energy ( $\gamma_{Int}$ ) is represented as  $\gamma_{Int} = \gamma_A + \gamma_i$ , where  $\gamma_i$  is the free energy of the nanoparticle. The total interfacial energy is determined by the chemical species, nanoparticle/support lattice misfit, and atomic structure at the interface [93].

As illustrated in Figure 2.12(a), the variation of the effective interfacial energy causes the Wulff shape of a nanoparticle to be truncated at different heights on the substrate and leads to different exposed areas of crystalline facets. The truncated shape of the supported nanoparticle is called the “Winterbottom shape.” Figure 2.12(b) demonstrates that the Winterbottom shape of Pt nanoparticles above the  $\text{TiO}_2$ -(001)-STO nanocuboid surface is slightly more than half of the Wulff shape. Such a result is consistent with the Winterbottom shape predicted by the reported values of the Pt/STO interfacial energy and STO(001) surface free energy [69].

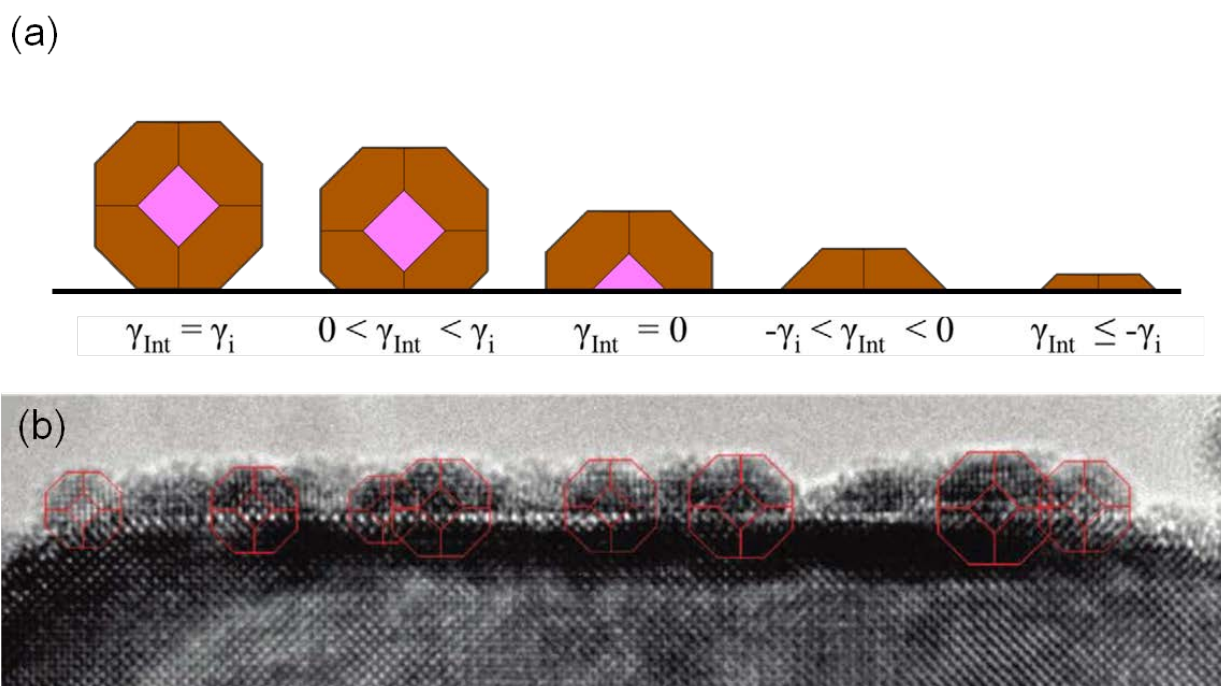


Figure 2.12 (a) Schematic of the variation in the shape of a Pd (or Pt) nanoparticle with (001) epitaxy on the surface, as a function of effective interfacial free energy ( $\gamma_{\text{int}}$ ). From left to right is the nanoparticle shows dewetting to wetting. The (111) and (001) facets of Pd are marked by orange and purple, respectively (Source: adapted from Ref. [93]). (b) HREM image of Pt nanoparticles supported on STO(001) surface of a  $\text{TiO}_2$ -(001)-STO nanocuboid. The red frame shows the Winterbottom shape of the Pt nanoparticles. (Source: adapted from Ref. [69].)

The shape of the truncated nanoparticles is able to influence its catalytic performance. The study by Enterkin et al. [25] shows that the Winterbottom shapes of Pt on  $\text{Ba}_x\text{Sr}_{1-x}\text{TiO}_3$  and STO surfaces affect the selectivity of the hydrogenation of acrolein towards an aldehyde or alcohol. The interface between Pt and  $\text{Ba}_x\text{Sr}_{1-x}\text{TiO}_3$  truncates the Pt at a lower height, resulting in a lower degree of wetting. Since aldehyde is a preferred product on lower coordinate sites (edges and

corners), the dewetted shape of Pt on the  $\text{Ba}_x\text{Sr}_{1-x}\text{TiO}_3$  surface leads to higher selectivity toward aldehyde. Compared to  $\text{Pt}/\text{Ba}_x\text{Sr}_{1-x}\text{TiO}_3$ ,  $\text{Pd}/\text{STO}$  shows higher degree of wetting and less low-coordinated sites, resulting in a higher selectivity toward alcohol.

This dissertation aims to study the shape effect of Pd on its catalytic activity. By utilizing STO nanopolyhedra with different surface terminations, the Winterbottom shape and the exposed facets of Pd is expected to be controlled, as shown in Figure 2.13.

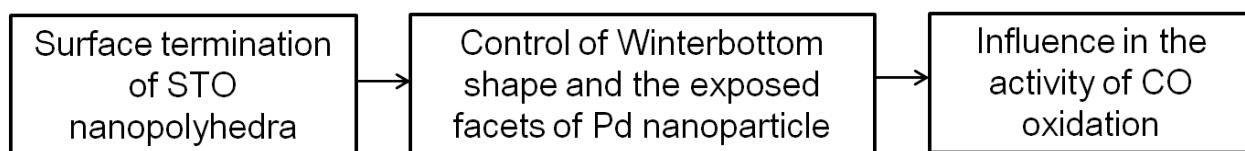
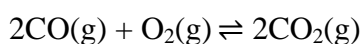


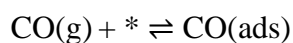
Figure 2.13 The objective of this dissertation.

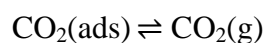
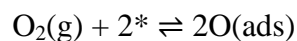
### 2.3.2 CO Oxidation as an Activity Probe

To determine the catalytic activity of  $\text{Pd}/\text{STO}$  nanopolyhedra catalysts, the CO oxidation reaction:



is established as a probe reaction. CO oxidation has been widely used as a benchmark reaction, as discussed in the review article by Freund et al. [97]. The CO oxidation on PGM catalysts follows the Langmuir-Hinshelwood mechanism [98–101]. The mechanism involves the adsorption and decomposition of the reactants and can be described by the following equations (Figure 2.14) (\* indicates a free adsorption site):





Initially, the reaction involves the chemisorption of CO and O<sub>2</sub> molecules onto the surface. The O<sub>2</sub> molecules are dissociatively chemisorbed, and the O<sub>(ads)</sub> formed species interact with chemisorbed CO molecules to form CO<sub>2</sub>, as shown in Figure 2.14.

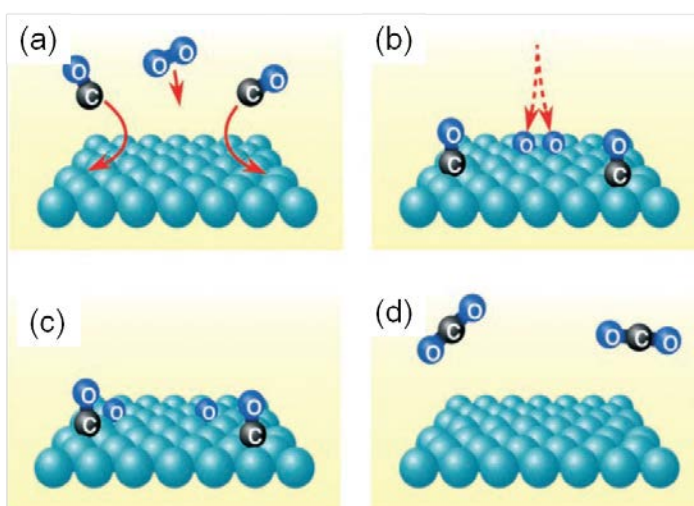


Figure 2.14 Schematic illustrations of the steps of CO oxidation over PGM surface: (a)

$\text{CO}(\text{g}) + ^* \rightleftharpoons \text{CO}(\text{ads})$ . (b)  $\text{O}_2(\text{g}) + 2^* \rightleftharpoons 2\text{O}^*(\text{ads})$ . (c)  $\text{O}^*(\text{ads}) + \text{CO}^*(\text{ads}) \rightleftharpoons \text{CO}_2^*(\text{ads})$ .

(d)  $\text{CO}_2^*(\text{ads}) \rightleftharpoons \text{CO}_2(\text{g})$  (Source: adapted from [57]).

CO oxidation is a structure-sensitive catalytic reaction. Studies have shown that the CO oxidation activity of Pd (Pt) depends upon the exposed crystal facets of free-standing Pd (Pt) nanoparticles. The Pt octahedra with (111) facets are significantly more active than Pt cubes with (001) facets toward CO oxidation in CO lean conditions (CO:O<sub>2</sub> = 1:40) [47]. A similar study on

Pd cubes and octahedra showed that the temperature required to achieve 50% conversion of CO is lower for Pd octahedra than for cubes. These results indicate that CO oxidation is more active on Pd(111) facets than on (001) facets [102].

## Chapter 3: Synthesis and Characterization Techniques

### 3.1 Hydrothermal Synthesis

Hydrothermal synthesis is a method that is used to produce inorganic mineral compounds. In the synthesis, the compounds crystallize from aqueous solutions (hydro-) at high vapor pressures and high temperatures (thermal-). Invented in the 19<sup>th</sup> century, hydrothermal synthesis was originally used for mineral extraction. Nowadays, it is used to commercially synthesize crystalline materials, such as metal oxide nanoparticles [103]. The synthesis requires an autoclave, which is a pressure vessel capable of maintaining elevated temperatures and pressures for the reaction.

In a typical synthesis, metal precursors such as metal chlorides, nitrates or acetates are added into the autoclave as aqueous solutions. A base (NaOH or KOH) is utilized as a pH controller, allowing the product to precipitate and stabilize. However, the growth mechanism is not yet well understood. The intermediate phases in the synthesis are difficult to characterize because autoclaves are sealed to maintain high pressures during the reaction. Sophisticated designs of autoclaves [104] are required to monitor the reaction during the thermal treatment process in the hydrothermal synthesis.

The synthesis of the three types of STO nanopolyhedra discussed in this dissertation follows similar procedures: Sr and Ti precursors were made into two separate solutions, which are denoted as solutions A and B, respectively. After solutions A and B were mixed and stirred, NaOH was added into the mixture to create a basic environment ( $\text{pH} \approx 14$ ) for STO growth. Then, the solution was transferred into a Teflon-lined container and sealed in a stainless steel autoclave. The autoclave was thermally treated with a controlled ramping rate and holding time.

In Chapter 6, the synthesis methods of the three types of STO nanopolyhedra studied in this dissertation will be presented in detail.

### **3.2 Atomic Layer Deposition (ALD)**

The ALD deposition discussed in this dissertation was performed by Cassandra George. The Pd ALD process was conducted in a viscous-flow ALD reactor as reported by [40]. Before ALD growth, the STO nanocuboids were heated in the ALD reactor at 200 °C for 10 min in nitrogen gas to equilibrate the temperature of the STO nanopolyhedra. This was followed by ozone treatment at 200 °C for 30 min to remove surface carbon. Pd(II) hexafluoroacetylacetonate ( $\text{Pd}(\text{hfac})_2$ ) and formalin (HCHO) were used as the precursors in the ALD process. The reactant exposures lasted 300 s for each precursor, and nitrogen purges of 300 s were performed in between each precursor exposure and after the last exposure. After ALD processing, the samples were removed from the reactor and cooled in the air. Samples were prepared with 1, 5, and 10 ALD cycles (denoted as 1c, 5c, 10c). The Pd/STO samples were in the form of dry powder, with a gray-scale color gradient that was darker for increased cycles of Pd.

### **3.3 X-ray Characterization Techniques**

#### **3.3.1 Introduction**

X-ray characterization techniques provide atomic-scale structural and chemical information about the sample of interest. The information obtained by X-ray scattering techniques includes the morphology, crystal structure, and domain size of nanocrystals. X-ray spectroscopy, on the other hand, provides information related to the chemical environment, such as the elemental fingerprint, oxidation states, and local coordination environment of the element of interest.

For advanced X-ray measurement techniques, an X-ray source with adjustable incident energy is necessary to reach different analysis depths or to obtain energy-continuous spectrum. In addition to that, when analyzing trace amounts of the element/phase of interest, a bright light source is necessary to increase the signal-to-noise ratio. A synchrotron light source was developed to fulfill these requirements. It provides a tunable and bright X-ray source with a small beam size. The synchrotron source makes it possible to probe much weaker signals and achieve higher resolution in the surface structure. In addition, the high brightness significantly reduces the time required to collect weak signals.

The X-ray characterization techniques applied in this dissertation include small-angle X-ray scattering (SAXS), X-ray absorption spectroscopy (XAS), X-ray fluorescence (XRF), and X-ray photoelectron spectroscopy (XPS).

### 3.3.2 Small Angle X-ray Scattering (SAXS)

SAXS is a global probe to reveal the structure of nanoparticles in terms of average sizes, shapes and packing arrangements of scattering objects with dimensions ranging from 1 to 100 nm. The scattering of X-rays at small angles provides the structural information on inhomogeneities of the electron density. In this dissertation, small-angle X-ray scattering (SAXS) measurements were applied to complement local probes such as TEM to measure the morphology of the sample.

When the incident X-ray is scattered by a particle, the scattering vector  $\vec{q}$  is defined by the momentum transfer of the incident ( $\vec{k}_0$ ) and scattered wave vectors ( $\vec{k}$ ) by:

$$\vec{q} = \vec{k} - \vec{k}_0 \quad (3.1)$$

The magnitude of the scattering vector  $\vec{q}$  is

$$q = |\vec{q}| = 4\pi \sin\theta / \lambda \quad , \quad (3.2)$$

where  $\theta$  is half of the scattering angle ( $2\theta$ ), and  $\lambda$  is the wavelength of the incident photon.

The scattered intensity is determined by the electron density distribution  $\rho(q)$  of a scattering object, and is given by

$$I(q) = |A(q)|^2 S(q) \quad , \quad (3.3)$$

where  $A(q)$  is the form factor of an isolated object, and  $S(q)$  is the structure factor arising from the interference of scattering from an ordered arrangement of distinct objects. When there is negligible interaction between the scattering objects (dilute conditions),  $S(q)$  can be approximated as 1, and the intensity becomes  $I(q) = |A(q)|^2$ . Amplitude of  $A(q)$  from a single object with volume  $v$  can be calculated as

$$A(\vec{q}) = \int_v \rho(\vec{r}) s(\vec{r}) e^{-i\vec{q}\cdot\vec{r}} d\vec{r} \quad , \quad (3.4)$$

where  $\vec{r}$  is the position vector,  $\rho(\vec{r})$  is the electron density, and  $s(\vec{r})$  is a function related to the shape (e.g., sphere, cylinder...) of an individual scatterer. Thus,  $A(q)$  can be modeled by the shape, dimension, and electron density profile of the scattering objects. Equation (3.3) can be expanded by the power series

$$I(q) = \rho_0^2 v^2 e^{-\frac{1}{3}q^2 R_g^2} \quad , \quad (3.5)$$

where  $\rho_0$  and  $v$  are the average electron density and volume of the scatterers, and  $R_g$  is the radius of gyration of the object, which is a measure of the distribution of electron density of the scattering object from its center of gravity and is defined as

$$R_g^2 = \frac{\int r^2 \rho(r) dr}{\int \rho(r) dr} \quad , \quad (3.6)$$

Equation (3.5) is usually referred to as the Guinier Law [105]. By plotting  $\log(I(q))$  versus  $q^2$  as a linear function in lower  $q$  region,  $R_g$  can be obtained from the slope of the function.  $R_g$  is an important parameter in SAXS analysis because it is related to the shape and dimension of the scattering objects. For the simplest example, i.e., a sphere with uniform density with radius  $R$ ,  $R_g$  is calculated as

$$R_g = \sqrt{\frac{3}{5}}R \quad . \quad (3.7)$$

For more complex objects, such as an ellipsoid of half axes  $a$ ,  $b$ , and  $c$ ,

$$R_g = \frac{1}{\sqrt{5}}(a^2 + b^2 + c^2)^{1/2} \quad . \quad (3.8)$$

In higher  $q$  region, the behavior of  $I(q)$  can be approximated by Porod's Law [105],

$$I(q) \propto q^{-a} \quad , \quad (3.9)$$

where  $a$  is the interface and fractal dimension of the scattering objects, and can be obtained by plotting  $\log(I(q))$  against  $\log(q)$ . For one, two, and three dimensional objects,  $a$  is 1, 2, and 4, respectively.

When the concentration of the scattering objects increases to the extent that the interparticle interaction can no longer be ignored, thus  $S(q)$  cannot be approximated as 1.  $S(q)$  oscillates around 1 and gradually turns into a diffraction peak as the scattering objects pack into a crystal-like structure. This holds true if the objects are distributed within a coherence length of the X-rays ( $\sim 5$  microns, [106]), such as the case here for Pd nanoparticles because of the small dimensions (50 nm-1 micron) of the STO support. The average center-to-center spacing,  $D$ , can be calculated from the peak position  $q_P$  by

$$D = \frac{2\pi}{q_P} \quad (3.10)$$

To analyze SAXS data, especially extract the information in geometry and dimensions of the scattering objects, the Irena [107] and SANS [108] software packages provide tools for data reduction and various models of the shapes of basic scattering objects, including spheres, cylinders, and more complex core-shell structures.

### 3.3.3 X-ray Absorption Spectroscopy (XAS)

XAS is a tool used to analyze the electronic structure and local atomic coordination environment around selected elements in a material. The key physical quantity measured in XAS is the X-ray absorption coefficient ( $\mu(E)$ ), which is the probability that X-rays are absorbed by a specific material through the photoelectric effect as a function of the incident X-ray energy ( $E$ ). The probability that the X-ray being absorbed is governed by Beer's Law:

$$I = I_0 e^{-\mu(E)t} \quad , \quad (3.11)$$

where  $I$  is the intensity transmitted through the sample,  $I_0$  is the intensity of the incident X-rays, and  $t$  is the thickness of the material. The material and especially energy dependence of  $\mu$  provides the basis of XAS. Generally,  $\mu$  decreases smoothly as the X-ray energy increases. However, when the X-ray energy is equal to that of the binding energy of a core-level electron, the X-ray liberates the electron (called “photoelectron”) from the core-level. This leads to a sharp rise in  $\mu$ , which is called an “absorption edge.” An X-ray absorption spectrum records the intensity of  $\mu$  as a function of incident X-ray energies (Figure 3.1).

XAS is divided into two regions based on the energy range around the absorption edge. The features between -30 to 30 eV with respect to the edge energy are the "X-ray absorption near-edge structure (XANES)." The gradual oscillations above the XANES range are the

"extended X-ray absorption fine structure" (EXAFS). The XANES region contains the information about the occupation of the energy states, which is related to the oxidation state of the absorbing element. The EXAFS region provides the local atomic structure, such as the coordination number and bond length to the surrounding atoms.

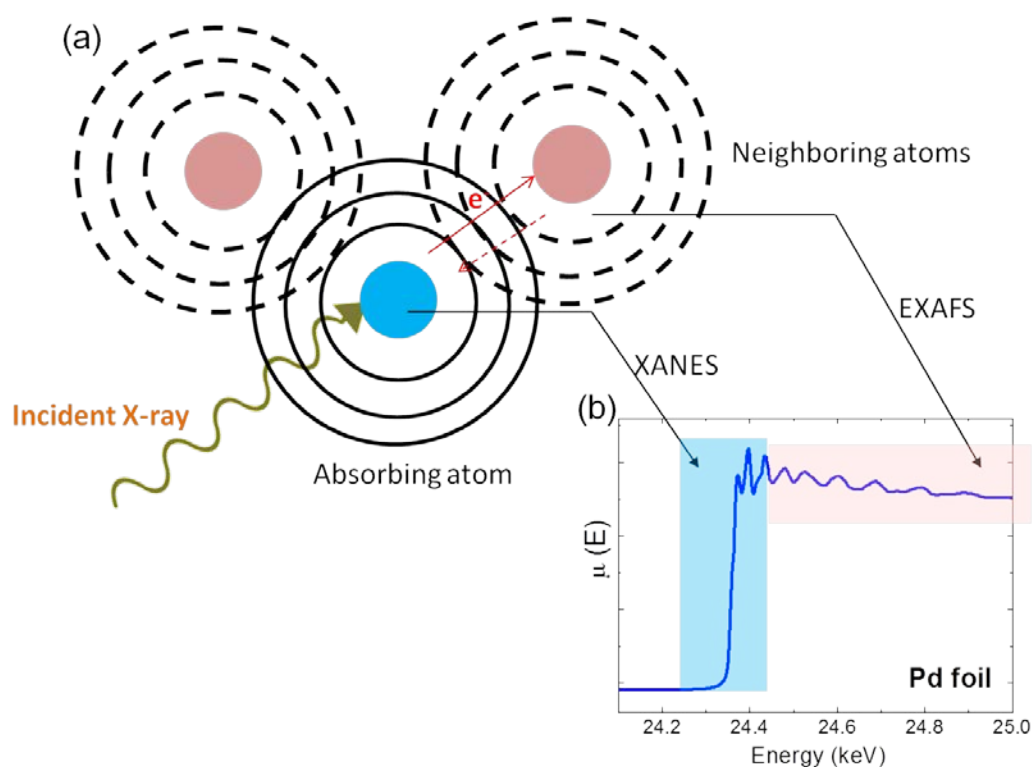


Figure 3.1 (a) Schematic diagram explaining the principle of XAS. The solid circle represents the wave function of the photoelectron produced during X-ray absorption. The dashed circles represent a further contribution when the photoelectron being scattered by the neighboring atoms. The interference between the initial and the scattered wave functions causes the oscillations in the EXAFS region. (b) A typical XAFS spectrum of a Pd foil at the Pd K-edge (24.35 keV). The XANES and EXAFS regions are identified in the figure.

In addition to the energy dependence, the absorption coefficient also depends strongly on the interaction between the photoelectron and the neighboring atoms near the absorbing atom (referred to as the “shell”). As shown in Figure 3.1, the outgoing electron wave from the absorbing atom can be backscattered by its neighboring atoms. The interference between the outgoing and the backscattered wave functions can either be constructive or destructive, depending on the distances and the electron wavelength. The interference results in oscillations above the absorption edge. Moreover, the configuration of the shells also modulates  $\mu(E)$ .

By analyzing the oscillations of  $\mu(E)$ , the local coordination structure can be obtained. In the following paragraphs, the steps of data reduction will be outlined. First, subtract and normalize the measured absorption coefficient ( $\mu(E)$ ) by comparing it to the absorption coefficient of an isolated atom ( $\mu_0(E)$ ). The superposition of the effect from the different nearest neighbor atom “shells,”  $\chi(E)$  is represented by:

$$\chi(E) = \frac{\mu(E) - \mu_0(E)}{\Delta\mu_0(E)} \quad , \quad (3.12)$$

where  $\mu_0(E)$  is a smooth background function from the absorption of an isolated atom, and  $\Delta\mu_0(E)$  is the jump in the absorption function at the absorption edge.  $\chi(E)$  can be converted to  $\chi(k)$  by

$$k = \sqrt{\frac{2m(E - E_0)}{\hbar^2}} \quad , \quad (3.13)$$

where  $E_0$  is the energy of the absorption edge, and  $m$  is the mass of an electron. When plotting  $\chi(k)$ , the  $\chi(k)$  is usually multiplied by  $k$ ,  $k^2$  or  $k^3$ . This is called  $k$ -weighting, which helps emphasize the features of  $\chi(k)$  in the higher  $k$  region in order to obtain an even oscillation throughout the  $k$ -region of interest. The  $k$ -weighted  $\chi(k)$  diagram is the superposition of several sinusoidal waves, usually with a dominating wave and several smaller waves. These sinusoidal

waves correspond to the scattering between the electron from absorbing atom and its neighbors located at different bond distances ( $R_j$ ). By employing the Fourier transform, the sinusoidal waves in  $\chi(k)$  can be deconvoluted and represented as multiple peaks in real space (usually called “R-space”). The  $\chi(k)$  corresponds to the combination of different near-neighbor coordination shells, which can be modeled as a sum over the  $j^{\text{th}}$  coordination shells:

$$\chi(k) = \sum_j \frac{N_j S_0^2 f_j(k) e^{-2k^2 \sigma_j^2}}{k R_j^2} \sin[2k R_j + \delta_j(k)] \quad , \quad (3.14)$$

where  $E_0$  is the absorption edge energy,  $N_j$  is the coordination number,  $S_0^2$  is the amplitude reduction factor,  $f_j(k)$  is a factor related to the probability of the photoelectron scattering from the  $j^{\text{th}}$  neighboring atom,  $R_j$  is the distance to the neighbor atom,  $\sigma_j$  is the EXAFS Debye-Waller factor that accounts for both structural and thermal disorder,  $\delta_j$  is the phase shift resulting from the scattering process.

Through EXAFS modeling (usually referred to as "fitting"), important local structural parameters, such as  $E_0$ ,  $N_j$ ,  $R_j$ , and  $\sigma_j$  can be determined. Note that  $\chi(R)$  is *not* a radial distribution function. Due to the "phase shift" term,  $\sin[2k R_j + \delta_j(k)]$ , in eq. (3.14), the position of the Fourier transformed peaks are not the real distances of the atomic shell and should be determined by EXAFS modeling. Because a range of incident X-ray energies is needed to create XAS spectra and a broad energy range is required to study a variety of elements, a synchrotron radiation X-ray source was used for measurements.

Two methods to measure  $\mu(E)$ , include transmission and fluorescence (Figure 3.2) methods. For concentrated samples, in which the element of interest is dominating, the transmission method is normally used. It simply involves measuring the X-ray flux by ion chambers, before

and after the X-ray beam passes through a uniform sample. From Beer's law, the transmitted flux  $I$ , is related to the incident flux by  $I/I_0 = \exp(-\mu(E))$ , or  $\mu(E) = \ln(I_0/I)$ . For dilute samples, the transmission signal may be too weak for transmission mode. In this case, fluorescence mode measurement is required. The fluorescence mode measures the incident X-ray flux  $I_0$  and the fluorescence X-rays emitted ( $I_f$ ) after the absorption.  $\mu(E)$  is proportional to  $I_f/I_0$ .

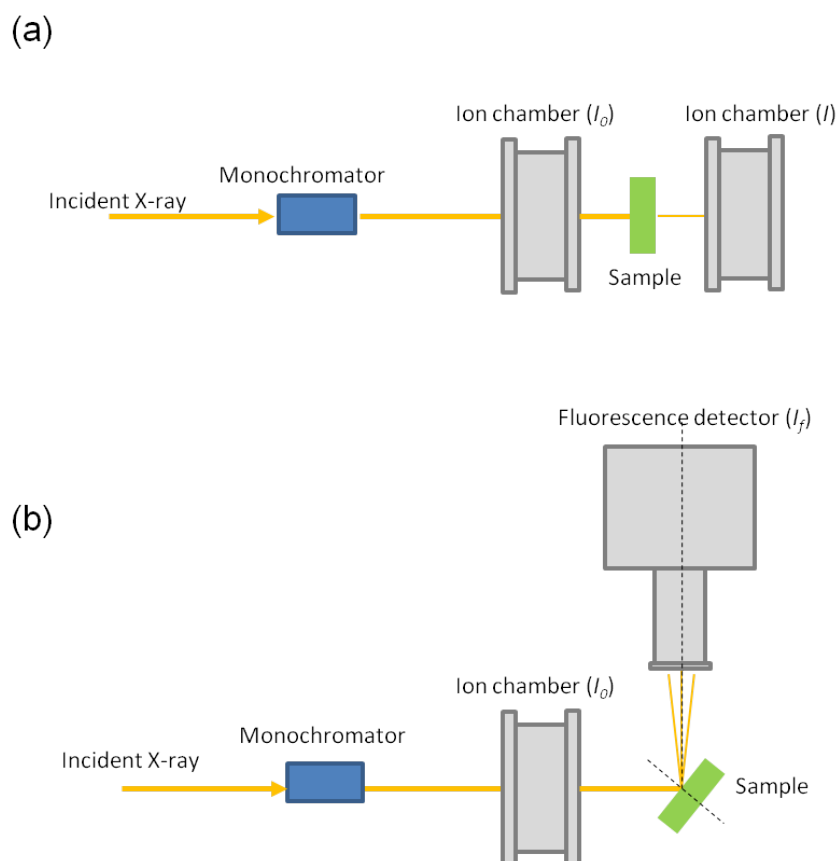


Figure 3.2 Schematic illustrations of the top-views of the two measurement modes of XAS. (a) Transmission mode and (b) Fluorescence mode. The monochromator consists of a pair of Si(111) single crystals that are scanned at an incident angle to scan the desired XAS energy range. Note that in the fluorescence mode, the X-ray fluorescence is collected in a direction parallel to the polarization direction to minimize the count-rate of elastic and inelastic scattered X-rays in the fluorescence detector. Because the synchrotron radiation is polarized in the horizontal plane, the X-ray fluorescence detector is set up at  $90^\circ$  angle to the incident beam in the horizontal plane to minimize the intensity from elastically scattered X-rays. Additionally, the sample is placed such that the beam incidence and exit angles are both  $45^\circ$ .

### 3.3.4 X-ray Fluorescence (XRF)

XRF is the emission of characteristic fluorescent X-rays from a material that has been excited by X-rays. As shown in Figure 3.3, when an electron at inner electron orbital is removed by an incident X-ray with energy higher than the binding energy of the orbital, a hole is created, leaving the atom in an excited state. Electrons from higher energy orbital can fill the hole and return the atom to the ground state. The radiative decay produces characteristic X-ray fluorescence, for which the photon energy is equal to the energy difference between the two levels involved. Because the energy levels between the different energy levels are element-distinctive, the characteristic fluorescence X-ray can be used to identify the chemical compositions in a specimen.

There are specific types of allowed XRF transitions that occur which are governed by the selection rules, each transition having its own specific energy. The three main types of transitions are K, L, and M, corresponding to the shell from which the electron was removed. K series emission lines have the highest energy, followed by L and M. Transitions in the specific series are denoted by the higher energy shell ( $\alpha$ ,  $\beta$ ,  $\gamma$ ...) followed by the sub-energy level (1, 2, 3...). For example,  $K\alpha_1$  is the transition from  $L_3$  to  $K_1$ . A complete database of K, L, and M X-ray line energies are available in Ref. [109].

XRF can be used in determining the atomic ratios of two elements of interest in the sample (denoted as A and B) in a specimen by comparing the XRF yield of A and B ( $Y_x$ ). The atomic ratio can be determined by the following equation:

$$\frac{N_A}{N_B} = \frac{Y_A}{Y_B} \frac{\sigma_B}{\sigma_A} \frac{\eta_B}{\eta_A} \frac{T_B}{T_A} \quad , \quad (3.15)$$

where  $\sigma_x$  is the XRF cross-section calculated by the XRF\_XSECT program [110],  $\eta_x$  is the detector efficiency, and  $T_x$  is the transmission factor as the X-ray emission passes from the sample to detector (approximated as 1 in air).

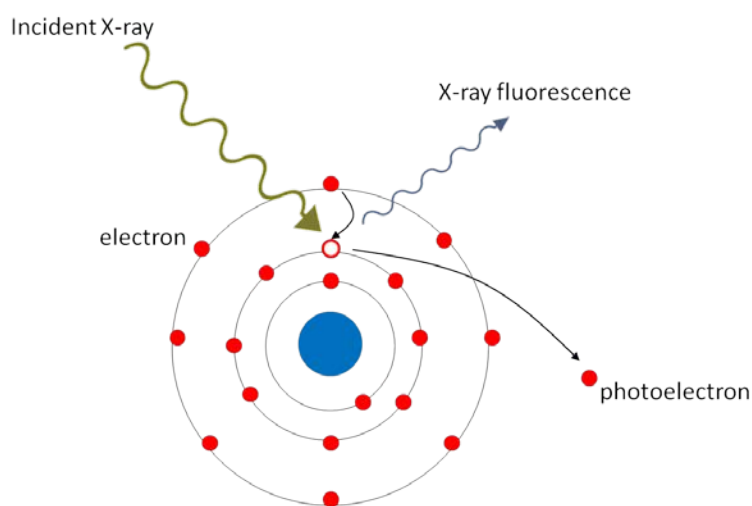


Figure 3.3 The schematic illustration of the interaction between an incident X-ray and an atom producing an emitted photoelectron followed by an X-ray fluorescent photon.

### 3.3.5 X-ray Photoelectron Spectroscopy (XPS)

Compared to XRF, XPS is a surface-sensitive method for examining chemical species and their oxidation states. In XPS experiments, X-rays with photon energies ranging from 100-1500 eV are used to irradiate the surface. The incident photons can be generated from conventional X-ray sources (Al or Mg targets) or synchrotron radiation sources. These energetic photons

penetrate the surface to a depth of 10-1000 nm based on the X-ray absorption length ( $1/\mu$ ). The emitted photoelectrons interact very strongly with matter and have an effective mean free path before undergoing an inelastic collision ranging from 0.5 to 10 nm. This makes the photoelectron process very surface sensitive in comparison to XRF. As shown in Figure 3.3, interaction between an incident X-ray and atom leads to a photoelectron, which is subsequently collected by an analyzer. Through energy conservation, the measured kinetic energy of the photoelectron is the incident photon energy minus the initial state binding energy and the work function of the analyzer, as described in the following equation:

$$E_b = h\nu - E_k - \phi \quad , \quad (3.16)$$

where  $E_b$  is the binding energy of the electron in the core level,  $h\nu$  is incident photon energy,  $\phi$  is the work function of the analyzer, and  $E_k$  is the kinetic energy of the emitted photoelectron. Therefore, by measuring the photoelectron kinetic energy, it is possible to obtain the electron's initial state, and thereby other information about the chemical state.

An important advantage of XPS is its ability to acquire the information of chemical states from the chemical shift of the core-level binding energy, which is very sensitive to the chemical environment around the element. When there is removal or addition of electronic charges due to changes in the chemical bonding environment, the electron shielding will alter and cause the binding energy to increase or decrease. For example, for elements with a higher oxidation state, its core-level peaks shift to the higher-binding energy side. This ability to discriminate between different oxidation states and chemical environments is a major strength of XPS.

The analyzing depth of the photoelectron ranges from 0.5 nm to 10 nm, depending on  $E_k$ . The incident photon energy is known and the kinetic energy of the photoelectron is detected with

high accuracy. The work function (depends on both the sample and the detector) can be determined with sufficient accuracy by calibration with a core-level peak and with known energy (ex: Carbon 1s peak at 285 eV).

### **3.4 Other Characterization Techniques**

#### **3.4.1 Transmission electron microscopy (TEM) and high resolution electron microscopy (HREM)**

TEM images were obtained with the help of Lawrence A. Crosby, Yuyuan Lin, Linhua Hu, and Xianyi Hu using the JEOL JEM-2100 FasTEM and the Hitachi H2300 STEM located in the EPIC facility of the NUANCE Center at Northwestern University (NU). High-resolution electron microscopy (HREM) images were taken by Lawrence A. Crosby with the JEOL JEM-2100 FasTEM at Northwestern University and the JEOL JEM-ARM200CF model in the Research Resources Center at the University of Illinois, Chicago (UIC).

For the preparation of TEM samples, approximately 2 mg of the Pd/STO sample was dispersed into ethanol and sonicated for at least 1 hr, obtaining a well-dispersed suspension. Then, a drop of the suspension was added onto a 400 mesh Cu TEM grid coated with carbon film (Ted Pella) before the measurement.

#### **3.4.2 Diffuse Reflectance Infrared Fourier Transform Spectroscopy (DRIFTS)**

DRIFT spectroscopy is a branch of infrared (IR) spectroscopy that works specifically on powdered samples with little to no sample preparation. It has been shown to be more sensitive to surface species than traditional IR transmission measurements and to be an excellent in-situ

technique in catalyst studies. An important advantage of DRIFTS is its minimal sample preparation. Contrary to transmission mode IR, which requires catalyst samples to be compressed into pellets, DRIFTS measures the samples directly as powder. Measuring the powder sample directly not only minimizes changes in the sample morphology and surface properties during the sample preparation, but ensures that the sample has good contact with the reaction gas during in-situ measurements [111].

DRIFTS operates by directing the IR beam into a cup-shaped sample holder filled with the sample or a mixture of the sample with an IR transparent matrix. The IR is either directly reflected by the surface of the sample as specular reflection, or undergoes multiple diffuse reflections that occur at the surface of the powder [112], as shown in Figure 3.4. The diffuse reflectance components contain information about the absorption properties because the IR travels predominantly through the surface of the particles. The diffuse reflectance IR signal is then collected by mirrors and sent to the detector.

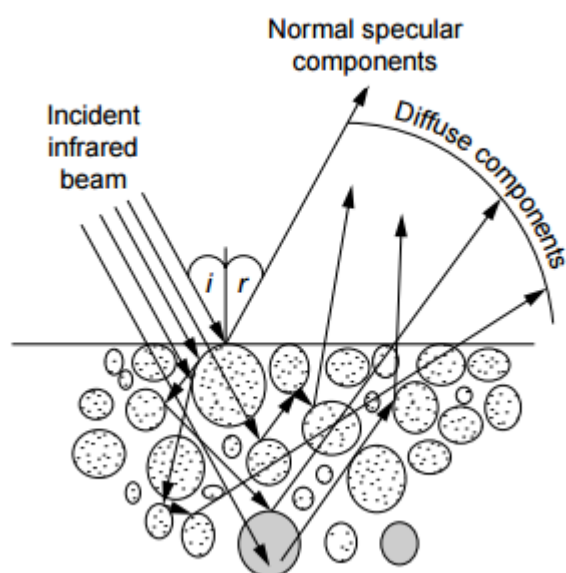


Figure 3.4 A schematic diagram of IR interacting with powder and generating diffuse reflection (Source: adapted from Ref. [112]).

### 3.4.3 Metal Dispersion of Pd Nanoparticles

“Metal dispersion (*Disp.*)” describes the fraction of surface atoms to the total number of atoms in nanoparticles by

$$Disp. = N_s / N_T , \quad (3.17)$$

where  $N_s$  is the number of metal atoms present on the surface, and  $N_T$  is the total number of metal atoms in the nanoparticle. Dispersion can be determined by either CO pulse adsorption methods or estimated from the average diameter of the nanoparticles.

CO pulse chemisorption determines the active surface area of metal by successive injection of equal volumes of pulsed CO gas to the sample. The total adsorbed volume of CO can be

calculated from the area under the TCD peaks, and can then be converted to the number of CO molecules precisely by the ideal gas law ( $PV = nRT$ ). The CO adsorbs onto the metal surface stoichiometrically, from which the numbers of the surface metals can be determined. There is a one-to-one relationship between Pt and CO, but a two-to-one relationship for Pd and CO [113].

Other than CO pulse chemisorption, the metal dispersion can also be estimated from the diameter of a (assumed to be) spherical or hemispherical nanoparticle with crystallinity [59,114]. For a hemispherical nanoparticle with diameter  $d$ , the surface area ( $A$ ) is  $A = \frac{1}{2}\pi d^2$  and the volume ( $V$ ) is  $V = \frac{1}{12}\pi d^3$ . The volume occupied by an atom ( $v_m$ ) in the bulk of crystalline metal is

$$v_m = M / \rho N_A \quad , \quad (3.18)$$

where  $M$  is the atomic mass,  $\rho$  is the density of the bulk metal, and  $N_A$  is Avogadro's number. The surface area occupied by an atom ( $a_m$ ) can be calculated from the number of atoms per unit surface area in the proportion of certain crystalline planes. Thus,  $Disp.$  can be calculated from (3.18) as the following equation:

$$Disp. = \frac{N_s}{N_T} = \frac{\frac{A}{a_m}}{\frac{V}{v_m}} = \frac{6}{d} \left( \frac{v_m}{a_m} \right) \quad (3.19)$$

### 3.4.4 Turnover Frequency of the CO Oxidation Reaction

The activity of CO oxidation over Pd is determined by using the turnover frequency (TOF). The TOF was defined as the frequency of CO conversion by surface Pd, in units of  $s^{-1}$ . [115]. In the case of CO oxidation over Pd, TOF is the frequency in which a *surface* Pd atom converts CO into  $CO_2$ , assuming all of the surface Pd atoms equally participate in the reaction. TOF has proven helpful in describing and comparing catalytic reactions on heterogeneous catalysts. The major advantage of using TOF is the normalization of the reaction rate to the amount of the active component. The normalization avoids the ambiguity caused by external factors such as the amount of catalyst used, loading of the active phase, and reactant gas flow rate [59,115]. Therefore, using TOF has made possible the comparison of rates measured on different catalysts.

The CO oxidation reaction was performed at the Clean Catalysis (CleanCat) Core Facility at Northwestern University using a BenchCAT 4000 reactor system. The system consisted of a 1/4" quartz tube plug flow reactor, a heating unit, and an Agilent 6850 gas chromatograph (GC) analyzer, as shown in Figure 3.5. The conversion of CO was measured under differential conversion conditions, in which the conversion was less than 20% to ensure that the concentration was approximately constant throughout the catalyst bed. All reaction runs were repeated at least three times, and average values of CO conversion were reported with standard deviations. The rate of CO consumption ( $r_{CO}$ ), or the TOF, can be represented by

$$r_{CO} = \frac{-X_{CO} F_{CO}}{N}, \quad (3.20)$$

where  $X_{CO}$  is the conversion of CO,  $F_{CO}$  is the molar flow rate of CO gas (mol./s), and  $N$  is the number of Pd atoms at the surface (mol.).  $X_{CO}$  can be plotted against  $(\frac{N}{F_{CO}})$ , and the slope of the

line leads to  $r_{CO}$  in units of  $s^{-1}$ . For the Pd/STO catalysts discussed in this dissertation,  $N$  is obtained by using the following equation:

$$N(\text{mol.}) = \frac{W_{\text{Pd/STO}}(\text{g}) \times \text{wt}\% \times \text{Disp.}(\%)}{106.4 \left(\frac{\text{g}}{\text{mol}}\right)}, \quad (3.21)$$

where  $W_{\text{Pd/STO}}$  is the total weight of the catalyst,  $\text{wt}\%$  is the mass loading of Pd,  $\text{Disp.}$  is the Pd dispersion, and 106.4 is the atomic mass of Pd.  $F_{CO}$  is calculated as

$$F_{CO} \left(\frac{\text{mol.}}{\text{s}}\right) = \frac{f \left(\frac{\text{mL}}{\text{min}}\right) \times 10^{-3} \times 1 \text{ (atm)} \times 0.5\%}{60(\text{s}) \times 0.082(\text{L} \cdot \text{atm} \cdot \text{mol}^{-1} \cdot \text{K}^{-1}) \times 298(\text{K})}, \quad (3.22)$$

where  $f$  is the flow rate of the CO mixture, and 0.5% is the percentage of CO in the reactant gas mixture.

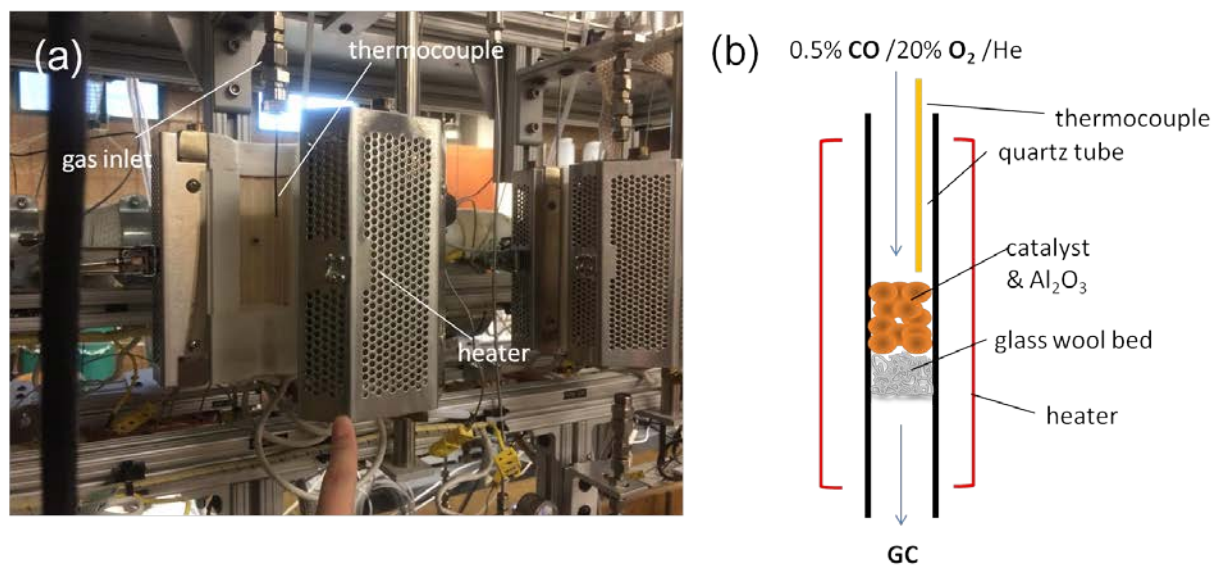


Figure 3.5 Setup of the CO oxidation reaction: (a) The BenchCAT 4000 reactor system. (b) Schematic illustration of the plug flow reactor.

## **Chapter 4: Morphological and Chemical Evolution of Pd Nanoparticles**

### **Supported on SrTiO<sub>3</sub> Nanocuboids**

#### **4.1 Introduction**

This chapter discusses the influence of surface chemical terminations on the morphology and chemical properties of supported Pd nanoparticles. Pd were grown by atomic layer deposition (ALD) on STO nanocuboid single crystals that were synthesized to have either a TiO<sub>2</sub>-(001) or SrO-(001) terminated surface. ALD is able to control the effective coverage, chemical state, and size of the Pd nanoparticles as a function of the number of ALD cycles, as demonstrated in the previous studies of ALD-Pt [10,24,26,31,33,46]. The Pd supported on the two types of STO nanocuboids were examined by transmission electron microscopy (TEM), X-ray absorption spectroscopy (XAS), and X-ray photoelectron spectroscopy (XPS) to reveal and compare their morphology, chemical states, and local atomic coordination structures.

#### **4.2 Experimental Methods**

##### **4.2.1 Sample Preparation**

Single crystal SrTiO<sub>3</sub> (STO) nanocuboids with well-defined (001) faces were synthesized to have predominantly SrO- or TiO<sub>2</sub>-terminated surfaces by acetic acid- [41] and oleic acid-assisted [43,44] methods respectively. The nanocuboids are in the form of a dry, white powder. High resolution transmission electron microscopy (HRTEM) experiments and density function theory (DFT) simulation were previously used to determine the surface termination of the STO nanocuboids [70]. The SrO-terminated STO nanocuboids were washed with ethanol then calcined in air at 450 °C for 3 h in order to remove the residual oleic acid ligands. Standard

Brunauer-Emmett-Teller (BET) analysis determined that the surface area was  $20 \text{ m}^2/\text{g}$  for the  $\text{TiO}_2$ -terminated nanocuboids, and  $61 \text{ m}^2/\text{g}$  for the SrO-terminated nanocuboids. In Figure 4.1, the mean edge length for the  $\text{TiO}_2$ -terminated nanocuboids is  $67 \text{ nm}$  with a standard deviation (SD) of  $12.5 \text{ nm}$ ; for the SrO-terminated nanocuboids, the mean is  $15 \text{ nm}$  with  $2.8 \text{ nm}$  SD. The  $\text{TiO}_2$ - and SrO nanocuboids discussed in this chapter was synthesized by Yuyuan Lin and Linhua He, respectively.

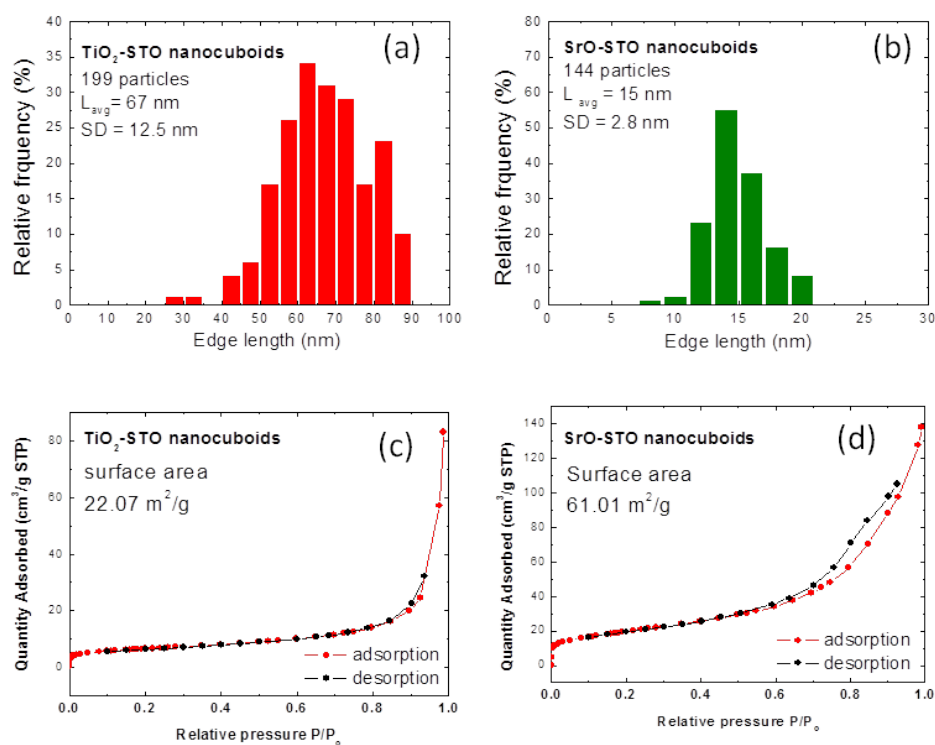


Figure 4.1 (a, b) Size distribution and (c, d) BET absorption curve for  $\text{TiO}_2$ -terminated and SrO-terminated STO nanocuboids.

The Pd ALD process was conducted in a viscous-flow ALD reactor [116]. Before ALD growth, both  $\text{TiO}_2$ -STO and pre-treated SrO-STO nanocuboids were heated in the ALD reactor at

200 °C for 10 min in nitrogen gas to equilibrate the temperature of the STO nanoparticles. This was followed by ozone treatment at 200 °C for 30 min to remove surface carbon. Pd(II) hexafluoroacetylacetonate ( $\text{Pd}(\text{hfac})_2$ ) and formalin (HCHO) were used as the precursors in the ALD process [89]. The reactant exposures lasted 300 s for each precursor, and nitrogen purges of 300 s were performed in between each precursor exposure and after the last exposure. After ALD processing, the samples were removed from the reactor and cooled in air. Samples were prepared with 1, 5, 10, and 20 cycles (denoted as 1c, 5c, 10c and 20c) of Pd ALD grown on the  $\text{TiO}_2$ -terminated STO nanocuboids, and with 1c, 5c, and 10c of Pd on the SrO-terminated nanocuboids. The Pd/STO samples were in the form of a dry powder, with a gray-scale color gradient that was darker for increased cycles of Pd.

#### 4.2.2 Morphology and Loading of Pd

The morphology of the as-deposited Pd/STO samples was examined using a JEOL 2100F TEM. The sizes and shapes of a large representative group of Pd nanoparticles for the 5c and 10c samples were measured using the ImageJ software [117].

The atomic ratio between Pd and Sr of the Pd/STO samples was measured by both inductively coupled plasma atomic emission spectroscopy (ICP-AES) and X-ray fluorescence (XRF). For ICP-AES, the Pd/STO sample was dissolved in aqua regia for 24 h, then analyzed by a Varian Vista MPX ICP Spectrometer. XRF measurements were performed at beamline 5BM-D at the Advanced Photon Source (APS) of Argonne National Laboratory with an incident photon energy of 24.4 keV. For both ICP and XRF measurements, the atomic ratio of Pd to Sr was directly obtained, and the wt% of Pd can be calculated from the stoichiometry of  $\text{SrTiO}_3$ . (See

Appendix B.1 for details.) Because the TiO<sub>2</sub>- and SrO-terminated STO nanocuboids have different surface areas, the Pd loadings on the different supports need to be normalized. Thus, "effective Pd coverage ( $\theta$ )" is defined to normalize the Pd loading. One monolayer of  $\theta$  is equal to the 2D density of Sr atoms on the STO surface. The value is  $1/(0.3905 \text{ nm})^2 = 6.56 \text{ nm}^{-2}$ .  $\theta$  can be calculated from the following formulation:

$$\theta = \frac{V_{STO}}{a_{STO}^3} / \left( \frac{N_{Sr}}{N_{Pd}} \times \frac{S_{STO}}{a_{STO}^2} \right) \quad (4.1)$$

where  $V_{STO}$  is the volume per gram of the STO nanocuboids,  $S_{STO}$  is the specific surface area of the STO nanocuboids measured by using BET,  $a_{STO}$  is the lattice constant of bulk STO (3.905 Å), and  $N_{Sr}/N_{Pd}$  the atomic ratio obtained by using both ICP and XRF measurements.

### 4.2.3 XANES and EXAFS Measurements

All the X-ray absorption near edge structure (XANES) and extended X-ray absorption fine structure (EXAFS) measurements were completed at the DuPont-Northwestern-Dow (DND) beamline 5BM-D at the APS. The Pd atom oxidation state(s) and its local atomic coordination structure were analyzed by XANES and EXAFS, respectively. These *ex-situ* (open air) XANES and EXAFS measurements of the as-deposited samples were carried out around the Pd K-edge (24.4 keV) in fluorescence mode with the sample under ambient atmosphere. Data processing was completed with the ATHENA and ARTEMIS software packages [118]. The coordination numbers ( $N$ ) of Pd–Pd and Pd–O bonds, Pd–Pd and Pd–O bond distances ( $R$ ), and Debye-Waller factors ( $\sigma$ ), were obtained by a least-squares fitting in R-space between 1-3.5 Å of the

$k^2$ -weighted Fourier transformed EXAFS data ( $k = 2.5-11 \text{ \AA}^{-1}$ ). Photoelectron scattering paths used in the fitting were based on the first nearest neighbors of Pd in FCC Pd (Pd–Pd) and tetragonal PdO (Pd–O) (Figure 4.7).

In addition to the above described *ex-situ* X-ray spectroscopy measurements, an X-ray flow cell [119] was employed for *in-situ* XANES and EXAFS experiments on a select set of samples. The Pd/STO sample was pre-reduced under flowing  $\text{H}_2$  at  $300 \text{ }^\circ\text{C}$  for 30 min to remove the Pd surface oxide, and the measurements were completed in an  $\text{H}_2$  flow at room temperature during the in-situ measurements. Additionally, to investigate the change of the Pd oxidation state under redox environments similar to a real catalytic reaction, *in-situ* XANES measurements were carried out by exposing the samples to redox atmospheres. The sample was heated to  $300 \text{ }^\circ\text{C}$  in the X-ray flow cell under pure  $\text{O}_2$  and held at that temperature for 30 min. Then, the cell was purged with  $\text{N}_2$  at a rate of  $10 \text{ mL/min}$  for 30 min and cooled to room temperature. The XANES measurements were completed in an  $\text{N}_2$  flow at room temperature. The reaction gas was then switched to  $3\% \text{ H}_2/\text{N}_2$ , and the procedure described above was applied to the  $\text{H}_2$  cycle. The  $\text{N}_2$  purge step after the  $\text{H}_2$  exposure removed the excess  $\text{H}_2$  in the cell, thus prevented Pd hydride formation.

#### 4.2.4 X-ray Photoelectron Spectroscopy Analysis

The surface species on the Pd/STO samples were analyzed with X-ray photoelectron spectroscopy (XPS, Thermo Scientific ESCALAB 250Xi) using a monochromatic Al  $\text{K}\alpha$  ( $1486.74 \text{ eV}$ ) X-ray source.

## 4.3 Results and Discussion

### 4.3.1 Morphology

Figure 4.2 presents TEM and high angle annular dark field (HAADF) images of the Pd/SrTiO<sub>3</sub> samples, which shows the Pd formed nanoparticles on the surface of the STO nanocuboids. The images of the 5c and 10c samples are representative and establish the morphology and growth trends of Pd nanoparticles on TiO<sub>2</sub>- and SrO-terminated surfaces of STO. The sizes and shapes of a large representative group of Pd nanoparticles for the 5c and 10c samples were measured using the ImageJ software [117]. The histograms for the nanoparticle diameters are shown in Figure 4.4 along with the statistical analysis determining the mean values for the diameters ( $\bar{d}$ ) and the standard deviations (SD). The shape of the Pd nanoparticle is described by an "aspect ratio," which is defined as the maximum height of the Pd nanoparticle perpendicular to the surface divided by the maximum width parallel to the surface, as shown in Figure 4.3(a). A smaller aspect ratio indicates that the Pd particle wets the surface more (i.e. flatter shape), and the larger aspect ratio indicates that the Pd particle shows more dewetting (i.e. rounder shape). For example, hemispherical nanoparticle has an aspect ratio 0.5, and that of a spherical nanoparticle is equal to 1.

On the TiO<sub>2</sub>-terminated STO surface, the shape of Pd nanoparticles is flatter, with a mean aspect ratio of  $\sim 0.6(1)$ , while Pd nanoparticles on the SrO-terminated surface have a higher aspect ratio  $\sim 0.8(1)$ , as shown in Figure 4.3 and Table 4.1. The difference in the wetting behavior provides some insight into the interfacial energy between Pd and the STO nanocuboids based on Winterbottom construction [39]. The smaller aspect ratios, or better

wetting, between Pd and the  $\text{TiO}_2$ -terminated surface indicates that the interfacial free energy of the Pd/ $\text{TiO}_2$ -STO interface is lower than that of the Pd/SrO-STO interface.

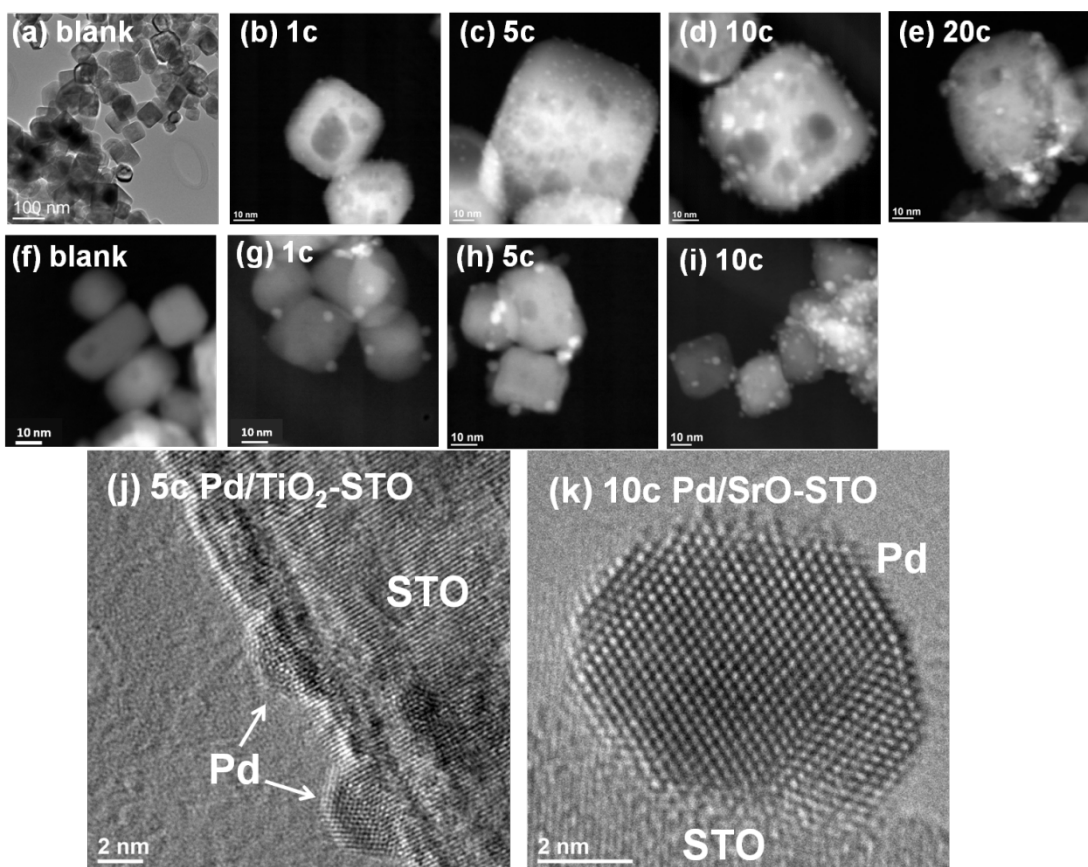


Figure 4.2 TEM and HAADF images of  $\text{TiO}_2$ -terminated (a-e) and SrO-terminated  $\text{SrTiO}_3$  (f-i) nanocuboids before and after ALD Pd deposition. Pd nanoparticles can be clearly seen from the images. HRTEM images in (j) and (k) show the details of the faceted Pd nanoparticles on  $\text{TiO}_2$ -terminated and SrO-terminated STO surfaces. A better wetting between Pd and the  $\text{TiO}_2$ -STO surface can be observed. (Images provided by: (a-e) Yuyuan Lin, (f-i) Linhua Hu, and (j, k) Lawrence A. Crosby.)

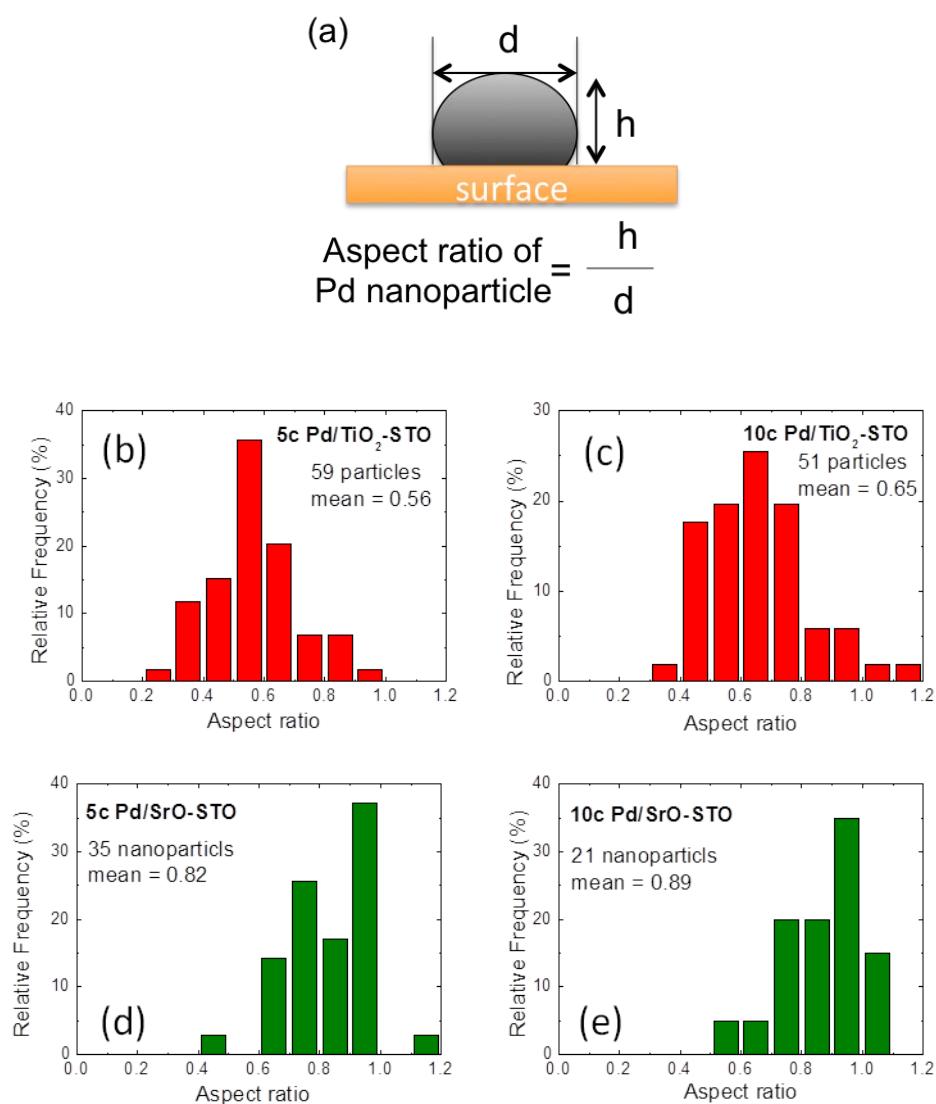


Figure 4.3 (a) Definition of the aspect ratio of a schematic Pd nanoparticle. (b-e) Distribution of the aspect ratio of Pd nanoparticles on  $\text{TiO}_2$ -terminated STO surface (b, c) and on SrO-terminated STO surface (d, e).

Table 4.1 The average aspect ratios of the 5c and 10c Pd nanoparticles.

		Average aspect ratio of Pd nanoparticles
Termination	# cycles	
TiO <sub>2</sub>	5c	0.56
	10c	0.65
SrO	5c	0.82
	10c	0.89

For the TiO<sub>2</sub>-STO surface, the 5c and 10c Pd samples have a SD of ~0.5 nm, which is narrower than the SD of 5c and 10c Pd on the SrO-STO surface, which is ~2 nm (Figure 4.4). From the TEM images in Figure 4.2, when the number of ALD cycles increase from 5c to 10c, Pd nanoparticles on the TiO<sub>2</sub>-terminated surface increase in average size, but the number of nanoparticles per unit area remains approximately constant. While Pd nanoparticles on the SrO-terminated surface increase in the number per area, the average size and size distribution are not substantially changed. This can be seen by comparing Figure 4.2(c) and (d) to Figure 4.2(h) and (i). Note that the TEM image analysis of the Pd nanoparticle shown in Figure 4.4 is unable to account for nanoparticles with diameters smaller than 1 nm. Schematic diagrams describing the morphology and evolution of Pd nanoparticles on the TiO<sub>2</sub>-and SrO-STO surfaces are shown in Figure 4.4(c) and (f).

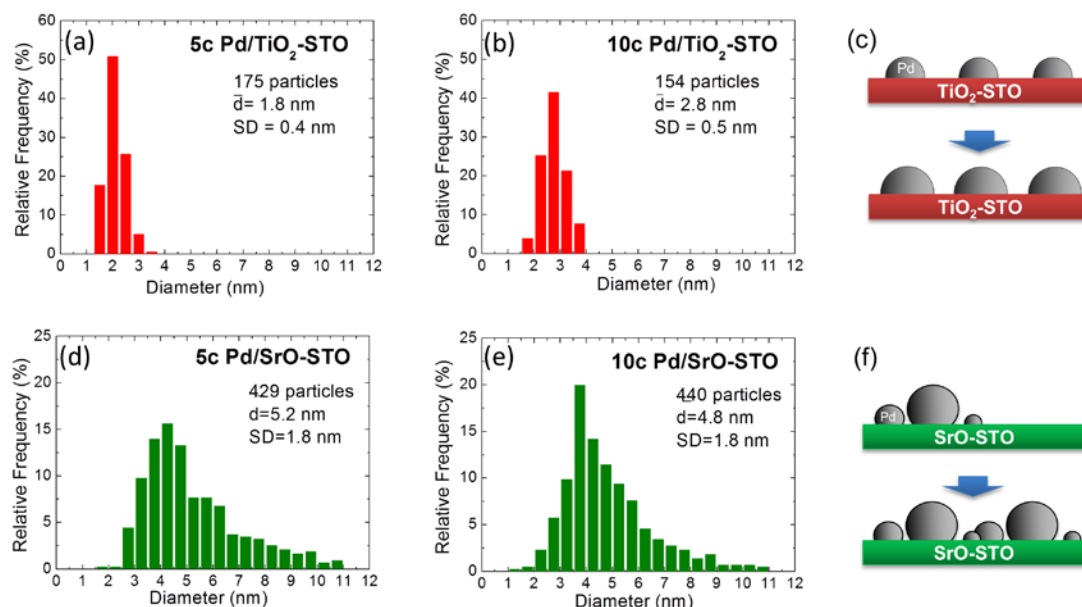


Figure 4.4 Histograms of Pd nanoparticle diameters extracted from TEM images: size distribution of 5c Pd/TiO<sub>2</sub>-STO (a), 10c Pd/TiO<sub>2</sub>-STO (b), 5c Pd/SrO-STO (d), and 10c Pd/SrO-STO (e). The mean diameter ( $\bar{d}$ ) and standard deviation (SD) values are included in the figure. Schematic representations of the morphology and evolution of Pd nanoparticles on TiO<sub>2</sub>- and SrO-terminated STO surface are shown in (c) and (f), respectively.

### 4.3.2 Pd Loading and Effective Coverage

The ICP-AES and XRF determined atomic ratios for Pd to Sr are listed in Table 4.2 along with the calculated Pd loading in wt% and effective Pd coverage (Detailed calculation in Appendix B.1). As expected for ALD, the Pd wt% loading exhibits approximately linear growth with the number of cycles. In order to compare the loading of Pd on two STO nanocuboids with different surface areas, the "effective Pd coverage ( $\Theta$ )" is utilized to normalize Pd loading in units of monolayer (ML). 1 ML is equivalent to one Pd atom per Ti or Sr surface atom on an

ideally terminated STO nanocuboid ( $6.56 \text{ nm}^{-2}$ ). Figure 4.5 and Table 4.2 shows  $\theta$  versus the number of ALD cycles. The higher  $\theta$  on the  $\text{TiO}_2$ -terminated surface implies that the interfacial free energy is more negative for Pd growth than on the SrO-terminated surface. This result is consistent with the fact that the Pd nanoparticle wets the  $\text{TiO}_2$ -terminated surface better than the SrO-terminated surface. The argument above is consistent with the TEM images shown in Figure 4.2.

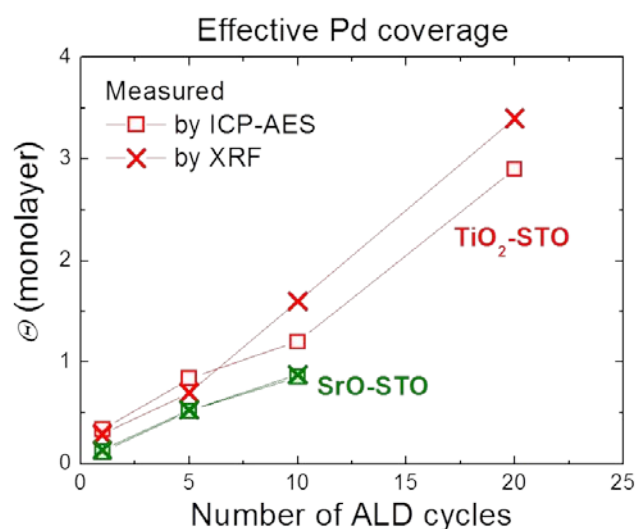


Figure 4.5 Effective Pd coverage ( $\theta$ ) increases almost linearly as the number of ALD cycles increases. One monolayer ( $\theta = 1\text{ML}$ ) coverage is defined as the 2D density of Sr atom in a SrO (001) atomic plane of STO ( $6.56 \text{ nm}^{-2}$ ).

Table 4.2 The atomic percentage ratio of Pd and Sr can be directly measured from both ICP-AES (inductively coupled plasma atomic emission spectroscopy) and XRF (X-ray fluorescence). Pd loading and the effective Pd coverage ( $\theta$ ) can then be calculated by assuming that the atomic ratio of Sr:Ti:O in the SrTiO<sub>3</sub> nanocuboids is exactly 1:1:3.

Termination	cycles	Pd/Sr (at% ratio)		Pd loading (wt%)		Effective Pd coverage, $\theta$ (ML)	
		ICP	XRF	ICP	XRF	ICP	XRF
<b>TiO<sub>2</sub></b>	<b>1c</b>	0.015	0.012	0.86	0.73	0.34	0.29
	<b>5c</b>	0.037	0.031	2.1	1.7	0.84	0.7
	<b>10c</b>	0.052	0.070	2.9	3.9	1.2	1.6
	<b>20c</b>	0.13	0.15	6.8	8.1	2.9	3.4
<b>SrO</b>	<b>1c</b>	0.014	0.016	0.86	0.94	0.12	0.14
	<b>5c</b>	0.063	0.064	3.5	3.6	0.52	0.53
	<b>10c</b>	0.11	0.11	5.8	5.9	0.86	0.88

### 4.3.3 Chemical State and Local Structure Analysis

The oxidation state of Pd species on STO is analyzed by XPS and XANES. Figure 4.6 shows the position of the Pd 3d core level peak is shifting toward to the lower binding energy (BE) side when the Pd loading increases. The shifting in the BE indicates that the chemical state of the Pd is transitioning from Pd<sup>2+</sup> to Pd<sup>0</sup>.

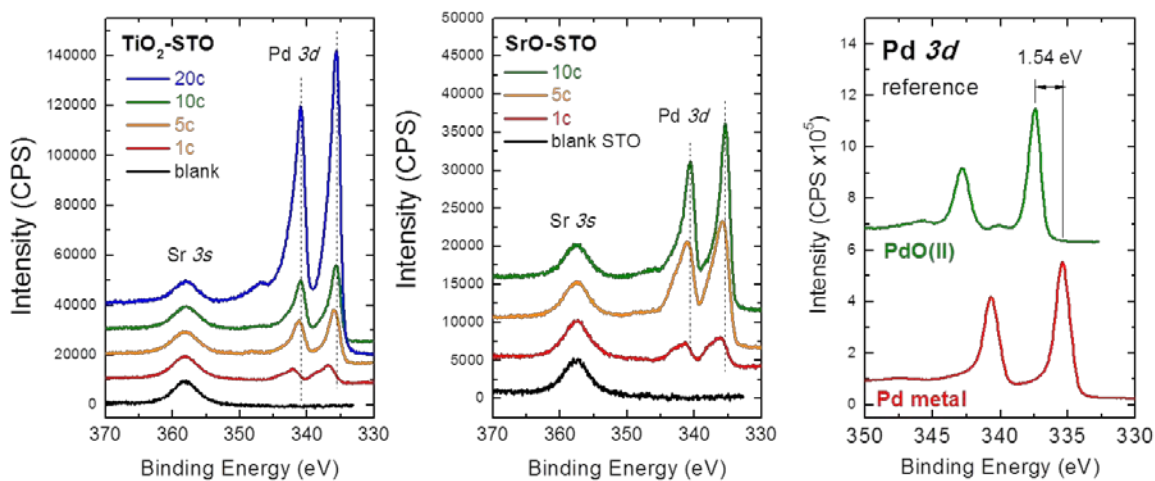


Figure 4.6 The Pd 3d core level doublet peak of the Pd/STO samples along with the reference spectra of Pd<sup>0</sup> and Pd<sup>2+</sup>, showing the position of Pd 3d shifts to the low BE region as the Pd loading increases.

The line shapes of the normalized XANES in Figure 4.7(a) indicate that Pd<sup>0</sup> and Pd<sup>2+</sup> co-existed on both types of surface terminations. With the increasing number of ALD cycles, the Pd chemical state shifts monotonically from Pd<sup>2+</sup> to Pd<sup>0</sup>. The result is consistent with the analysis by XPS. The best fit of the EXAFS data was achieved when using scattering path lengths based on the first nearest neighbors around the Pd atoms in the metallic face centered Pd and tetragonal

PdO structures determined by X-ray crystallography, as shown in Figure 4.7(c). The magnitudes of the Fourier transforms of the EXAFS spectra and the best fit to the first nearest neighbor coordination number ( $N$ ) are presented in Figure 4.7(b). As listed in Table 4.4, the number of O nearest neighbors to Pd diminishes and the number of Pd neighbors increases as the number of ALD cycles increases. In ALD cycle 1c, only the Pd–O peak appears, indicating that the 1c sample behaves like PdO on both TiO<sub>2</sub>- and SrO-terminated surfaces. After subsequent ALD cycles, the Pd–Pd peak grows at the expense of the Pd–O peak, indicating the presence of more Pd in the metallic state (Pd<sup>0</sup>). In addition, for the same number of ALD cycles, the fraction of palladium as Pd<sup>0</sup> is greater on the SrO-STO surface than on the TiO<sub>2</sub>-STO surface.

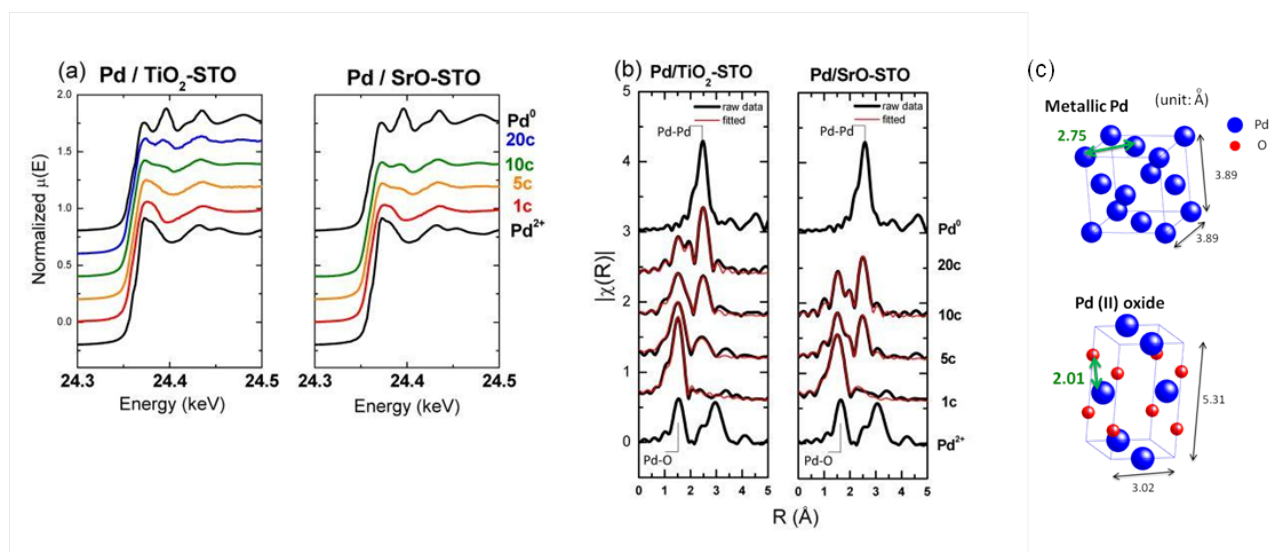


Figure 4.7 (a) The Pd K-edge X-ray absorption spectra for the ALD-Pd/STO samples with different numbers of ALD cycles. The Pd K-edge of a Pd foil ( $\text{Pd}^0$ ) and PdO ( $\text{Pd}^{2+}$ ) powder references are shown for comparison. (b) Fourier transform magnitudes of  $k^2$ -weighted Pd K-edge EXAFS spectra, along with the corresponding first shell fit (red lines). Pd–O and Pd–Pd first shell coordination numbers can be extracted from the best fit of the EXAFS data. (c) The unit cells of face-centered cubic metallic Pd and tetragonal Pd oxide (PdO) as determined by X-ray crystallography. The scattering paths (Pd–Pd and Pd–O) used in EXAFS fitting are indicated by the green arrows.

The EXAFS fitting result shows that for both of the terminations, the Pd–Pd coordination number ( $N_{\text{Pd-Pd}}$ ) increases and the Pd–O coordination number ( $N_{\text{Pd-O}}$ ) decreases as the number of ALD cycles increased. The  $\sigma$ , or the Debye-Waller factor (DWF), in the Pd nanoparticles is higher than the bulk value ( $\sigma = 0.074 \text{ \AA}$  based on the Debye temperature of Pd,  $\theta_{\text{D, Pd}} = 274 \text{ K}$ ). In general, the DWF increases as the size of the nanoparticle decreases because there is more

surface, and at a surface the local DWF is always larger. However, the trend of DWF decreasing is not observable because of the relatively large uncertainties.

The atomic fraction of Pd in the Pd<sup>0</sup> and Pd<sup>2+</sup> chemical states, namely  $f_{Pd^0}$  and  $f_{Pd^{2+}} = 1 - f_{Pd^0}$ , is calculated from both the linear combination fitting of XANES and the first shell coordination numbers ( $N$ ) of Pd–Pd and Pd–O bonding fitted from the EXAFS (details in Appendix B.3). As seen in Figure 4.8, the atomic fractions obtained from both XANES and EXAFS agree with each other. The atomic fraction of Pd<sup>0</sup> monotonically increases with the number of ALD cycles, and is greater on the SrO surfaces than on the TiO<sub>2</sub> surfaces.

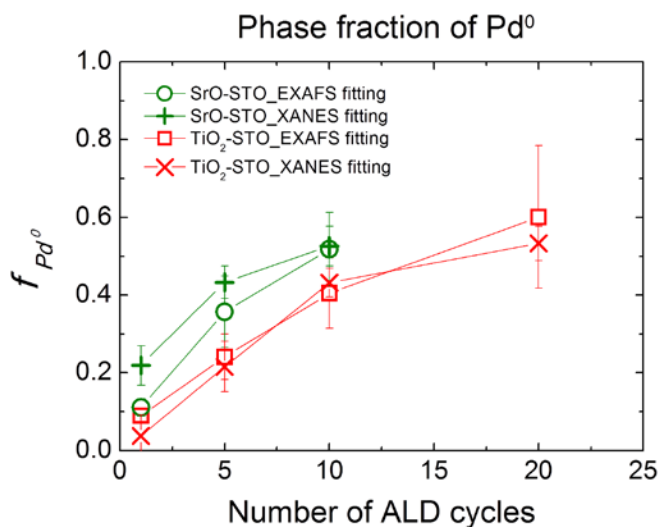


Figure 4.8 Atomic phase fraction of Pd<sup>0</sup> ( $f_{Pd^0}$ ) in Pd nanoparticles with the number of ALD cycles.  $f_{Pd^0}$  increases monotonically as the number of ALD cycles increases; and  $f_{Pd^0}$  is higher on the SrO-STO surface at the same number of ALD cycles.

Table 4.3 Atomic phase fraction of Pd<sup>0</sup> phase determined from both XANES and EXAFS analysis described in Figure 4.8.

Termination	# cycles	Atomic phase fraction of Pd <sup>0</sup>	
		XANES	EXAFS
TiO <sub>2</sub>	<b>1c</b>	0.04 ± 0.05	0.09 ± 0.02
	<b>5c</b>	0.22 ± 0.07	0.24 ± 0.06
	<b>10c</b>	0.43 ± 0.04	0.41 ± 0.09
	<b>20c</b>	0.53 ± 0.04	0.60 ± 0.18
SrO	<b>1c</b>	0.22 ± 0.05	0.11 ± 0.02
	<b>5c</b>	0.43 ± 0.04	0.36 ± 0.09
	<b>10c</b>	0.53 ± 0.04	0.52 ± 0.09

Table 4.4 Fitting parameters of Pd K-edge EXAFS of as-deposited Pd/SrTiO<sub>3</sub> nanocuboids, including the first nearest neighbor coordination numbers ( $N$ ), bond distances ( $R$ ), EXAFS Debye-Waller factors ( $\sigma$ ), and energy shifts ( $\Delta E$ ) for Pd-Pd and Pd-O scattering paths.

		$N_{\text{Pd-Pd}}$	$R_{\text{Pd-Pd}}$ (Å)	$\sigma_{\text{Pd-Pd}}$ (Å)	$\Delta E_{\text{Pd-Pd}}$ (eV)	$N_{\text{Pd-O}}$	$R_{\text{Pd-O}}$ (Å)	$\sigma_{\text{Pd-O}}$ (Å)	$\Delta E_{\text{Pd-O}}$ (eV)
<b>Pd foil</b>		12	2.75	0.074	0				
<b>PdO (II)</b>						4	2.01		0
<b>Termination</b>	<b># cycles</b>								
<b>TiO<sub>2</sub></b>	<b>1c</b>	1.0 ±1.0	2.69 ±0.10	0.11 ±0.02	5.1 ±3.5	3.2 ±0.4	2.01 ±0.01	0.04 ±0.01	2.1 ±1.5
	<b>5c</b>	2.4 ±1.5	2.72 ±0.05	0.11 ±0.02	0.2 ±4.7	3.0 ±0.6	2.01 ±0.02	0.05 ±0.02	2.0 ±2.6
	<b>10c</b>	3.4 ±1.1	2.70 ±0.02	0.10 ±0.02	-3.1 ±2.6	1.7 ±0.5	2.01 ±0.02	0.05 ±0.02	1.5 ±3.8
	<b>20c</b>	4.8 ±0.3	2.72 ±0.02	0.09 ±0.02	-3.6 ±2.8	1.1 ±0.8	2.01 ±0.07	0.06 ±0.01	3.7 ±1.8
<b>SrO</b>	<b>1c</b>	1.2 ±0.9	2.71 ±0.06	0.10 ±0.05	2.7 ±2.6	3.2 ±0.6	2.01 ±0.01	0.06 ±0.02	3.5 ±1.7
	<b>5c</b>	3.0 ±1.1	2.71 ±0.03	0.09 ±0.02	0.1 ±3.1	1.8 ±0.6	2.01 ±0.03	0.06 ±0.02	3.5 ±4.1
	<b>10c</b>	4.2 ±0.8	2.72 ±0.02	0.10 ±0.01	-3.1 ±1.8	1.3 ±0.4	2.01 ±0.02	0.05 ±0.02	1.5 ±3.9

\* The value of  $\Delta E$  can either be a positive or negative number. Therefore, a fitted  $\Delta E$  value like 2.0 ±2.6 will be acceptable. The acceptable range of  $\Delta E$  is in between -10 to 10 eV.

\*\* The value of  $\sigma_{\text{Pd-Pd}}$  of Pd foil (0.074 Å) was calculated from the Debye temperature of Pd,  $\theta_{\text{D, Pd}} = 274$  K.

#### 4.3.4 In-situ EXAFS Measurements of $N_{Pd-Pd}$ under Reduction Conditions

Although TEM is an effective tool for imaging the size of Pd nanoparticles directly, it is difficult to establish statistically significant measurements of the size of Pd nanoparticles when the loading is very low. It has been proposed that the coordination number of the first nearest neighbors ( $N$ ) has a positive correlation with the size of the metallic nanoparticles [120,121]. Thus, EXAFS could serve as a good complementary characterization tool for measuring the size of nanoparticles. The in-situ EXAFS measurements were completed in  $H_2$  flow at room temperature. Under this condition, hydrogen dissolves into interstitial sites in the Pd lattice and forms a Pd hydride, causing a slight expansion in the Pd lattice [122–125]. The expansion can be seen from the  $R_{Pd-Pd}$  values listed in Table 4.5, which are 1 to 2% larger than that of the Pd foil. Despite this lattice expansion, the FCC structure of the Pd sublattice is retained [125]. Therefore  $N$ , which is related to the sublattice structure of Pd, is unchanged by Pd hydride formation. Thus  $N$  can still be applied as a probe reflecting the trend in Pd nanoparticle size evolution.

Figure 4.9 shows that  $N_{Pd-Pd}$  on the  $TiO_2$ -terminated surface increases monotonically as the number of ALD cycles increases; whereas the same quantity on the SrO-terminated surface levels off after 5c. The result implies that the mean size of Pd nanoparticles on the  $TiO_2$ -STO surface continued to increase over the range of 1-20 cycles. For the SrO-STO surface, the Pd nanoparticles grow in size from 1c to 5c, but stop increasing after 5c. This EXAFS result is consistent with the nanoparticle size trend seen by TEM in Figure 4.2. For both surfaces, the Pd nanoparticle grows more significantly during the first ALD cycle than the subsequent cycles. The

phenomena are similar to the result of ALD-Pt on the SrO-terminated nanocuboids reported in Refs. [26,46].

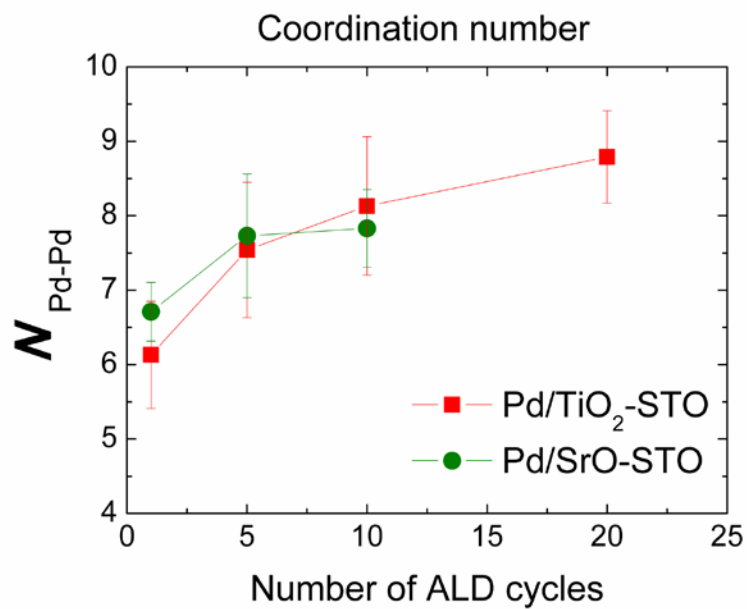


Figure 4.9 First shell coordination number of Pd ( $N_{\text{Pd-Pd}}$ ) extracted from the *in-situ* EXAFS measurement as a function of the number of ALD cycles. The measurements were performed after the residual Pd oxide on the Pd/STO samples was removed under flowing H<sub>2</sub> at 300 °C for 30 min.

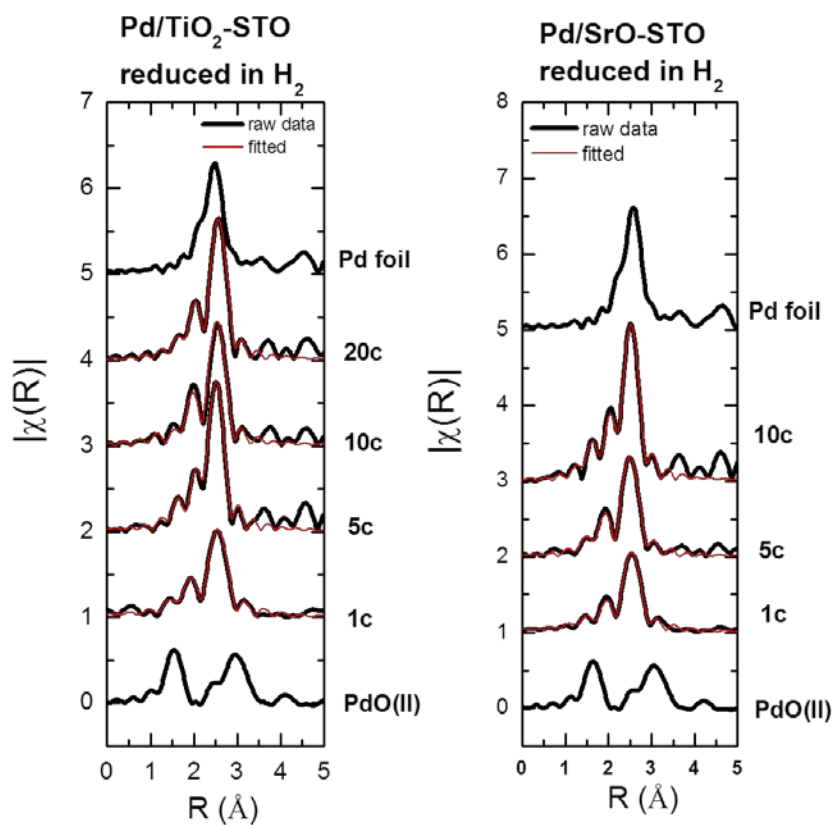


Figure 4.10 Fourier transform magnitudes of  $k^2$ -weighted Pd K-edge EXAFS spectra of the reduced Pd/STO samples, along with the corresponding first shell fit (red lines). Pd–O and Pd–Pd first shell coordination numbers can be extracted from the best fit of the EXAFS data (Table 4.5).

Table 4.5 Fitting parameters of Pd K-edge EXAFS of Pd/SrTiO<sub>3</sub> nanocuboids reduced in H<sub>2</sub> at 300 °C for 30 min. The fitting parameters include the first nearest neighbor coordination numbers (*N*), bond distances (*R*), EXAFS Debye-Waller factors (*σ*), and energy shifts (*ΔE*). Notice that the error bar is large in the Pd–O path because the Pd–O contribution presumably only comes from the interface bonding between Pd and the oxygen in the SrTiO<sub>3</sub> lattice.

		<i>N</i> <sub>Pd-Pd</sub>	<i>R</i> <sub>Pd-Pd</sub> (Å)	<i>σ</i> <sub>Pd-Pd</sub> (Å)	* <i>ΔE</i> <sub>Pd-Pd</sub> (eV)	<i>N</i> <sub>Pd-O</sub>	<i>R</i> <sub>Pd-O</sub> (Å)	<i>σ</i> <sub>Pd-O</sub> (Å)	* <i>ΔE</i> <sub>Pd-O</sub> (eV)
<b>Pd foil</b>		12	2.75	** 0.074	0			0.04	
<b>PdO (II)</b>						4	2.01		
<b>Termination</b>	<b># cycles</b>								
<b>TiO<sub>2</sub></b>	<b>1c</b>	6.2 ±0.3	2.77 ±0.01	0.09 ±0.01	-4.2 ±0.8	0.3 ±0.3	2.85 ±0.11	0.07 ±0.21	4.1 ±8.3
	<b>5c</b>	7.5 ±0.9	2.74 ±0.04	0.08 ±0.01	-0.6 ±0.1	0.5 ±0.5	2.75 ±0.02	0.06 ±0.01	1.6 ±0.0
	<b>10c</b>	8.1 ±0.6	2.78 ±0.01	0.09 ±0.01	-6.2±0.9	0.2 ±0.2	2.73±0.14	0.09 ±0.04	4.5 ±1.2
	<b>20c</b>	8.7 ±0.4	2.81 ±0.01	0.09 ±0.01	-4.4 ±0.3	0.1 ±0.1	2.69 ±0.17	0.06 ±0.02	4.0 ±0.0
<b>SrO</b>	<b>1c</b>	6.7 ±0.4	2.78 ±0.01	0.10 ±0.05	-5.5 ±0.4	0.2 ±0.1	2.66 ±0.05	0.05 ±0.03	-6.4 ±0.0
	<b>5c</b>	7.7 ±0.5	2.73 ±0.01	0.10 ±0.05	-4.3 ±0.5	0.1±0.1	2.67 ±0.43	0.04 ±0.04	-5.8 ±0.0
	<b>10c</b>	7.8 ±0.5	2.74 ±0.01	0.08 ±0.01	0.3 ±0.5	0.6 ±0.2	2.75 ±0.00	0.06 ±0.03	5.9 ±1.5

\* The value of *ΔE* can either be a positive or negative number. Therefore, a fitted *ΔE* value like -0.6±0.1 will be acceptable. The acceptable range of *ΔE* is in between -10 to 10 eV.

\*\* The value of *σ*<sub>Pd-Pd</sub> of Pd foil (0.074 Å) is calculated based on a Debye temperature of Pd, *θ*<sub>D, Pd</sub> = 274 K.

#### 4.3.5 Mechanism of ALD-Pd Nanoparticle Growth on TiO<sub>2</sub>- and SrO-STO Surfaces

Combining the data described in the above paragraphs, a model for the mechanism of ALD-Pd nanoparticle growth on the STO surfaces can be proposed. The growth of Pd on TiO<sub>2</sub>-terminated STO surface is similar to the “nucleation and growth model,” as in the case of Pt on STO nanocuboids reported by Christensen et al. [24] and Wang et al. [26,46]. In this nucleation and growth mechanism, single Pt atoms deposited on the surface are able to move across the surface and merge into the existing nuclei. However, the growth of Pd on the SrO-STO surface cannot be simply explained by the nucleation and growth model only. The residual ligands left on the STO surface from the Pd precursor, Pd(hfac)<sub>2</sub>, have to be taken into account as well. In previous ALD-Pd studies on both Al<sub>2</sub>O<sub>3</sub> and TiO<sub>2</sub> supports, it was shown that Pd(hfac)<sub>2</sub> dissociates into surface (hfac)\* species, which are incompletely removed by subsequent formalin cycles [126–128]. Meanwhile, the surface (hfac)\* species start to decompose creating surface F\* species when the temperature is above 100 °C [128]. For our ALD growth temperature of 200 °C, XPS on both TiO<sub>2</sub>- and SrO-terminated supports (Figure 4.11(a)) show F 1s core level peaks with binding energies at 685 and 689 eV consistent with that of -F and -CF<sub>3</sub> species, respectively as reported in [128–130]. The XPS result indicates the existence of residual (hfac)\* species on both the TiO<sub>2</sub>- and SrO-STO surfaces after ALD Pd growth.

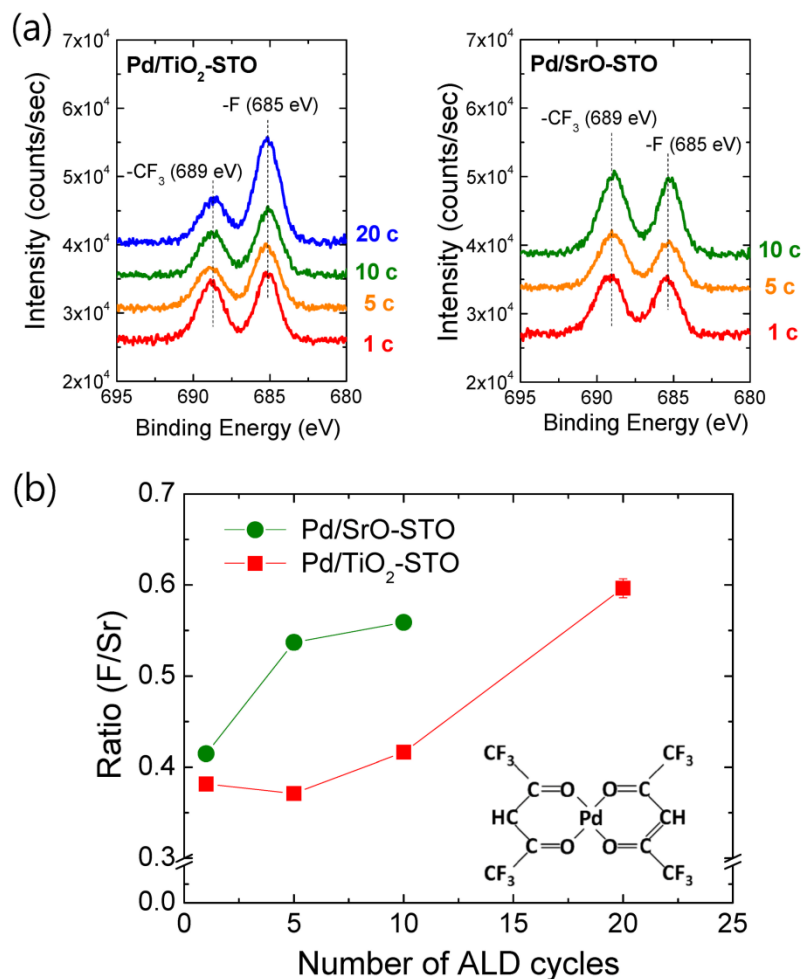


Figure 4.11 (a) X-ray photoelectron spectra of F 1s peaks of the Pd/TiO<sub>2</sub>-STO and Pd/SrO-STO samples. (b) The atomic ratio between F and surface Sr atoms. The inserted image in 7(b) shows the structure of a Pd(hfac)<sub>2</sub> molecule, which has 12 fluorine atoms.

The degree of interaction between the hfac species and the STO surface is likely responsible for the difference in Pd growth pattern. The hfac ligand is acidic and will interact more strongly with the basic SrO-STO surface than the neutral TiO<sub>2</sub>-STO surface [42,70]. In the XPS analysis, the atomic ratios between F and Sr for the Pd/SrO-STO samples are higher than the

Pd/TiO<sub>2</sub>-STO samples (Figure 4.11(b)), indicating a higher coverage of hfac species remaining on the SrO-STO surface (See Appendix B.2 for details in calculation). The strongly bonded hfac species on the SrO surface hinders the migration of deposited Pd atoms across the surface to combine with existing nuclei, and leads to the formation of secondary nuclei in subsequent ALD cycles. Consequently, the Pd nanoparticle density for 10c is higher than that of 5c on the SrO-STO surface, as shown in the TEM images in Figure 4.2. The formation of secondary nuclei also explains the wide size distribution of Pd nanoparticles on the SrO-STO surface. The increase in Pd nanoparticle size is inhibited by the number of hfac species surrounding the Pd nanoparticle. The nanoparticle can grow until the free Pd atoms within the migration distance are entirely consumed. The hfac species are expected to be statistically distributed over the SrO surface; therefore, in regions of a higher hfac concentration, the migration of the Pd atoms is hindered, leading to smaller nanoparticles. Conversely, in areas with a low hfac number density, Pd atoms migrate relatively freely and result in the formation of larger Pd nanoparticles.

Furthermore, from the EXAFS fitting of  $N_{\text{Pd-Pd}}$  shown in Figure 4.9, the trapped Pd single atoms (or clusters) lower the average  $N_{\text{Pd-Pd}}$  in the Pd nanoparticles on the SrO surface. This explains why TEM determined average size of Pd is larger on the SrO surface, but the  $N_{\text{Pd-Pd}}$  value is not reflecting the TEM determined size: the trapped Pd is beyond the resolution of the TEM (< 1 nm). On the other hand, the reason why the Pd on SrO 5c behaves more like Pd<sup>2+</sup> than the SrO 10c can be rationalized as the following: on the surface of 5c, the smaller trapped Pd are easier to oxidize, which makes the 5c appears more oxidized. During the subsequent ALD cycles, secondary Pd nuclei sites start to grow and reduce the percentage of trapped Pd clusters. Therefore, the Pd in the SrO 10c sample appears more reduced than the 5c sample. A schematic

representation of the "nucleation and growth model" and "trapped Pd model" can be found in Figure 4.12.

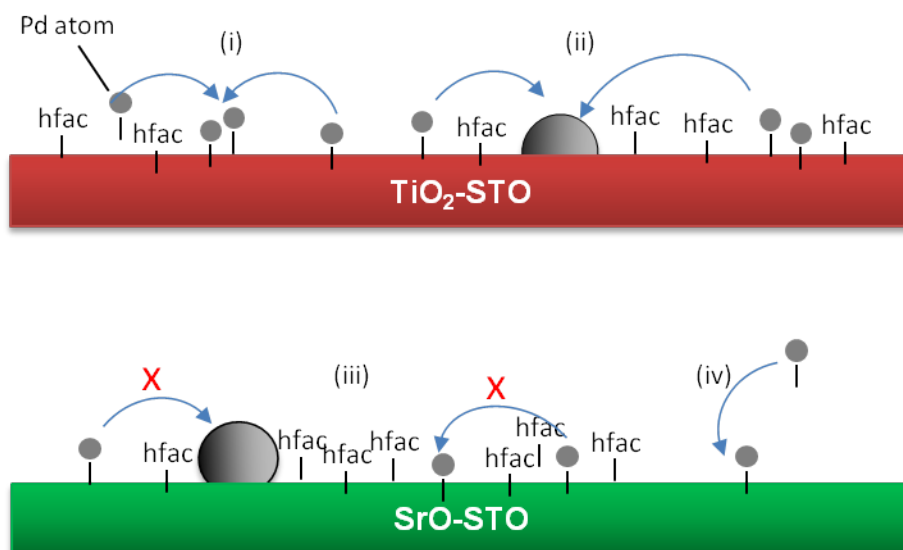


Figure 4.12 Schematic representations of the growth of ALD Pd nanoparticles on the TiO<sub>2</sub>- and SrO-terminated STO surfaces. On the TiO<sub>2</sub>-STO surface, Pd follows the "nucleation and growth model," in which Pd atoms are able to migrate across the surface to form nuclei because the hfac species on the surface weakly bounded (i). The nucleus grows from the migration of the Pd atoms in the subsequent ALD cycles (ii). On the SrO-STO surface, Pd follows the "trapped Pd model," in which the migration of Pd is hindered by the strongly bonded hfac species (iii). In the subsequent ALD cycles, Pd forms secondary nuclei on hfac free area (iv).

#### 4.3.6 In-situ XANES Measurements of Pd/STO under Redox Environment

In order to track the oxidation state change of Pd under environmental conditions similar to a catalytic reaction, *in-situ* XANES was used to measure the oxidation state change of Pd at each step of a redox reaction. Based on Figure 4.5, the effective Pd coverages for the 5c/TiO<sub>2</sub>-STO and 10c/SrO-STO are similar (approximately 0.8 ML). Therefore, the two samples were chosen for comparison of their behavior under redox conditions. The *in-situ* XANES redox measurements (Figure 4.13) show that the oxidation state of Pd on both TiO<sub>2</sub>- and SrO-terminated surfaces can be shifted to either Pd<sup>0</sup> or Pd<sup>2+</sup> state by exposing the Pd/STO sample to H<sub>2</sub> or O<sub>2</sub> gas at 300 °C, and the transition is reversible. This indicates that both of the Pd/STO catalysts have the potential to sustain multiple oxidation/reduction cycles in catalytic reactions.

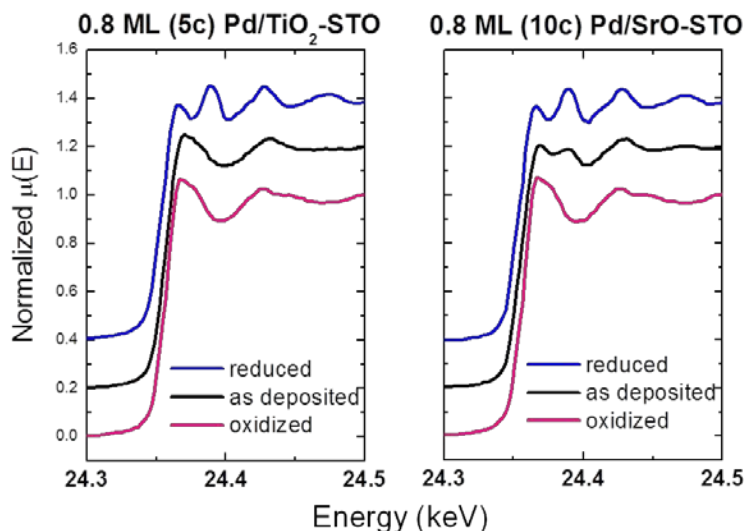


Figure 4.13 Pd K-edge *in-situ* XAFS measurements of 0.8 ML Pd on the TiO<sub>2</sub>- and SrO-terminated STO surfaces. The measurements were performed at 300 °C under H<sub>2</sub>/O<sub>2</sub> redox conditions and were shown to be reversible.

#### 4.4 Summary

The morphological and chemical properties of ALD-grown Pd nanoparticles supported on TiO<sub>2</sub>-STO and SrO-STO nanocuboids with well-defined (001) surface are characterized and compared by the combined analysis of TEM, XRF, XANES, EXAFS, and XPS. The Pd nanoparticle exhibits better wetting on the TiO<sub>2</sub>-STO surface than on the SrO-STO surface, indicating lower interfacial free energy of Pd/TiO<sub>2</sub>-STO than that of Pd/SrO-STO interface. The contrasting wetting property may offer opportunities for controlling the morphology and exposed facets of Pd nanoparticles by different surface terminations of the support oxide. In addition, the number of the ALD cycles is able to control the effective Pd coverage and the fraction of Pd<sup>0</sup>.

The coverage and Pd<sup>0</sup> fraction are found to increase monotonically with the number of ALD cycles on both supports.

As the loading of Pd increases, the Pd nanoparticles grow in number on the SrO-STO surface, but in size on the TiO<sub>2</sub>-STO surface. The difference in the growth behavior is attributed to the interaction between the STO surface and the residual hfac species from the Pd precursor. The strongly-bounded hfac species hinder the migration of Pd atoms on the SrO-STO surface and leave single Pd atoms or sub-critical nuclei trapped. Thus, the Pd nanoparticles grow by forming secondary nuclei on the SrO-STO surface. Compared to Pd on the SrO-STO surface, Pd on the TiO<sub>2</sub>-STO surface is not affected by the relatively weakly-bounded hfac species. Therefore, the Pd nanoparticles follow a nucleation and growth mechanism and grow in size.

The result has demonstrated the feasibility of utilizing the Pd/STO metal/support oxide system to investigate the relationship between the structure of metal catalysts and the performance. We expect that this approach can be further employed for other metal/support oxide systems.

## **Chapter 5: Morphology and CO Oxidation Activity of Pd Nanoparticles**

### **Supported on SrTiO<sub>3</sub> Nanopolyhedra**

#### **5.1 Introduction**

This chapter discusses the relationship between the morphology and catalytic activity of ALD-Pd nanoparticles on TiO<sub>2</sub>-(001)-STO nanocuboids and (110)-STO nanododecahedra. The focus is on building the connection between the shape of supported Pd nanoparticles and CO oxidation activity. As the nanoparticle formation on different supports involves different magnitudes of interfacial and surface energies, the equilibrium shape of the supported nanoparticles changes with different support surfaces according to the Winterbottom construction [39,93]. The equilibrium shape, or the Winterbottom shape, is determined by the minimization of total interfacial and surface energies. The variation of these energy contributions may lead to differences in the truncated height and exposed facets of the supported nanoparticles, and further results in the change of catalytic properties. For free-standing Pt or Pd nanoparticles, the catalytic activity depends upon the exposed crystal facets, as studies have shown that (111) facets of Pt or Pd are significantly more active than (001) facets toward the CO oxidation reaction [47,48]. Therefore, the CO oxidation reaction is established in the present study as an activity probe to distinguish the supported Pd nanoparticles with different area ratios of the exposed (111) to (001) facets.

## 5.2 Materials and Methods

### 5.2.1 Sample Preparation

TiO<sub>2</sub>-(001)-STO nanocuboids and (110)-STO nanododecahedra supports were produced by two separate hydrothermal synthesis methods as reported in Refs. [41,45]. The two types of supports are single crystal nanopolyhedra with atomically-flat facets and negligible edge/corner areas. TiO<sub>2</sub>-(001)-STO nanocuboids have an average edge length of 50-70 nm, while that of (110)-STO nanododecahedra have diameters ranging from 100-1000 nm. The specific surface areas of the two types of supports were measured by a standard Brunauer-Emmett-Teller (BET) analysis. TiO<sub>2</sub>-(001)-STO nanocuboids and (110)-STO nanododecahedra showed BET surface areas of approximately 20 and 4 m<sup>2</sup>/g, respectively.

Pd was deposited on the two types of STO supports by atomic layer deposition (ALD) at 200 °C using Pd(II) hexafluoroacetylacetonate (Pd(hfac)<sub>2</sub>) and formalin (HCHO) as the precursors. The deposition conditions and experimental setup followed our previous ALD work in Ref. [40]. In this thesis project, 1, 5, and 10 ALD cycles of Pd (denoted as 1c, 5c, and 10c) were deposited on both the TiO<sub>2</sub>-(001) and (110) terminated STO nanopolyhedra.

### 5.2.2 Electron Microscopy

The morphological evolution of the Pd/(001)-TiO<sub>2</sub>-STO nanocuboids and Pd/(110)-STO nanododecahedra was measured by a JEOL JEM-2100FasTEM, and by a Hitachi H-2300 STEM equipped with a secondary electron (SE) detector. Both instruments are part of the EPIC facility in the NUANCE Center at Northwestern University (NU). The high-resolution electron microscopy (HREM) images of Pd nanoparticles were collected by the JEOL JEM-2100FasTEM

system at NU and the JEOL JEM-ARM200CF at the Research Resources Center at the University of Illinois, Chicago (UIC). The size distributions of large representative groups of Pd nanoparticles were extracted by using the ImageJ software [117].

### **5.2.3 Small-Angle X-ray Scattering (SAXS)**

Small-angle X-ray scattering (SAXS) measurements were applied as a complementary technique to the TEM measurements. X-ray scattering data were simultaneously collected by the small-angle and medium-angle Rayonix area detectors at the DuPont-Northwestern-Dow (DND) 5ID-D beamline located at the Advanced Photon Source (APS) of Argonne National Laboratory (ANL). Data were collected at an incident photon energy of 16.00 keV at room temperature. The powdered Pd/STO samples were loaded into Kapton capillary tubes of 1.1 mm in diameter (Cole-Parmer). SAXS data were also taken from an empty capillary tube for background subtraction. 5 images were taken for each sample, and the exposure time of each image was 0.1 s. The 2D SAXS patterns were converted to 1D intensity profiles, which were averaged together.

### **5.2.4 Inductively Coupled Plasma Atomic Emission Spectroscopy (ICP-AES) and X-ray fluorescence (XRF)**

The weight percent (wt%) and coverage (atoms/nm<sup>2</sup>) of Pd were obtained by using both inductively coupled plasma atomic emission spectroscopy (ICP-AES, or ICP) and X-ray fluorescence (XRF). The ICP measurements were conducted at the Quantitative Bio-element Imaging Center at Northwestern University. The Pd/STO samples were dissolved in aqua regia at room temperature for 24 h prior to ICP measurements. The XRF measurements were performed at the APS DND 5BM-D beamline. Data were collected at an incident photon energy of 24.4 keV

by two Vortex-ME4 four-element silicon drift detectors (SDD). The atomic ratio between Pd and Sr was obtained from XRF data and converted to wt% Pd by assuming stoichiometric SrTiO<sub>3</sub> nanopolyhedra. The coverage of Pd on the STO support was calculated accordingly from the Pd/Sr atomic ratio and BET surface area of the STO nanopolyhedra. (See Appendix B.1 for details in the measurements and calculation.)

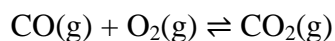
### **5.2.5 X-ray Absorption Near Edge Structure (XANES)**

The chemical states of the supported Pd were determined by measuring the Pd K-edge (24.35 keV) X-ray absorption near edge structure (XANES) measurements. The XANES spectra were measured at the 5BM-D beamline of the APS. The powder Pd/STO samples were uniformly spread onto X-ray transparent tape (3M) and measured in fluorescence mode at room temperature. The XANES data were analyzed using the ATHENA software package [118].

### **5.2.6 Metal Dispersion and CO Oxidation Reaction Measurements**

The metal dispersions of the supported Pd nanoparticles were obtained from both the average Pd nanoparticle size [131] and the CO pulse chemisorption method. (See Appendix B.5 for details.) The CO pulse chemisorption measurements were carried out by using an Altamira AMI-200 catalyst characterization instrument in the Clean Catalysis (CleanCat) Core facility at NU. The Pd/STO catalysts were pre-reduced by 10% H<sub>2</sub>/Ar at 360 °C for 300 min, followed by 25 pulses of 1 - 2.5% CO/Ar injections at room temperature.

To determine the catalytic activity of the Pd/STO samples, the CO oxidation reaction



was employed by using a pre-mixed 0.5% CO/20% O<sub>2</sub>/He reactant gas. The gas-phase reactions were performed using a BenchCAT 4000 reactor system (Altamira Instruments) in the CleanCat Core facility at NU. The system used a 1/4" diameter vertical quartz tube flow reactor. In a typical run, approximately 50 mg of the sample was blended with 300 mg of Al<sub>2</sub>O<sub>3</sub> powder (Sigma-Aldrich). The sample was packed on a quartz wool bed. A CO oxidation catalytic run consisted of varying the reaction gas flow rate from 50 to 200 standard cubic centimeters per minute (sccm), consecutively at 80, 100, and 120 °C. The conversion of CO was measured by using an Agilent 6850 Gas Chromatograph. All reaction runs were repeated at least three times, and the average values of CO conversion were obtained with standard deviations. The performance of the Pd/STO samples was evaluated using the turnover frequency (TOF) of the CO oxidation reaction. TOF was defined as the frequency of CO conversion by surface Pd, in units of s<sup>-1</sup>.

### **5.2.7 Diffuse Reflectance Infrared Fourier Transform Spectroscopy (DRIFTS)**

The DRIFTS measurements were carried out using a Thermal 6700 FTIR model at the CleanCat Core facilities at NU. For a typical experiment, 80 - 100 mg of pure SiO<sub>2</sub> powder (Sigma-Aldrich) was loaded into a Praying Mantis<sup>TM</sup> cell. 20 - 25 mg of the Pd/STO catalyst was packed on top of the SiO<sub>2</sub>. The catalyst was reduced in 150 sccm 10 % H<sub>2</sub>/Ar flow at 300 °C for 30 min, then purged with pure Ar before measurement. The background spectrum was collected at room temperature under constant Ar gas flow. The Pd/STO sample was saturated in 10% CO/Ar gas flow for at least 10 min, followed by an Ar gas purge at 30 - 60 sccms. The DRIFTS

were collected every minute at room temperature in a mixture of 15 sccms of 10% O<sub>2</sub>/Ar with 15 sccms of Ar flow.

## 5.3 Results and Discussions

### 5.3.1 Morphology of ALD-Pd

The Figure 5.1 TEM images show that Pd deposited by the 1 to 10 cycles of ALD form uniformly dispersed NPs, decorating the surfaces of both types of STO nanopolyhedra used in this study. The NPs exhibit approximately equiaxed shapes with narrow size distributions, ranging from 2-3 nm, as shown in Figure 5.2. As the number of ALD cycles increases, Pd on the TiO<sub>2</sub>-(001) surface follows the nucleation and growth model, as previous observed for ALD-Pt [24] and ALD-Pd [40] on the same type of STO surface. In contrast, Pd NPs on the (110)-STO surface from 1c to 5c do not grow significantly in size, but instead grow in number, a trend which suggests secondary nucleation. The number density of Pd from 5c to 10c, however, does not change significantly (see Appendix B.4). Note that for 1, 5, and 10 ALD cycles, the average diameters of Pd NPs on (110)-STO surfaces are larger than on TiO<sub>2</sub>-(001)-STO surfaces.

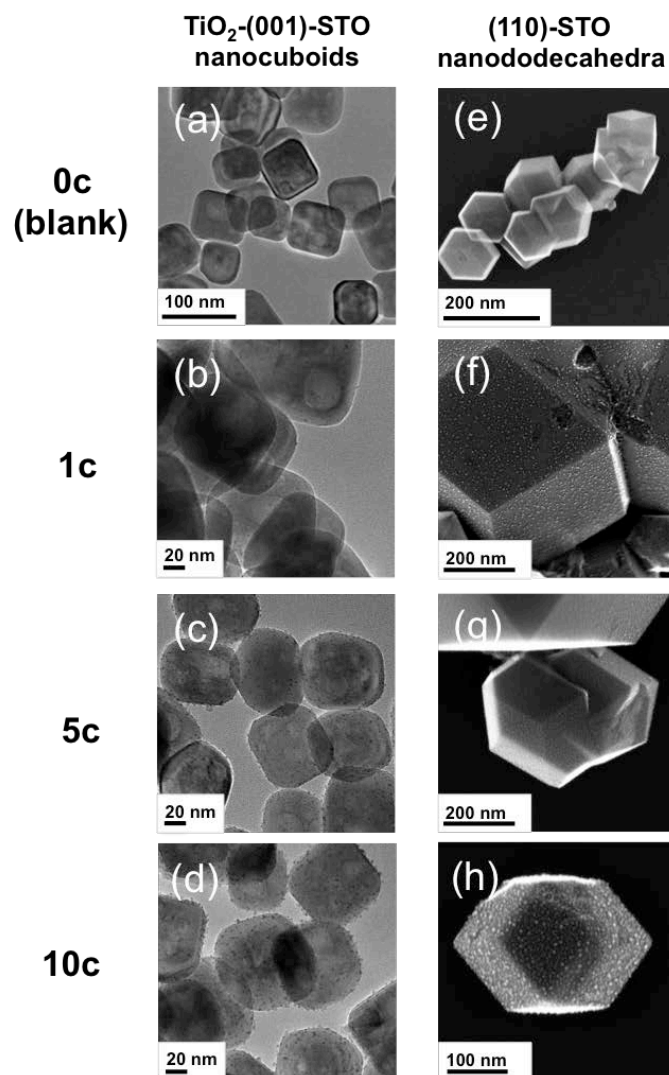


Figure 5.1 TEM images of ALD-Pd deposited on STO nanopolyhedra supports. The left-hand column shows the images of (a) 0c (blank STO), (b) 1c, (c) 5c, and (d) 10c of Pd loaded on the TiO<sub>2</sub>-(001)-STO nanocuboid support. The right-hand column shows (e) 0c, (f) 1c, (g) 5c, and (h) 10c of Pd loaded on the (110)-STO nanododecahedra support. (Figure (e-h) were provided by Lawrence A. Crosby)

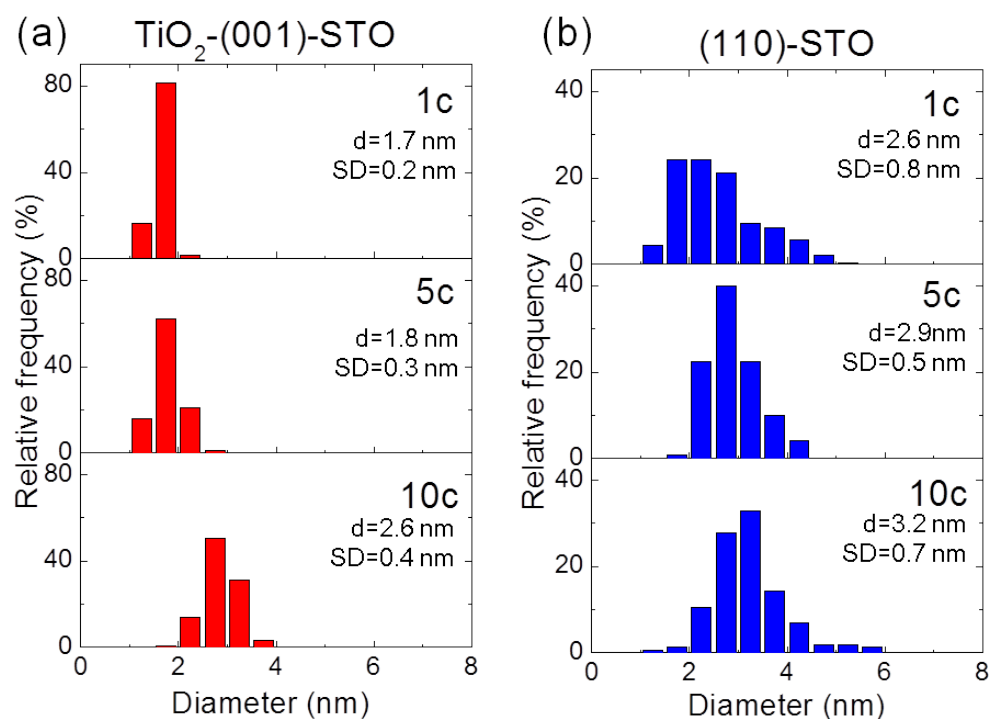


Figure 5.2 Histograms of Pd nanoparticle diameters obtained from multiple representative TEM images: (a) 1c, 5c, and 10c Pd/TiO<sub>2</sub>-(001)-STO nanocuboids, and (b) 1c, 5c, and 10c Pd/(110)-STO nanododecahedra. The mean diameters ( $d$ ) and standard deviations (SD) are included.

To obtain morphological information as a representative global average, SAXS measurements were implemented to complement the local structure resolved from TEM. Figure 5.3 (a) and (b) show the background subtracted SAXS data of Pd on TiO<sub>2</sub>-(001)-STO nanocuboids and (110)-STO nanododecahedra, respectively. For both supports, broad peaks are observed in the range:  $q = 0.1 - 0.3 \text{ \AA}^{-1}$ , which is due to constructive interference between neighboring Pd nanoparticles and is related to the average interparticle spacing ( $D$ ) as  $D =$

$2\pi/q_p$ . The peak position  $q_p$  shifts to lower  $q$  as the number of ALD cycles increases. The fitted position of  $q_p$  and the corresponding  $D$  values are summarized in Table 5.1 (see Appendix B.4 for fitting details).

The SAXS result shows that average NP separation distance  $D$  is generally larger on the (110)-STO surface than that on the TiO<sub>2</sub>-(001)-STO surface. From 5c to 10c,  $D$  increases from 2.9 to 3.7 nm on TiO<sub>2</sub>-(001)-STO surface, while  $D$  only slightly increases from 4.4 to 4.9 nm on (110)-STO nanododecahedra. The larger fractional increase in  $D$  for the TiO<sub>2</sub>-(001)-STO surface implies coalescence between Pd nanoparticles, consistent with the TEM observed nucleation and growth process. A similar coalescence trend was reported in Ref. [24] for ALD-Pt on the same type of TiO<sub>2</sub>-(001)-STO nanocuboids. For Pd on the (110)-STO surface, the slight increase in  $D$  is consistent with the insignificant variation of the number density of Pd.

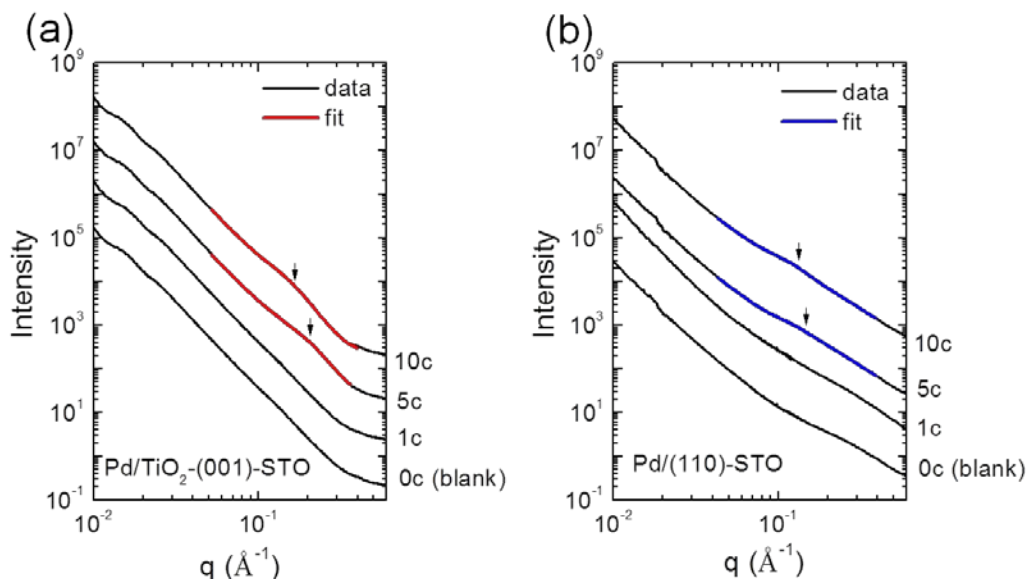


Figure 5.3 Background subtracted SAXS data of (a) Pd/TiO<sub>2</sub>-(001)STO and (b) Pd/(110)-STO samples (offset for clarity). The interference between neighboring Pd nanoparticles leads to a broad peak in the range of  $q = 0.1 - 0.3 \text{ \AA}^{-1}$ . The position of the interference peak ( $q_p$ ) is obtained by fitting the peak with a Gaussian function on a power-law background (see Appendix B.4 for details in fitting).  $q_p$  shifts to lower  $q$  region as the number of ALD cycles increases, as indicated by the arrows.

Table 5.1 Fitted interparticle spacing ( $D$ ) from the SAXS results in Figure 5.3.

	TiO <sub>2</sub> -(001)-STO		(110)-STO	
	$q_{\text{peak}} (\text{\AA}^{-1})$	$D$ (nm)	$q_{\text{peak}} (\text{\AA}^{-1})$	$D$ (nm)
<b>1c</b> <sup>a</sup>	-	-	-	-
<b>5c</b>	0.22(1)	2.9(2)	0.15(1)	4.5(3)
<b>10c</b>	0.16(1)	3.7(2)	0.13(1)	4.9(4)

<sup>a</sup> Meaningful fitting results were unable to be obtained from the 1c samples due to the weak intensity of the interference peak.

Figure 5.4 shows atomic resolution images of individual Pd nanoparticles supported on the surfaces of  $\text{TiO}_2$ -(001)-STO nanocuboids and (110)-STO nanododecahedra. Figure 5.4 (a-d) shows outlines of the faceted shapes of single crystal Pd nanoparticles on both types of STO surfaces. Although Winterbottom construction provides insight into expected morphology of supported Pd nanoparticles, a statistically significant number of images are not yet obtained to confirm whether the experimental Pd shapes are consistent with the predicted Winterbottom shapes. While the Pd nanoparticles shown in (a-d) appear to be single crystals, Figure 5.4 (e) and (f) clearly indicate that twinning occurs in some Pd nanoparticles on both surfaces. The proportion of Pd nanoparticles containing twins is not yet clear. More high resolution electron microscopy studies are necessary to confirm the Winterbottom shape, twinning, and in-plane epitaxial relationship between the Pd and STO.

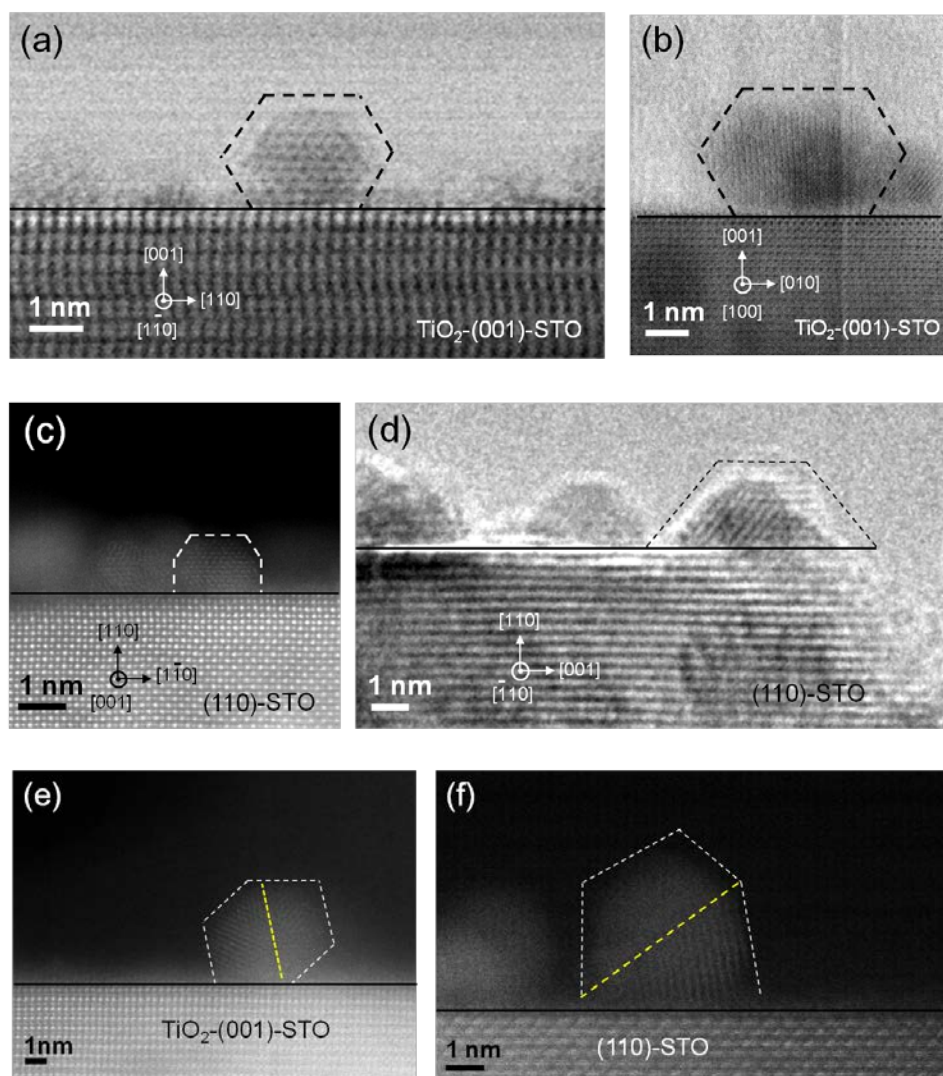


Figure 5.4 Atomic resolution annular bright field (ABF) (a, b), TEM (d), and high angle annular dark field (HAADF) (c, e, and f) images of Pd supported on (a) (b) TiO<sub>2</sub>-(001)-STO and (c) (d) (110)-STO surfaces. The Pd nanoparticles are single-crystalline, as the arrangement of Pd atoms can be clearly seen in the images. (e) (f) HAADF images show twinned Pd nanoparticles on TiO<sub>2</sub>-(001)-STO and (110)-STO surfaces, respectively. The dashed line in yellow represents the twin plane. (Images provided by Lawrence A. Crosby)

### 5.3.2 Loading and Coverage of Pd

The weight percent (wt%) loading of Pd was obtained by using both ICP and XRF, as shown in Figure 5.5(a). However, as the two types of STO nanopolyhedra supports have different surface-to-volume ratios, the Pd loading on each support cannot be compared directly by using wt%. Instead, we use “coverage,” defined as the density of Pd atoms per unit surface area of the nanopolyhedra ( $\text{atom}/\text{nm}^2$ ) to exclude the volume effect. Figure 5.5(b) displays the calculated Pd coverage on the two types of surfaces. Compared to  $\text{TiO}_2$ -(001)-STO surface, the growth rate of Pd on (110)-STO surface is approximately 3 times higher.

Pd shows significant mass gain during the initial ALD cycles on both types of supports. The loading increases by approximately 5 times from 1c to 5c, while the mass gain is less significant from 5c to 10c. Furthermore, the mass gain of Pd for the first cycle is the same as the average gain of cycles 2 through 5 (0.20 wt% and 0.16 wt% per cycle on  $\text{TiO}_2$ -(001)-STO nanocuboids and (110)-STO nanododecahedra, respectively), implying a linear growth from 0c to 5c Pd on both types of STO nanopolyhedra. The linear mass gain of Pd for the initial ALD cycles is analogous to the earlier study of Pt-ALD on  $\text{TiO}_2$ -(001)-STO nanocuboids [24]. Nevertheless, the mass gain per ALD cycle of Pt is ~20 times higher on  $\text{TiO}_2$ -(001)-STO nanocuboids (corresponding to ~10 times higher in coverage per cycle compared to that of Pd). It should be noted that the linear growth model of ALD-Pd observed here deviates slightly from Refs. [10] and [46], where the growth rate of ALD-Pt is higher for the first cycle than the subsequent cycles.

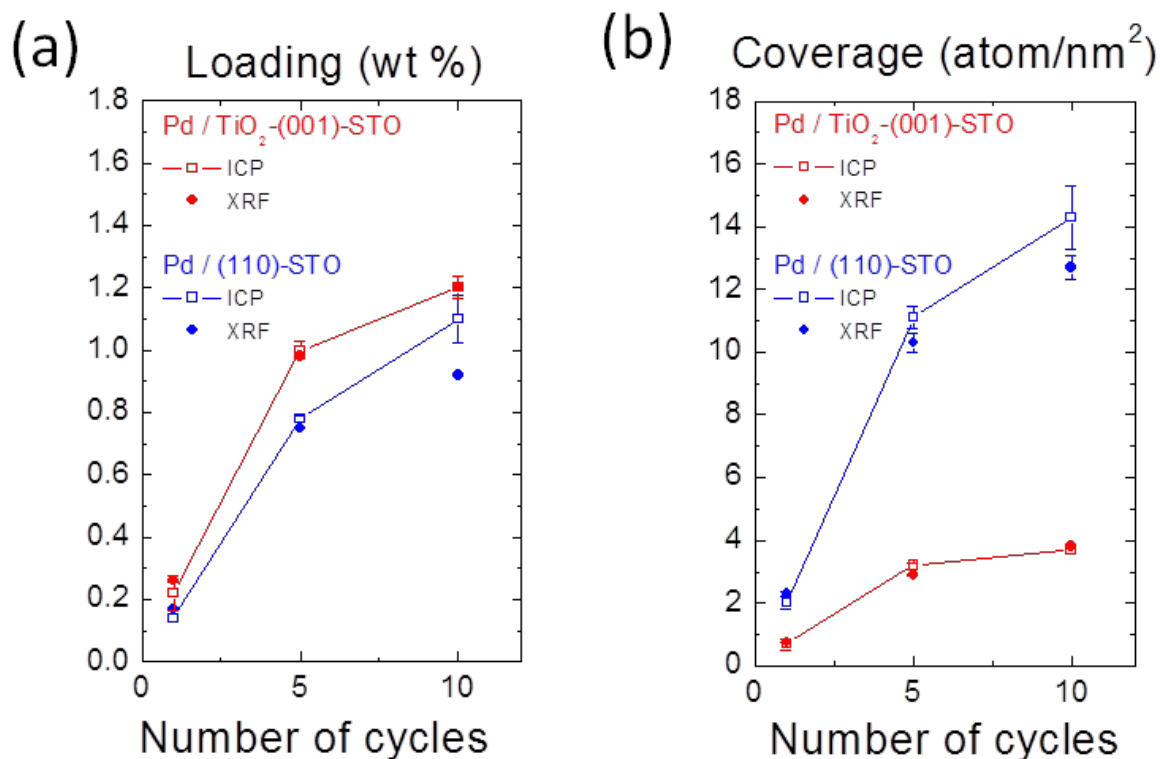


Figure 5.5 Wt% loading of Pd and (b) Pd surface coverage as a function of the number of ALD cycles calculated from both XRF and ICP measurements. The red line and the blue line represent Pd/TiO<sub>2</sub>-(001)-STO, and Pd/(110)-STO, respectively. The coverage is defined as the surface density of Pd atoms and assumes all Pd are on the STO support surface. The numerical data of wt% and coverage are presented in Table 5.2.

Table 5.2 Atomic ratio of Pd to Sr, Pd loading (wt%), and Pd coverage.

		Pd/Sr atomic ratio		Pd loading (wt%)		Pd coverage (atom/nm <sup>2</sup> ) <sup>c</sup>	
		XRF	ICP <sup>a</sup>	XRF <sup>b</sup>	ICP	XRF	ICP
Termination	cycles						
<b>TiO<sub>2</sub>-(001)-STO</b>	<b>1c</b>	0.0045	0.004(1)	0.26	0.22(6)	0.8(1)	0.7(2)
	<b>5c</b>	0.017	0.019(1)	0.99	1.00(3)	2.9(1)	3.2(1)
	<b>10c</b>	0.019	0.022(1)	1.20	1.20(4)	3.2(1)	3.7(1)
<b>(110)-STO</b>	<b>1c</b>	0.0029	0.0025(2)	0.17	0.14(2)	2.3(1)	2.0(2)
	<b>5c</b>	0.013	0.014(1)	0.75	0.78(1)	10.3(3)	11.1(4)
	<b>10c</b>	0.016	0.017(1)	0.92	1.10(7)	12.7(4)	14(1)

<sup>a</sup> Calculated from ICP obtained wt% Pd and wt% Sr.

<sup>b</sup> Calculated from Pd/Sr atomic ratio assuming stoichiometric SrTiO<sub>3</sub> nanocuboids. The error of XRF is small (< 1%) because of good statistics in the counts.

<sup>c</sup> Calculated from Pd/Sr atomic ratio and BET surface areas of the two types of STO nanopolyhedra supports.

### 5.3.3 XANES Determination of the Pd<sup>0</sup> Atomic Fraction

Figure 5.6(a) and (b) show Pd K-edge XANES of Pd nanoparticles supported on TiO<sub>2</sub>-(001)-STO nanocuboids and (110)-STO nanododecahedra, respectively. On the two types of STO surfaces, metallic (Pd<sup>0</sup>) and oxide (Pd<sup>2+</sup>) phases of Pd co-exist. The oxidation state of Pd shifts gradually from Pd<sup>2+</sup> to Pd<sup>0</sup> with increased Pd loading. Figure 5.6(c) shows the atomic fraction ( $f$ ) of Pd in the Pd<sup>0</sup> chemical state, which was calculated from the linear combination fitting of the Pd foil and PdO(II) reference spectra under the assumption that  $f_{Pd^0} + f_{Pd^{2+}} = 1$ . The result shows that  $f_{Pd^0}$  increases monotonically with the number of ALD cycles for both supports, and is higher on (110)-STO than that on TiO<sub>2</sub>-(001)-STO for the same number of ALD cycles.

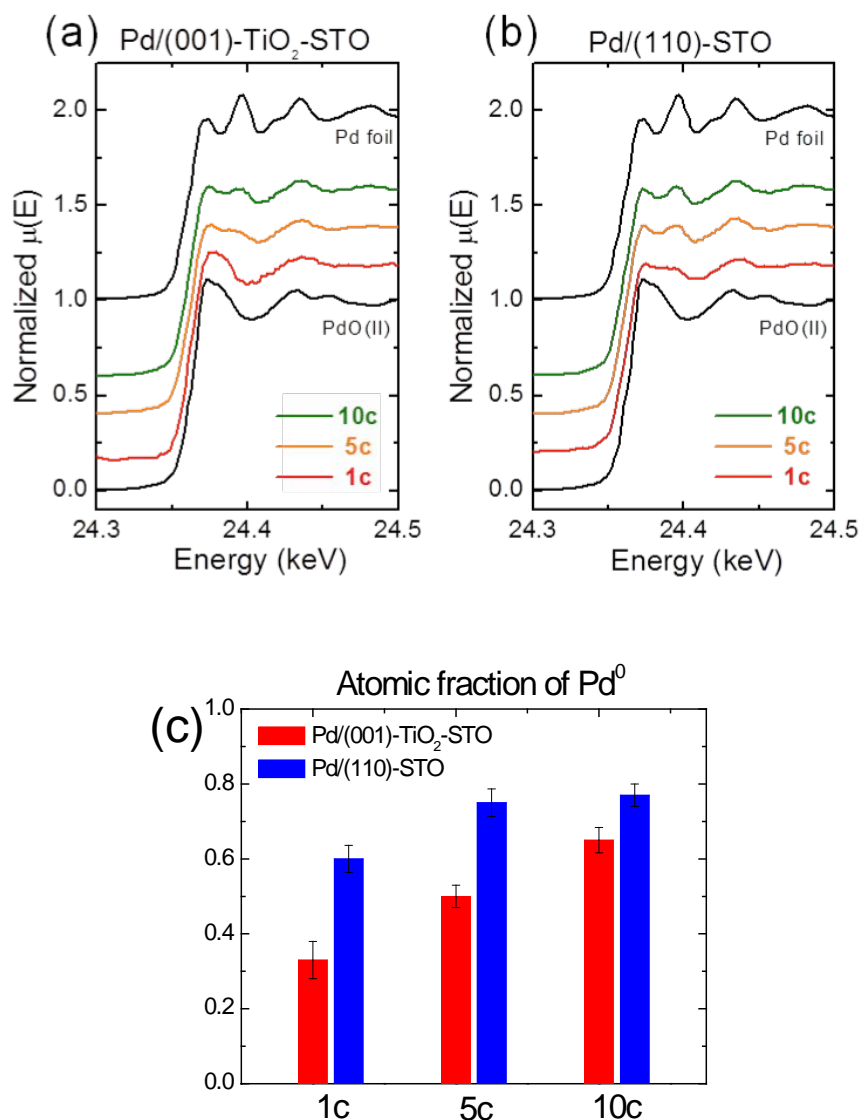


Figure 5.6 Pd K-edge XANES of (a) Pd/TiO<sub>2</sub>-(001)-STO nanocuboids and (b) Pd/(110)-STO nanododecahedra. The Pd foil (Pd<sup>0</sup>) and PdO(II) (Pd<sup>2+</sup>) spectra are shown as references. Comparing the data to the references reveals that the chemical state of supported Pd NPs gradually shifts from Pd<sup>2+</sup> to Pd<sup>0</sup> as the loading increases. (c) The atomic fraction of metallic Pd ( $f_{Pd^0}$ ) obtained from linear combination fitting.  $f_{Pd^0}$  is higher on (110)-STO than on TiO<sub>2</sub>-(001)-STO surface at the same number of ALD cycles.

### 5.3.4 CO Oxidation Activity

Figure 5.7 and Table 5.3 show the turnover frequency (TOF) of the CO oxidation reaction over 1, 5, and 10c Pd on the two types of STO nanopolyhedra. No major difference was observed in the TOF for 5 and 10c Pd on  $\text{TiO}_2$ -(001)-STO nanocuboids and (110)-STO nanododecahedra. However, 1c Pd/ $\text{TiO}_2$ -(001)-STO displays a 2 - 3 times higher TOF at 80 and 100 °C.

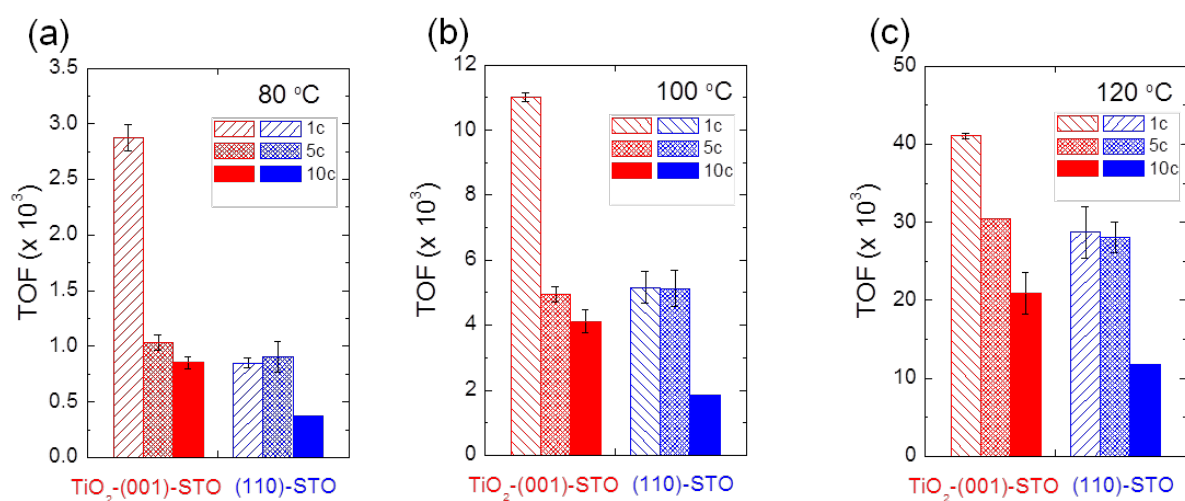


Figure 5.7 The turnover frequency (TOF) of the CO oxidation reaction at 80, 100, and 120 °C. The 1c Pd / $\text{TiO}_2$ -(001)-STO sample is more active than the others at 80 and 100 °C, as seen from the higher TOF.

Table 5.3 The CO oxidation turnover frequency (TOF) at 80 - 120 °C for the Pd/STO catalysts. TOF was calculated from ICP obtained wt% and TEM estimated metal dispersion (see Appendix B.6 for details).

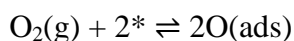
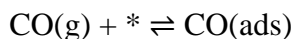
		<b>Diameter</b>	<b>Dispersion</b>	<b>TOF 80 °C</b>	<b>TOF 100 °C</b>	<b>TOF 120 °C</b>
		<b>(nm)<sup>a</sup></b>	<b>(%)<sup>b</sup></b>	<b>(s<sup>-1</sup>)</b>	<b>(s<sup>-1</sup>)</b>	<b>(s<sup>-1</sup>)</b>
<b>Support</b>	<b># cycles</b>					
<b>TiO<sub>2</sub>-(001)-STO</b>	<b>1c</b>	1.7	73.8	2.9(1)×10 <sup>-3</sup>	1.1(1)×10 <sup>-2</sup>	4.1(4)×10 <sup>-2</sup>
	<b>nanocuboids</b>					
	<b>5c</b>	1.8	69.7	1.0(1)×10 <sup>-3</sup>	4.9(2)×10 <sup>-3</sup>	3.0×10 <sup>-2</sup>
	<b>10c</b>	2.6	48.2	8.5(5)×10 <sup>-4</sup>	4.1(3)×10 <sup>-3</sup>	2.1(3)×10 <sup>-2</sup>
<b>(110)-STO</b>	<b>1c</b>	2.6	48.2	8.5(4)×10 <sup>-4</sup>	5.2(5)×10 <sup>-3</sup>	2.9(3)×10 <sup>-2</sup>
	<b>nanododecahdera</b>					
	<b>5c</b>	2.9	43.2	9(1)×10 <sup>-4</sup>	5.1(6)×10 <sup>-3</sup>	2.8(2)×10 <sup>-2</sup>
	<b>10c</b>	3.2	39.2	3.8×10 <sup>-4</sup>	1.9×10 <sup>-3</sup>	1.2×10 <sup>-2</sup>

<sup>a</sup> Average diameter of Pd obtained from multiple TEM images

<sup>b</sup> Dispersion estimated from the average diameter of Pd

The elevated TOF of 1c Pd/TiO<sub>2</sub>-(001)-STO was further studied by using DRIFTS measurements of the CO adsorption intensity on Pd under O<sub>2</sub> exposure. We examined 1c Pd/TiO<sub>2</sub>-(001)-STO, 10c Pd/TiO<sub>2</sub>-(001)-STO, and 1c Pd/(110)-STO samples, with average Pd sizes of 1.7, 2.6 and 2.6 nm, respectively. Figure 5.8(a-c) are the results of the DRIFTS measurements, showing two groups of CO absorption bands: the linear absorption band (~2000-2100 cm<sup>-1</sup>, denoted as L sites) and the bridge-multiple absorption band (~1800-2000 cm<sup>-1</sup>, denoted as B-M sites) [132–134]. The broad width of the L and B-M bands indicates the presence of multiple CO absorption species on the Pd surface [132]. Additionally, the adsorption feature around 1970 cm<sup>-1</sup> (assigned to the bridge-bonded CO on terrace facets of Pd [132,134]) of 10c Pd/TiO<sub>2</sub>-(001)-STO (Figure 5.8(b)) and 1c Pd/(110)-STO (Figure 5.8(c)) disappears after the CO intensity starts to decrease abruptly. This implies that the bridge-bonded CO on terrace sites is more active than the other sites for CO oxidation.

Note that CO absorption intensities of both 10c/TiO<sub>2</sub>-(001)-STO and 1c/(110)-STO abruptly decrease in the presence of O<sub>2</sub>, while the intensity decay is smoother for 1c/TiO<sub>2</sub>-(001)-STO. This is clearly observed in the normalized peak areas under the CO absorption bands (Figure 5.8(d-e)). The abrupt decrease in intensity occurs for relatively larger Pd NPs (2.6 nm) but not for smaller Pd NPs (1.7 nm). This difference is attributed to CO poisoning on the larger Pd nanoparticles. It is well-established that the CO oxidation reaction over Pd surfaces follows the Langmuir-Hinshelwood reaction mechanism [98–101]. In this mechanism, the adsorption of CO and O<sub>2</sub> molecules involves the following elementary steps (\* denotes a free adsorption site):



It is known that O<sub>2</sub> on Pd surfaces possesses a lower sticking coefficient than CO, and the coefficient drops as CO coverage increases [135–137]. Due to CO poisoning, the initial CO<sub>2</sub> production rate is slow because O<sub>2</sub> adsorption is inhibited. The influence of the unequal adsorption strengths was previously demonstrated by studies which exposed O<sub>2</sub> on Pd single crystal surfaces [135] and nanoparticles [101,136], both pre-covered with CO.

The CO poisoning effect described above may occur in our Pd/STO samples with larger Pd, where there are more facet sites than corner/edge sites. Initially, the dissociative adsorption of O<sub>2</sub> is inhibited by CO poisoned Pd facets. Then, successful adsorption of O<sub>2</sub> on some unoccupied adsorption sites allows CO in the vicinity of the adsorbed O<sub>2</sub> to be consumed. This creates additional adsorption sites for O<sub>2</sub> molecules. Because the presence of the active O<sub>2</sub> species accelerates the CO<sub>2</sub> production rate when the surface coverage of CO is high, the intensity of CO adsorption bands in DRIFTS drops dramatically due to fast CO consumption. This phenomenon was also observed in many empty adsorption site (or vacancy) mediated surface auto-catalytic reaction processes [98,138,139].

1c Pd/TiO<sub>2</sub>-(001)-STO, however, has smaller Pd (~ 2 nm), on which the CO poisoning is less prominent due to the larger fraction of the Pd edge/corner sites. These low coordinated sites result in stronger O<sub>2</sub> adsorption/dissociation [137]. As a consequence, O<sub>2</sub> dissociates on Pd and reacts with CO more easily, causing a steady decrease in the CO adsorption intensity. This argument also explains the significantly higher TOF of 1c Pd/TiO<sub>2</sub>-(001)-STO compared to the other samples, because the reaction is not inhibited by CO poisoning. At 120 °C, the TOF of 1c Pd/TiO<sub>2</sub>-(001)-STO and other samples are more comparable due to the weakened adsorption strength of CO, which decreases the effect of CO poisoning. Additionally, raising the temperature increases the overall rate of the reaction.

Also note that the mutual decrease trend of the CO absorption intensity for the L sites and B-M sites shown in Figure 5.8(d-f) is consistent for all three samples investigated. Figure 5.9 shows the area ratios of B-M to L sites stay constant for individual samples, indicating that the adsorbed CO migrates over the Pd surface and redistributes as CO is removed.

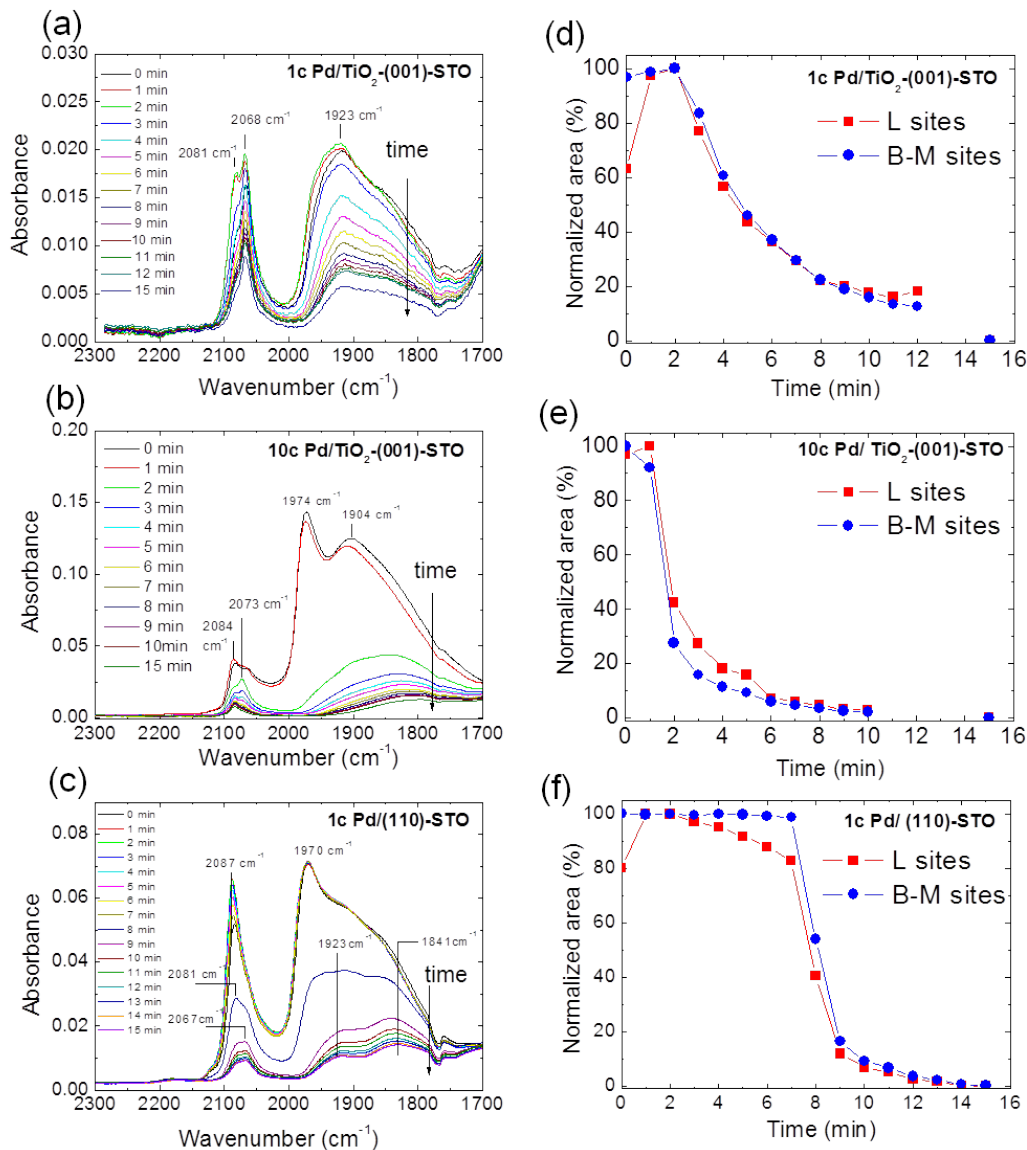


Figure 5.8 DRIFTS showing CO absorption intensity as a function of O<sub>2</sub> exposure time at room temperature for (a) 1c Pd/TiO<sub>2</sub>-(001)-STO nanocuboids, (b) 10c Pd/TiO<sub>2</sub>-(001)-STO nanocuboids, and (c) 1c Pd/(110)-STO nanododecahedra. (d-f) The evolution of normalized CO adsorption peak areas over time. The area denoted as L sites is the linear absorption branch (~2000-2100 cm<sup>-1</sup>) and the bridge-multiple branch (~1800-2000 cm<sup>-1</sup>) is denoted as B-M sites.

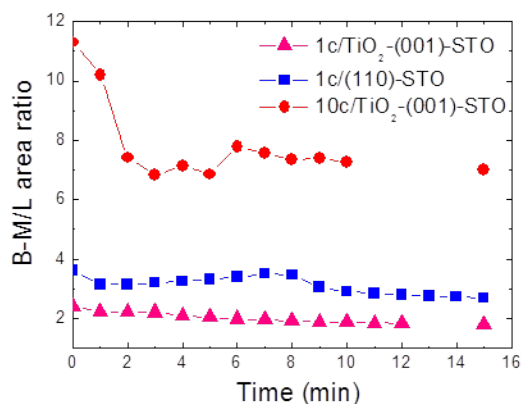


Figure 5.9 Evolution of the B-M to L area ratios with O<sub>2</sub> exposure time. The B-M to L ratios stay constant for the three samples, indicating the redistribution of CO absorption sites as CO is removed.

#### 5.4 Summary

This chapter investigates the morphology and CO oxidation activity of uniformly distributed ALD-Pd nanoparticles supported on single crystal TiO<sub>2</sub>-(001)-STO nanocuboids and (110)-STO nanododecahedra. As the loading increases, Pd on the TiO<sub>2</sub>-(001)-STO surface follows the nucleation and growth model and grows in size, while Pd on the (110)-STO surface begins with secondary nucleation and grows in number. The deposition rate of Pd is higher from 1c to 5c than 5c to 10c on both of the STO surfaces, and is three times higher on the (110)-STO nanododecahedra than on the TiO<sub>2</sub>-(001)-STO nanocuboids. HREM images show that faceted single crystalline and twinned Pd nanoparticles co-exist on the two types of STO surfaces.

However, more images are necessary to confirm the proportion of twinned nanoparticles to single crystalline nanoparticles and the experimental Winterbottom shapes.

Nevertheless, it is the size and not the shape of Pd that most influences the CO oxidation activity. TOF analysis and DRIFTS show that the CO oxidation activity is lower for larger Pd nanoparticles. This is due to CO poisoning on the relatively large facet sites, which inhibits O<sub>2</sub> adsorption. In contrast, the smaller Pd nanoparticles have a higher proportion of edge and corner sites, allowing dissociative adsorption of O<sub>2</sub> on these sites and leading to higher CO oxidation activity.

This chapter demonstrates the ability of STO nanopolyhedra to bridge the materials gap between surface science and catalytic reaction studies. It also provides an example of how the influence of morphology on catalytic activity can be directly studied.

## Chapter 6: Synthesis and Characterization of the STO Nanopolyhedra

### 6.1 Introduction

This chapter serves as a guide to synthesizing  $\text{TiO}_2$ -(001)-terminated nanocuboids, SrO-terminated-(001) nanocuboids and (110)-STO nanododecahedra. Synthesizing various types of STO nanopolyhedra is an ongoing research topic that started before this dissertation and will continue to develop. The previous literature regarding the synthesis method, detailed synthesis procedure, and characterization results of the product will be presented.

In order to apply the STO nanopolyhedra as a catalyst support in various characterization and chemical reaction testing conditions, the synthesis of the STO should be reproducible and should have a reasonable yield. For example, at least 1,000 mg of the Pd/STO nanopolyhedra catalysts are required in order to obtain meaningful characterization and catalytic reaction results. This requirement can be fulfilled by either mass producing in single batch or mixing several batches of STO nanopolyhedra with similar quality.

However, mass production of the SrO-terminated nanocuboids is particularly challenging compared to the other two types of nanopolyhedra due to the low yield. Additionally, removing the long-chain oleic acid surfactant from the surface of STO is difficult. Therefore, several alternative methods to synthesize SrO-terminated STO with a more reproducible yield are under development, and the preliminary results are reported in Section 6.4.

## 6.2 Acetic Acid-Assisted Synthesis of TiO<sub>2</sub>-(001)-STO Nanocuboids

### 6.2.1 Background and Synthesis

The synthesis of TiO<sub>2</sub>-(001)-STO nanocuboids follows the sol-precipitation synthesis developed by Rabuffetti et al. [41]. The details of the synthesis are as follows:

Solution A was prepared by dissolving 2.43 g of Sr(OH)<sub>2</sub>·8H<sub>2</sub>O (Alfa-Aesar, 99%) into 50 mL 1.1M acetic acid (3.15 mL acetic acid in 50 mL solution). Solution B was prepared by mixing 1 mL TiCl<sub>4</sub> (Acros, 99.9%) with 20 mL 200 proof ethanol alcohol. After that, solution B was added slowly into A under a moderate stirring rate for at least 10 min, resulting in a clear transparent liquid with pH ≈ 1. Then, 5g NaOH pellets (Fisher) were added to the transparent solution. While the NaOH pellets were dissolving, the viscosity of the solution increased until a white opaque gel with pH ≈ 14 was formed. The suspension was then stirred for at least 10 min until the high viscosity gel totally disappeared, resulting in a white opaque suspension. The suspension was in the form of a white colloidal solution, which was then loaded into a 125 mL Teflon-lined autoclave (Parr, model 4748) and heated with a ramping rate of 0.5 °C/min to 240 °C for 48 h. The autoclave was subsequently allowed to cool to room temperature. The white sediment at the bottom of the autoclave was filtered and washed thoroughly with deionized water and was then dried at 80 °C for 12 h in the air.

### 6.2.2 Characterization and Discussion

Figure 6.1 shows the TiO<sub>2</sub>-terminated nanocuboids. The mean edge length for the TiO<sub>2</sub>-terminated nanocuboids is 67 nm, with a standard deviation (SD) of 12.5 nm. The Standard Brunauer-Emmett-Teller (BET) analysis determined surface area is 20 m<sup>2</sup>/g.

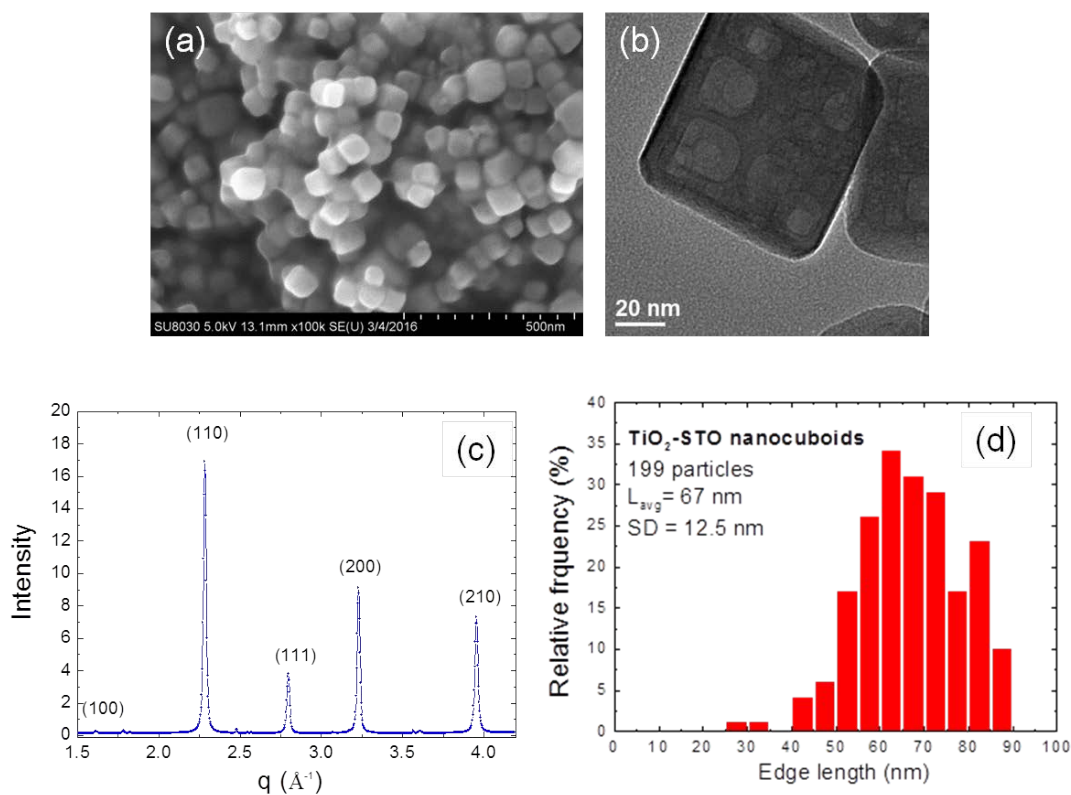


Figure 6.1 (a) Low resolution SEM image, (b) TEM image, (c) wide angle X-ray scattering (WAXS) pattern, and (d) statistics of the  $\text{TiO}_2$ -(001)-STO nanocuboids. The WAXS were collected at the 5ID-D beamline at the APS with an incident X-ray energy of 16.0 keV.

Figure 6.1(b) shows that square-like features are present within the STO nanocuboids. These features exhibit lower contrast and similar alignment with the nanocuboid. As reported by Rabuffetti et al., thickness mapping by using electron energy loss spectroscopy revealed a depletion of materials across the square-shaped features [41]. The depletion region suggests that the features are voids within the STO nanocuboids. Crosby et al. proposed that these voids were Kirkendall voids created by the interdiffusion of the Sr precursor into an amorphous Ti complex

during the hydrothermal synthesis [140]. To investigate the formation of the Kirkendall voids, the white suspension formed during the hydrothermal synthesis after the addition of NaOH was studied by using TEM. As shown in Figure 6.2(a), the nanoparticles are round, with a diameter of 50 - 60 nm, which is almost equal to the edge length of the nanocuboids. The surfaces of the round nanoparticles are rougher than the nanocuboids. No Kirkendall voids are present in the round nanoparticles (Figure 6.2(b)). After a 240 °C, 48 h thermal treatment, nanocuboids with Kirkendall voids were formed, as shown in Figure 6.2(c). This result suggests that the Kirkendall voids might start to form during the thermal treatment in the hydrothermal synthesis. More evidence is required to further elucidate the development of the Kirkendall voids.

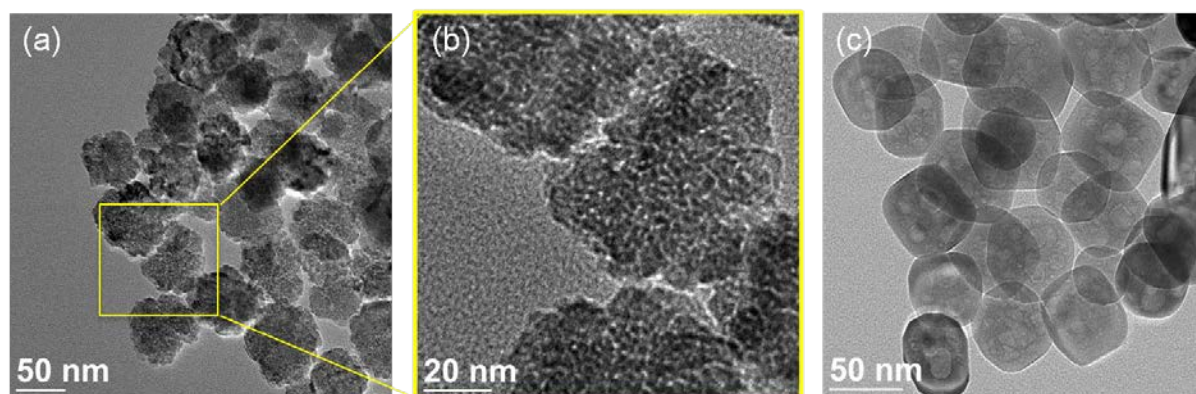


Figure 6.2 TEM images showing the STO nanoparticles before and after the thermal treatment. (a) Round nanoparticles formed after NaOH addition. (b) Close-up of the yellow frame in (a), showing that there are no Kirkendall voids in the particles. (c) STO nanocuboids and Kirkendall voids formed after a 240 °C, 48 h thermal treatment.

## 6.3 Oleic Acid-Assisted Synthesis of SrO-(001)-STO Nanocuboids

### 6.3.1 Background and Synthesis

The synthesis of SrO-(001)-STO nanocuboids follows the works [43,44] published by Hu et al. The STO nanocuboids grow between lamellar microemulsion structures formed by oleic acid molecules; thus, the kinetic-Wulff shape is defined by the lamellar structure [43]. Details of the synthesis are reported as follows:

Solution A was prepared by dissolving 0.22 g Sr(Ac)<sub>2</sub> (Alfa Aesar) into 15 mL deionized water, and was then added with 0.33 g of Ti(OBu)<sub>4</sub> (Alfa Aesar, 99%). Solution B was prepared by mixing 5 mL oleic acid (TCI America, 97%) with 25 mL 200 proof ethanol alcohol. Solution C was prepared by mixing 0.4 g sodium oleate (TCI America) with 20 mL of ethanol, then heated until the sodium oleate dissolved. Solutions A and C were added to B successively while continuously stirring. Then, 2.5 mL of NaOH solution (8 g NaOH in 20 mL water) was added and the mixture was stirred for 5 min. The suspension was loaded into a 125 mL Teflon-lined autoclave (Parr, model 4748) and heated with a ramping rate of 2 °C/min to 160 °C and was held for 10 h. The autoclave was cooled at room temperature, and the white sedimentation was washed thoroughly with deionized water and dried in the air.

### 6.3.2 Characterization

The standard Brunauer-Emmett-Teller (BET) analysis determined surface area of the SrO-terminated nanocuboids is 61 m<sup>2</sup>/g. The mean edge length for the SrO-terminated nanocuboids is 15 nm with 2.8 nm SD, as shown in Figure 6.3.

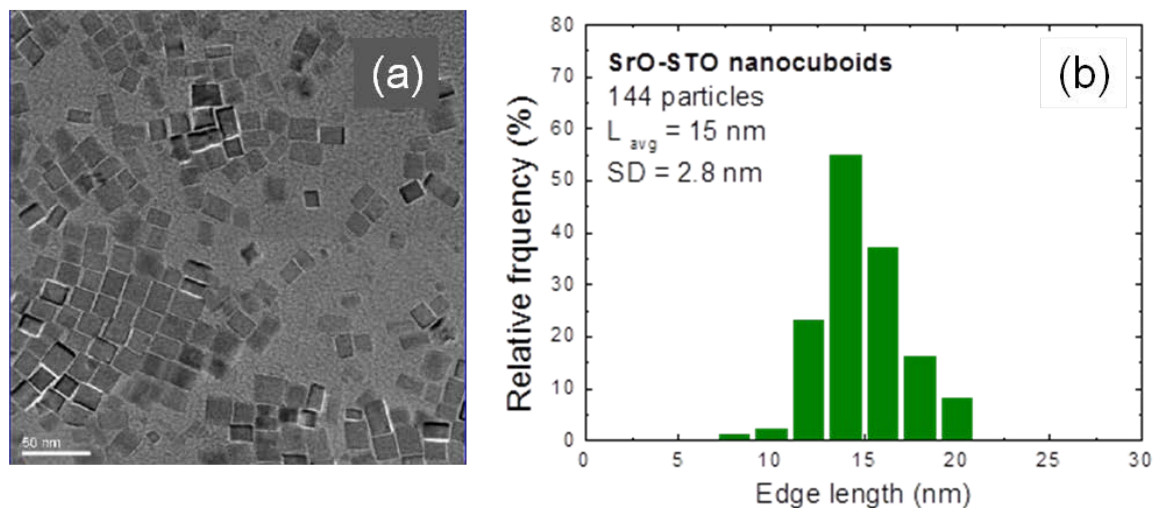


Figure 6.3 (a) TEM image of SrO-(001)-STO nanocuboids. (Adapted from Ref. [44]) (b) Statistics of the edge length of SrO-(001)-STO nanocuboids from (a).

## 6.4 Alternative Methods for Synthesizing Surfactant-Free SrO-(001)-STO Nanocuboids

### 6.4.1 Background

The mass production of the SrO-(001)-STO nanocuboids is particularly challenging compared to the TiO<sub>2</sub>-(001)-STO nanocuboids due to the low yield. Additionally, the SrO nanocuboids are coated with a layer of strongly bounded carboxylate groups, as shown from the TEM and FTIR results in Ref. [70]. The long-chain (18 carbon) carboxylate groups make the oleic acid difficult to remove. In order to remove the oleic acid, the as-synthesized SrO-(001)-STO nanocuboids were heated at 450 °C for 3 h. However, the SrO nanocuboids sintered and the facets were distorted after the thermal treatment. The distorted nanocuboids no longer serve as a suitable nanopolyhedra support. Therefore, an alternative oleic acid-free method for synthesizing the SrO-(001)-STO nanocuboids is required. The “short carboxylic acid”

synthesis and the “octanoic acid-butanol” synthesis were investigated as possible methods to synthesize the oleic acid-free SrO-(001)-STO nanocuboids. The syntheses and results are presented in the following paragraphs.

## **6.4.2 Short Carboxylic Acid Synthesis**

### **6.4.2.1 Background**

The termination of the STO nanocuboid surfaces are dictated by the acidity and solubility of the acid added in the synthesis. In the acetic acid-assisted TiO<sub>2</sub>-(001)-STO synthesis, the highly soluble acetic acid reacts with the basic SrO, resulting in acidic TiO<sub>2</sub>-terminated surfaces. As the chain length of the acid increases, its solubility decreases. In the oleic acid synthesis, the SrO surface termination is favored because the strongest base in the system, the SrO, pairs with the weak oleic acid [70].

Based on the arguments above, a weak (or short-chain) carboxylic acid may lead to the formation of SrO surface termination. The shorter chain will make the surfactant removal process easier. The "short carboxylic acid" synthesis modified the original TiO<sub>2</sub>-(001)-STO synthesis by substituting the acetic acid with various three to seven-carbon carboxylic acids. The following paragraphs present the "short carboxylic acid" synthesis as well as the results and discussion.

### **6.4.2.2 Synthesis**

Several carboxylic acids as shown in Table 6.1 were substituted into the acetic acid STO synthesis. The details of the synthesis are as follows:

Solution A was prepared by dissolving 2.43 g Sr(OH)<sub>2</sub>·8H<sub>2</sub>O (Alfa-Aesar, 99%) into 50 mL

of 1.1M carboxylic acids. The volumes of the carboxylic acids added to solution A can be referred to in Table 6.1. Solution B was prepared by mixing 1 mL TiCl<sub>4</sub> (Acros Organics, 99.9 %) to 20 mL of 200 proof ethanol alcohol. After that, solution B was added slowly into A under a moderate stirring rate for at least 10 min. Then, 5 g NaOH pellets (Fisher) were added to the solution and stirred for at least 10 min. The suspension was loaded into a 125 mL Teflon-lined autoclave (Parr, model 4748) and heated with a ramping rate of 0.5 °C/min to 240 °C for 48 h. The autoclave was subsequently allowed to cool to room temperature. The sedimentation was washed thoroughly with deionized water and dried at 80 °C for 12 h in the air.

Table 6.1 List of the carboxylic acids used in the short carboxylic acid synthesis

<b>Name of acid</b>	<b>Number of carbon</b>	<b>pKa</b>	<b>Volume (mL)<sup>a</sup></b>	<b>Solubility in water at RT</b>
Acetic acid (C2)	2	4.76	3.15	miscible
Propionic acid (C3)	3	4.88	4.12	miscible
Valeric acid (C5)	5	4.82	2.67	4.97 g/100 mL
Capronic acid (C6)	6	4.88	0.58	1.08 g/100 mL
Heptanoic acid (C7)	7	4.89	0.13	0.24 g/100 mL

<sup>a</sup> Volumes of the carboxylic acids being added to the 50 mL, 1.1M water-based solution, as described in Section 5.4.4.2.

### 6.4.2.3 Results and Discussion

Figure 6.4 shows the morphology of the nanoparticles synthesized using C2, C3, C6 and C7 acids are almost identical. The result using C5 acid, however, shows three different shapes: rough

cuboids, sharp cuboids, and some rod-like structure in the TEM image, as shown Figure 6.5. It is not yet clear why the addition of C5 acid resulted in the three different types of nanoparticles.

Carboxylic acid molecules with longer carbon chains have lower solubility in water because the carbon chain is hydrophobic. For C6 and C7 acids, the carboxylic acids are almost immiscible with water. This indicates the carboxylate ions may not directly participate in the hydrothermal reaction.

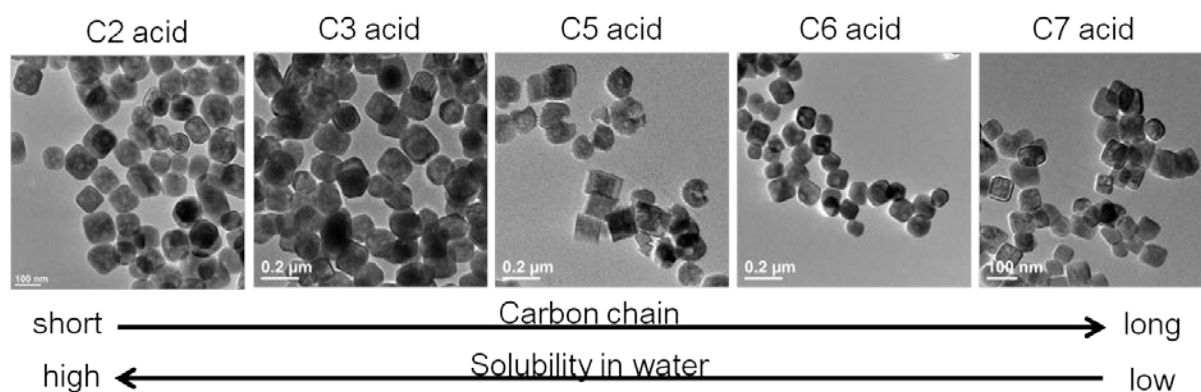


Figure 6.4 TEM images of C3 to C7 carboxylic acids substituted for the original acetic acid-assisted synthesis.

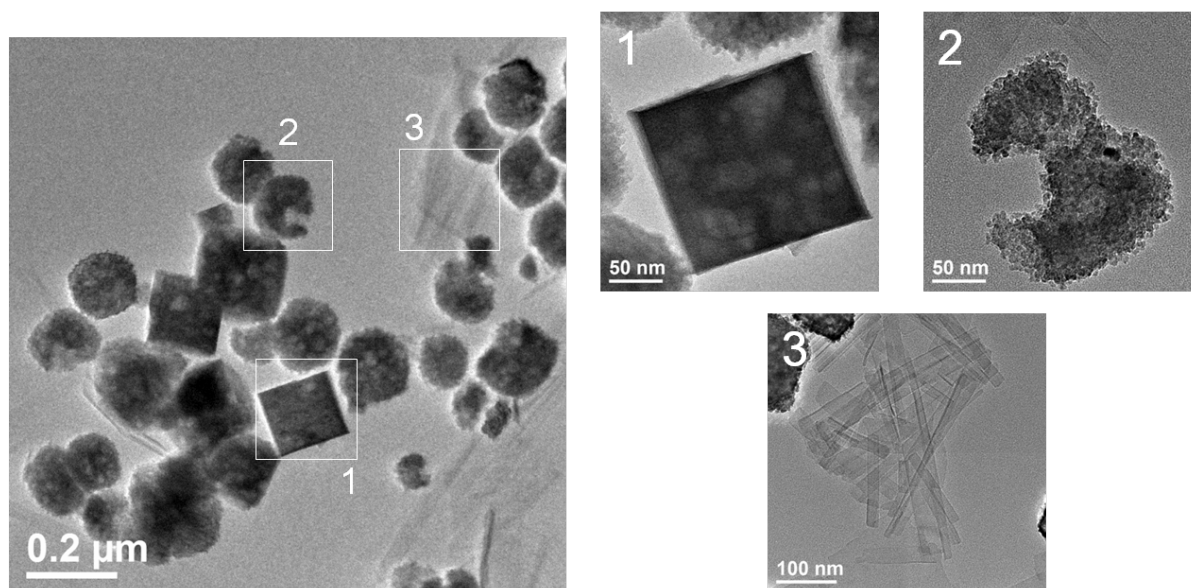


Figure 6.5 TEM images of the three types of particles resulting from the C5 acid substituted for the original acetic acid-assisted synthesis: 1. sharp cuboids, 2. rough cuboids, and 3. rod-like structures.

To further investigate the function of the acetic acid in the original  $\text{TiO}_2$ -STO synthesis, the acetic acid was replaced by the same concentration of HCl or by pure water. Figure 6.6 reveals that nanocuboids form in both of cases. The results imply that the presence of the acid is not the main component affecting the formation or shape of the STO nanocuboids

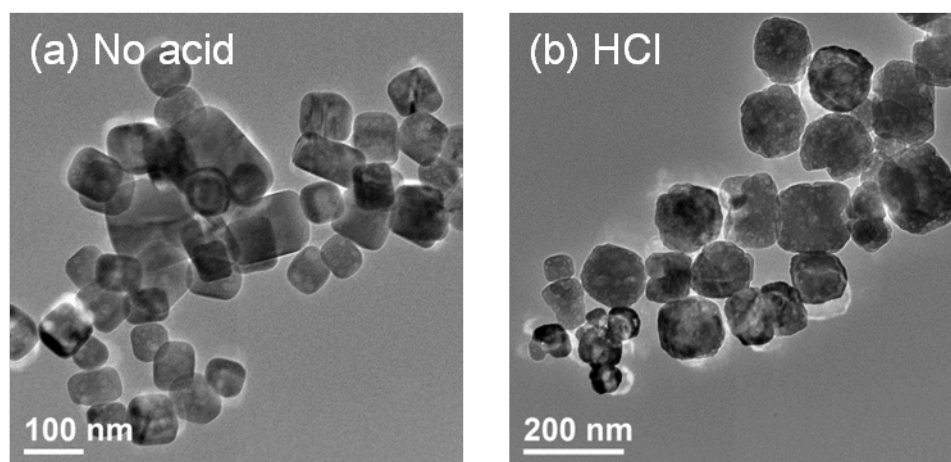


Figure 6.6 Results of replacing the 1.1M acetic acid in the  $\text{TiO}_2$ -(001)-STO synthesis with (a) pure water and (b) 1.1M HCl in the original acetic acid-assisted synthesis.

### 6.4.3 Octanoic Acid-Butanol Synthesis

#### 6.4.3.1 Background

In addition to the “short carboxylic acid synthesis,” another attempt to produce SrO-terminated STO nanocuboids was made by recreating the lamellar microemulsion structure similar to that in the oleic synthesis with shorter carbon chains. Microemulsions are defined as the structures that a mixture of oil, water, and surfactant can make [141,142]. The variation of microemulsion structures can be modeled using ternary phase diagrams [143]. To reproduce the lamellar microemulsion structure, a phase diagram regarding the components in the original synthesis (water/ethanol/oleate) will be informative in pinpointing the phase region that results in the lamellar microemulsion structure. However, the phase diagram for water/ethanol/oleate has not yet been published.

As an alternative, the phase diagram of water/butanol/sodium octanoate (caprylate) is available in Ref. [143]. In Figure 6.7, Region D shows the composition range for the lamellar

structure. The water/butanol/sodium octanoate phase diagram has a well-defined lamellar region that allows each of the composition limits to be adjusted by approximately 20%. Therefore, the water/butanol/sodium octanoate system was chosen as the target system to recreate the lamellar structure and the SrO-terminated STO nanocuboids.

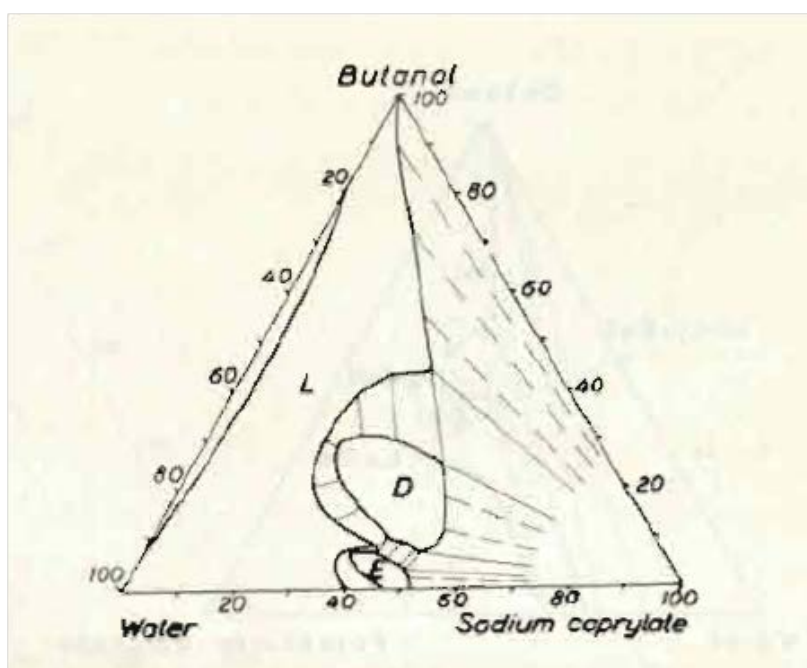


Figure 6.7 Ternary phase diagram of water/butanol/sodium octanoate (caprylate) at room temperature (Source: copied from page 113 of Ref. [143].) L and D are the micelle and lamellar regions, respectively. Note that the unit of the phase diagram is wt% instead of molar%.

#### 6.4.3.2 Synthesis

Multiple component points in the water/butanol/sodium octanoate phase diagram are chosen in order to pinpoint the possible compositions that will lead to the lamellar structure (region D).

The chemical compositions of the samples (A-F) are listed in Table 6.2, and the synthesis is described below:

Solution A was prepared by dissolving  $\text{Sr}(\text{Ac})_2$  into water. Then, octanoic acid was added and the mixture was stirred until  $\text{Sr}(\text{Ac})_2$  was fully dissolved. Solution B was prepared by mixing  $\text{Ti}(\text{O}i\text{Bu})_4$  with butanol. Solution A was added slowly into B under a moderate stirring rate for at least 10 min with rigorous stirring. Then, NaOH was added to the solution, forming a viscous suspension. The viscous suspension was then stirred at least for 10 min. The suspension was loaded into a 125 mL Teflon-lined autoclave (Parr, model 4748), and heated to 180 °C with a ramping rate of 0.5 °C/min and was held for 10-12 h. The autoclave was cooled at room temperature, and the white sedimentation was washed thoroughly with deionized water and dried at 80 °C for 12 h in the air. The detailed amount of chemicals added in the synthesis can be found in Table 6.2.

Table 6.2 The table shows the volumes of Sr(OAc)<sub>2</sub>, Ti(OBu)<sub>4</sub>, octanoic acid, butanol, and water used in the octanoic-butanol synthesis. Samples A-F were prepared by utilizing various chemical compositions as described.

<b>Sample no.</b>	<b>Sr(Ac)<sub>2</sub> (g)</b>	<b>Ti(OBu)<sub>4</sub> (mL)</b>	<b>Octanoic Acid (mL)</b>	<b>Butanol (mL)</b>	<b>Water (mL)</b>	<b>10M NaOH (mL)</b>	<b>NaOH (g)</b>
A	0.43	0.25	1.2	40	7.5	3	0
B	2.1	3.4	30	17	26	12.5	0
C	2.1	3.4	51	15	6	12.5	0
D	2.0	3.4	43	21	7.5	0	3
E	2.0	3.4	4	30	37.5	0	5
F	2.0	3.4	3	48	20.5	0	5

\* All of the samples were thermally treated under 180 °C, 12 h with a 1 °C/min ramp rate, except for A and B, which are under 180 °C, 10 h with a 1 °C/min ramp rate.

#### 6.4.3.3 Results and Discussion

The results in Figure 6.8 show a variety of nanoparticle shapes, including rods (E, F), sheets (D), cuboids (B) and spheres (A, C). The various shapes of the nanoparticles suggest that the growth might be influenced by different types of microemulsions. Because the phase diagram applied was the water/butanol/sodium octanoate system at room temperature instead of water/butanol/octanoic acid at 180 °C hydrothermal treatment, the boundary of the phase regions are expected distorted. Therefore, the composition used in the synthesis may not result in the desired microemulsion at the reaction temperatures. Additionally, the samples were characterized solely by using TEM to show the morphology. To confirm the crystal structure and compositions of the various particles, XRD and XPS are required.

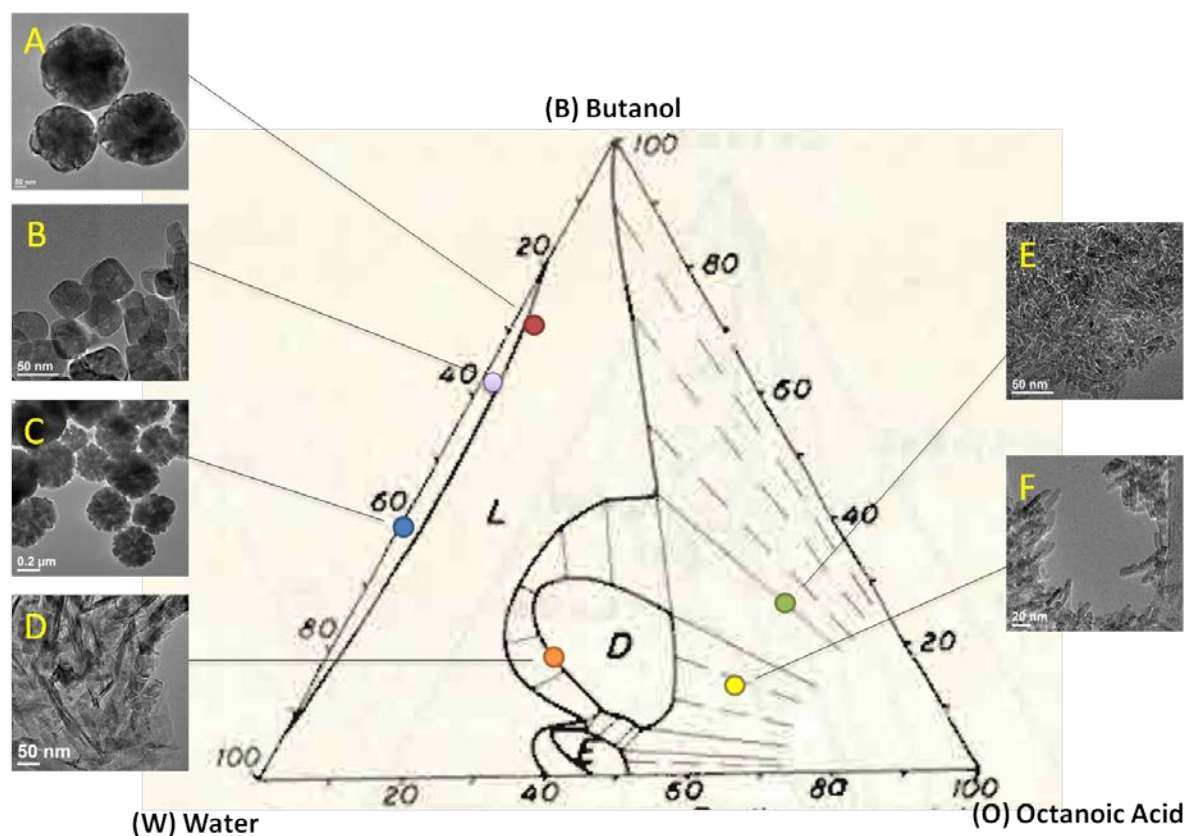


Figure 6.8 Preliminary results of the octanoic acid-butanol synthesis. The compositions and the corresponding results are shown accordingly. The TEM images marked with A-F are the nanoparticles synthesized based on the chemical composition listed in Table 6.2. (Image D and F provided by Lawrence A. Crosby)

## 6.5 Glycerol-Assisted Synthesis of (110)-STO Nanododecahedra

### 6.5.1 Background

As we were able to successfully demonstrate the syntheses of the  $\text{TiO}_2$ -(001) and  $\text{SrO}$ -(001) nanocuboids, our interest expands to the synthesis of STO nanopolyhedra with other low-index planes. Dong et al. [144] provided a detailed study in controlling the ratio of (110) to (001) facets on STO nanocrystals by using alcohols with different pKa values and concentrations as

surfactants. In this work, the proportion of the (110) facets increases with the addition of lower pKa alcohols, such as glycerol. Based on the result, glycerol was chosen as a surfactant to synthesize STO nanopolyhedra with predominantly (110) facets.

### 6.5.2 Synthesis

The synthesis of (110)-STO nanododecahedra was developed with the help of Robert M. Kennedy and Lawrence A. Crosby. The synthesis procedure was modified from Ref. [144] and has been reported in Ref. [45] by Crosby et al. The primary modifications include the use of titanium tetrabutoxide ( $\text{Ti}(\text{OBu})_4$ ) instead of titanium tetrachloride ( $\text{TiCl}_4$ ) as a titanium precursor, the use of strontium acetate ( $\text{Sr}(\text{Ac})_2$ ) instead of  $\text{SrCl}_2$ , and the use of sodium hydroxide ( $\text{NaOH}$ ) instead of lithium hydroxide ( $\text{LiOH}$ ). Additionally, the solution was not chilled in an ice bath. With these changes, the details of the synthesis are as follows:

Solution A was prepared by dissolving 2.9 mL acetic acid into 37.1 mL deionized water, then adding 1.9 g  $\text{Sr}(\text{Ac})_2$  while stirring. Solution B was prepared by adding 3.1 mL  $\text{Ti}(\text{OBu})_4$  to 31.5 g of glycerol while stirring for at least 5 minutes. Solution A was then added to solution B while stirring for at least 2 minutes. Then 10 mL of 10 M  $\text{NaOH}$  was added dropwisewhile stirring. The resulting mixture (translucent yellow-white) was placed into a 125 mL Teflon-lined autoclave (Parr, model 4748) for 36 - 48 h of thermal treatment at a temperature of 240 °C, with a ramping rate of 1 °C/min for heating. The resulting white powder was washed by dispersing it in water and centrifuging it repeatedly until the pH was neutral as measured by pH strips, then dried in an oven at 80 °C overnight.

### 6.5.3 Characterization

The TEM measurements were performed by Laurence A. Crosby. TEM samples were prepared by suspending a few milligrams of powder in approximately 10 mL of ethanol and sonicating for 15 minutes. The dispersed nanoparticles were then drop-cast with a pipet onto lacey carbon TEM grids. The samples were characterized with several microscopes including a Hitachi HD2300 equipped with a secondary electron detector, a probe-corrected JEOL ARM 200CF, and the Argonne chromatic aberration-corrected TEM (ACAT, a FEI Titan 80-300 ST. with a Cs/Cc image corrector) at Argonne National Laboratory. X-ray diffraction (XRD) samples were prepared by compacting several grams of the powder sample into a pellet on a low background glass slide. In order to identify the phase purity of the synthesized sample, the survey scattering profile was completed with an Ultima X-ray diffractometer (Rigaku), with a Cu  $K\alpha$  source operating at 40 kV. To minimize the instrument peak width when calculating the crystallite size, an ATXG X-ray diffractometer (Rigaku) equipped with a Ge (111) monochromator was utilized.

### 6.5.4 Results and Discussion

The images of the (110)-terminated STO nanododecahedra are shown in Figure 6.9. Some of the nanododecahedra show slight sintering as shown in Figure 6.9(a). Nevertheless, the nanododecahedra still have well-defined (110) surfaces, and the majority of the particles imaged exhibited sharp faceting with little, if any, corner rounding. As the (110)-STO nanododecahedra have well-defined (110) surfaces with minimal corner rounding, they can still serve as a nanopolyhedra catalyst support. The Standard Brunauer-Emmett-Teller (BET) analysis

determined that the surface area is  $4 \text{ m}^2/\text{g}$ .

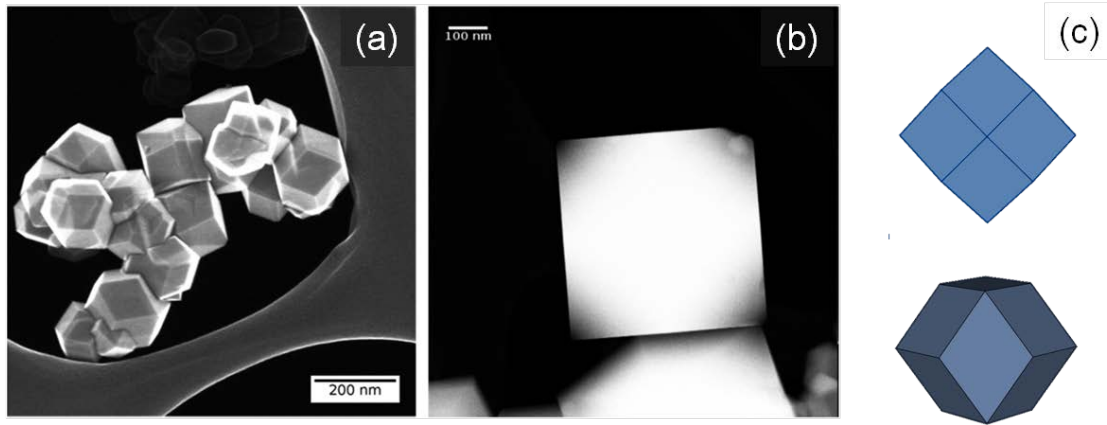


Figure 6.9 (a) Low-magnification SEM and (b) HAADF images demonstrating the dodecahedral shape of the nanoparticles. The three-dimensional characters are evident in (a), and are shown in (b) via intensity changes at the corners. The geometry of a dodecahedron is illustrated in (c). (Source: (a) and (b) were provided by Lawrence A. Crosby and were published in Ref. [45].)

The XRD pattern of the STO dodecahedra is shown in Figure 6.10, in which the Bragg peaks were indexed clearly. From the XRD profile, all of the major diffraction features of the powder sample can be identified as cubic  $\text{SrTiO}_3$  with negligible impurities. The positions and the relative intensities in between the peaks are consistent with  $\text{SrTiO}_3$  with a lattice constant of  $3.903 \text{ \AA}$ . The Scherrer equation [145] is used to analyze the crystalline domain size of the STO nanoparticles

$$L_{\text{hkl}} = \frac{0.9\lambda}{\beta \cos\theta} \quad , \quad (6.1)$$

where  $L$  is the crystalline size in the [hkl] direction, 0.9 is the Scherrer constant,  $\lambda$  is the incident X-ray wavelength (1.542 Å for Cu K $\alpha$  source),  $\theta$  is the angular peak position, and  $\beta$  is the integral breadth. Figure 6.11 shows the (110) diffraction peak of the nanododecahedra. The peak shape was fitted using a Lorentzian function given by

$$f(x) = A \frac{w/2}{(x-x_0)^2+(w/2)^2} + Bx + y_0 \quad , \quad (6.2)$$

where  $A$  is the scaling factor,  $B$  and  $y_0$  are the fitting constants for the linear background, and the  $w$  and  $x_0$  terms give the peak full width half maximum (FWHM) and the position, respectively. The integral breadth ( $\beta$ ) for the Lorentzian peak shape is related with the FWHM via [146]:

$$\beta = \left(\frac{\pi}{2}\right) FWHM \quad (6.3)$$

The additional peak broadening by the instrument contribution was also taken into consideration in determining the peak broadening contributed by the crystallite size. 325 mesh single crystal Si powder was used as a standard to determine the instrumental peak width. The Si powder has a large crystallite size (44  $\mu\text{m}$ ), which minimized the peak broadening from size effects (Figure 6.11). For Lorentzian peaks, the peak width due to the size of the crystalline domains is obtained by subtracting the instrumental width from the measured peak width. The calculation led to an average crystalline domain size of 180 nm, which is consistent with that observed by TEM.

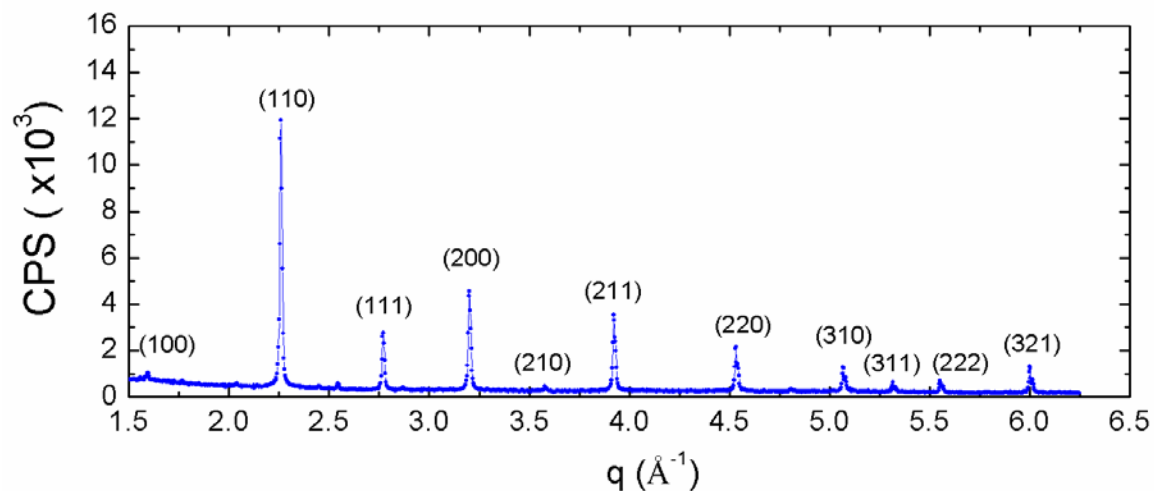


Figure 6.10 XRD pattern for the STO nanodecahedra.

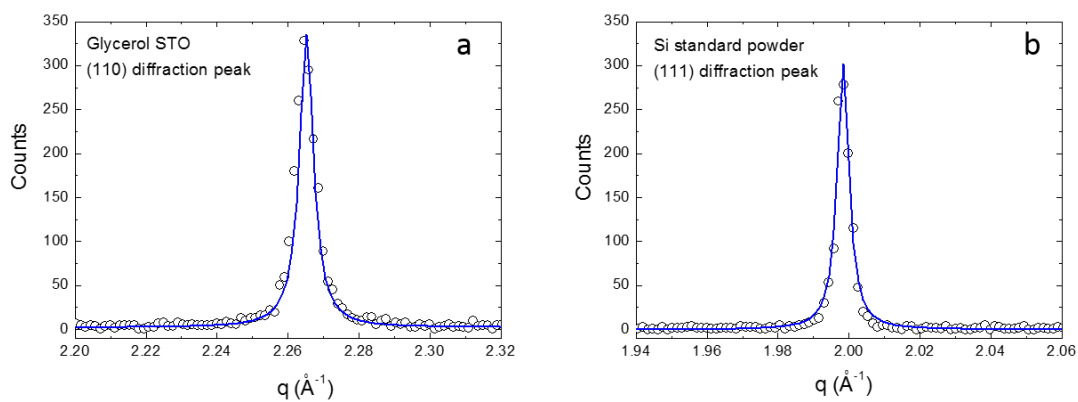


Figure 6.11 XRD peaks of (a) the (110) peak of the STO dodecahedra and (b) the (111) peak of the 325 mesh Si powder. By applying the modified Scherrer equation (6.1), the mean crystallite size in the  $[hkl]$  direction can be determined from the broadening of the  $(hkl)$  diffraction peak.

The surface structure of the (110)-STO nanododecahedra exhibits a complex ( $n \times 1$ ) reconstruction. From the HREM images (Figure 6.12), the surface is determined to be a combination of  $(3 \times 1)$  and  $(4 \times 1)$  reconstructions. Similar reconstructions were previously observed in a bulk (110)-STO single crystal surface [78].

Glycerol may serve as either a co-solvent, surfactant, or both. It alters the kinetics of growth and/or the thermodynamics to stabilize the the STO(110) surface. The (110) facets are small in the equilibrium Wulff shape of STO in oxygen. In the work of Crosby et al. [140], the  $\text{TiO}_2$ -(001)-STO nanocuboids had to be annealed over 700 °C to reveal distinctive (110) facets at the edges and corners. Therefore, the surfactant should have a significant influence on the (110)-STO nanopolyhedra synthesis. In our case, the reconstructions on the (110) surfaces are stabilized during the nanoparticle growth, and remain stable as the samples are stored at ambient conditions.

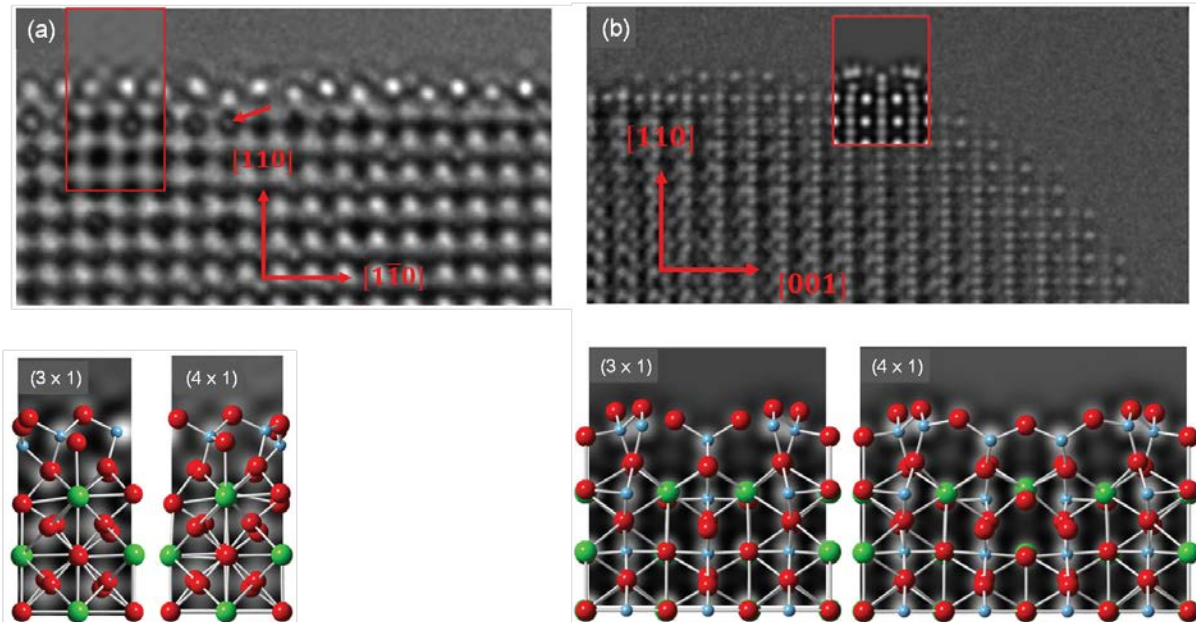


Figure 6.12 (a) Experimental images down the  $[001]$  zone and the simulated result (red box) for a  $(3 \times 1)$  reconstruction. The inset images below shows the simulations for the  $(3 \times 1)$  and  $(4 \times 1)$  reconstructions with the atomic structures superimposed. (b) Experimental images down the  $[1\bar{1}0]$  zone and the simulated result (red box) for a  $(4 \times 1)$  reconstruction. The inset images below shows the simulations for the  $(3 \times 1)$  and  $(4 \times 1)$  reconstructions with the atomic structures superimposed. The  $(3 \times 1)$  gave the best fit to experiment for this area, although in other regions it was the  $(4 \times 1)$ . (Source: Ref. [45], HREM images and the analysis provided by Lawrence A. Crosby)

## 6.6 Summary

The synthesis of the  $\text{TiO}_2$ -(001)-STO and (110)-STO nanopolyhedra with consistent reproducibility can be used in catalytic reaction testing. Several attempts to synthesize surfactant-free SrO-(001)-STO nanocuboids are also reported in this chapter. This include the “short carboxylic acid” method and the “octanoic acid-butanol” method. Further development of an alternative synthesis is still ongoing, and this chapter serves as a reference for continuing this research.

## Chapter 7: In-situ XAS Study of the Reduction of Pd Surface Complex

### Supported on $\gamma\text{-Al}_2\text{O}_3$

#### 7.1 Introduction

This chapter presents the characterization of small and mono-dispersed Pd nanoparticles synthesized from a newly developed grafting reaction of  $\text{Pd}(\text{acac})_2$  on  $\gamma\text{-Al}_2\text{O}_3$ . In most of the conventional preparations of supported metal nanoparticles, a metal precursor is deposited on an oxide support via an impregnation method and reduced with  $\text{H}_2$  at elevated temperatures. Reduction of the metal precursor induces the formation of metal nanoparticles. In the reduction process, the conditions have to be carefully controlled since small nanoparticles are thermodynamically unstable under heat treatment. Heat treatment may induce sintering of the nanoparticles, which is a challenge for synthesizing small and monodispersed metal nanoparticles.

The new approach introduced in this chapter creates monodispersed Pd nanoparticles under a mild reduction condition of the supported single-site  $(-\text{AlO}_x)\text{Pd}(\text{acac})$  complex (Figure 7.1). After reduction, monodispersed Pd nanoparticles can be prepared directly. A previous experiment of the  $(-\text{AlO}_x)\text{Pd}(\text{acac})$  complex on  $\gamma\text{-Al}_2\text{O}_3$  suggested its stability under a 1-octene reduction treatment up to 120 h at room temperature. As shown in Figure 7.2, the particle size and distribution was not changed significantly at 24, 72, and 120 h.

In order to further study the formation mechanism of the Pd nanoparticles, especially at the very early stage of particle formation, in-situ XAS experiments are designed to measure the change in chemical state and local coordination environment of Pd in the  $(-\text{AlO}_x)\text{Pd}(\text{acac})$  complex under reduction gas flow.

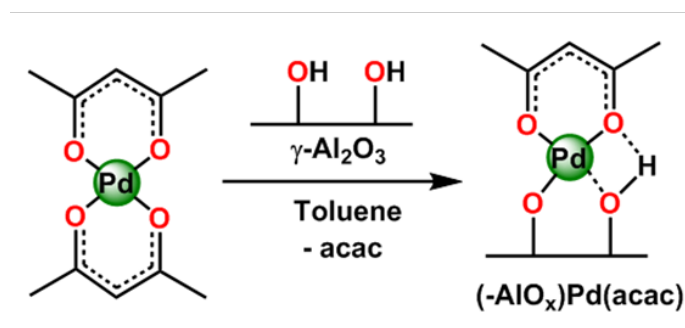


Figure 7.1 Synthesis and proposed structure of the  $(-\text{AlO}_x)\text{Pd}(\text{acac})$  complex. (Image provided by Aidan R. Mouat)

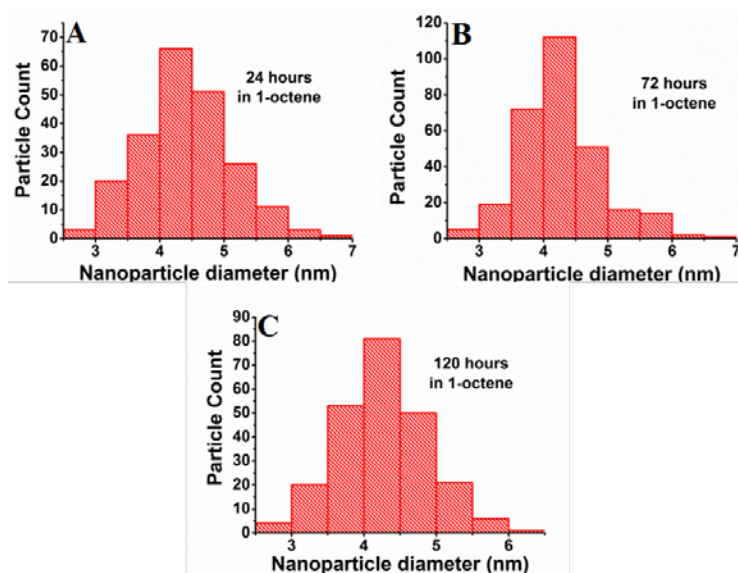


Figure 7.2 Histograms of Pd nanoparticle diameters extracted from TEM images: size distributions when the  $(-\text{AlO}_x)\text{Pd}(\text{acac})$  complex reduced in 1-octene at room temperature for (a) 24 h (b) 72 h and (c) 120 h. (TEM and image analysis provided by Aidan R. Mouat and Cassandra L. Whitford.)

## 7.2 Synthesis

The synthesis method was provided and completed by Aidan R. Mouat. Detailed synthesis of the  $(-\text{AlO}_x)\text{Pd}(\text{acac})$  complex are presented below:

Prior to reaction, all glassware was dried at 150 °C overnight and cooled under dynamic vacuum. Calcined  $\gamma\text{-Al}_2\text{O}_3$  (5.0 g) was treated similarly and held under an atmosphere of  $\text{N}_2$  after cooling. In a separate flask, 0.36 g  $\text{Pd}(\text{acac})_2$  (1.1 mmol, 2.5wt% Pd) was dissolved in ca. 25 mL of anhydrous toluene. The golden solution was cannulated onto the  $\gamma\text{-Al}_2\text{O}_3$  under  $\text{N}_2$  and the resulting suspension stirred for 18 h at room temperature. The suspension was allowed to settle and the golden mother liquor cannula filtered off the solid. The solid was then washed twice with 25 mL of anhydrous toluene under  $\text{N}_2$ , filtering off the wash liquid in the manner previously described. When the wash was no longer colored, the solid was suspended in hexanes and vacuum filtered in open air. The resulting beige solid was further washed with hexanes to remove excess toluene and dried under dynamic vacuum at 25 °C overnight prior to further experiments. After preparation, the solid could be stored under ambient conditions indefinitely with no observable degradation of the  $(-\text{AlO}_x)\text{Pd}(\text{acac})$  surface complex. ICP analysis of several preparations of the material indicated the Pd loading to be  $0.20 \pm 0.01\%$  Pd. The as synthesized  $(-\text{AlO}_x)\text{Pd}(\text{acac})/\gamma\text{-Al}_2\text{O}_3$  sample is a gray powder.

## 7.3 Characterization Methods

XAS measurements were completed at beamline 5BM-D at the Advanced Photon Source (APS) of Argonne National Laboratory. The Pd atom oxidation states were analyzed by in-situ Pd K-edge (24.35 keV) XANES. A Linkum cell was used for the fluorescence mode XAS measurements (see Appendix A.3, Figure A2). XANES scans of the  $(-\text{AlO}_x)\text{Pd}(\text{acac})/\gamma\text{-Al}_2\text{O}_3$

were taken every other 6 min for the 9-hour experimental period under 10 sccm pure ethylene flow at 50 °C. Each scan takes approximately 6 min. At 1, 3, 6, and 9 h of the reaction, the ethylene flow was replaced by 50 sccm of He to seize the reduction, and Pd K-edge EXAFS scans were taken at room temperature.

The fractions of Pd<sup>2+</sup> ( $f_{\text{Pd}^{2+}}$ ) and Pd<sup>0</sup> ( $f_{\text{Pd}^0}$ ) were obtained from linear combination fitting analysis under the assumption of

$$f_{\text{Pd}^0} + f_{\text{Pd}^{2+}} = 1. \quad (7.1)$$

In data analysis, XANES spectra of the (-AlO<sub>x</sub>)Pd(acac) before reaction (Pd<sup>2+</sup>) and Pd foil (Pd<sup>0</sup>) were used as the standards in the linear combination fitting. The fitting range was -20 eV to +30 eV with respect to the Pd K-edge. ATHENA and ARTEMIS software packages [118] were used in data analysis.

#### 7.4 Results and Discussion

Figure 7.3(a) shows the evolution of the Pd K-edge XANES for the (-AlO<sub>x</sub>)Pd(acac) complex from 0 - 9 h under ethylene flow. The Pd K-edge and the line shape of XANES shifts from Pd<sup>2+</sup> to Pd<sup>0</sup> as the sample is reduced under ethylene flow. The EXAFS data also shows consistent results with XANES; namely that the Pd–Pd peak grows while the Pd–O peak diminishes, signifying an increase and decrease in coordination number, respectively, as presented in Figure 7.3(b). The trends that the  $f_{\text{Pd}^0}$  and  $f_{\text{Pd}^{2+}}$  change with the reduction time are plotted in Figure 7.4. At the beginning,  $f_{\text{Pd}^0}$  increases faster. After 3 h, the trend slows down and  $f_{\text{Pd}^0}$  seems to approach 60% at 9 h.

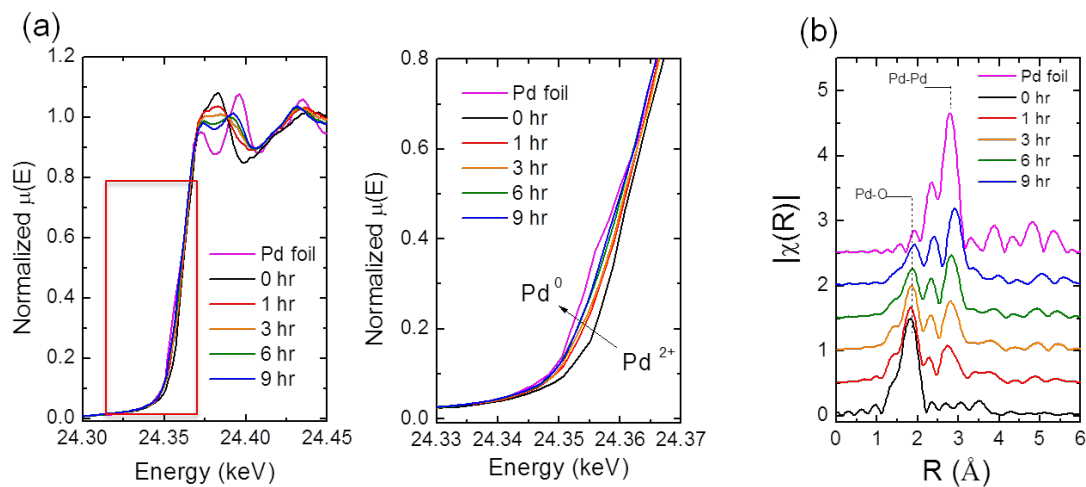


Figure 7.3 (a) XANES and (b) EXAFS data at the Pd K-edge of the  $(-\text{AlO}_x)\text{Pd}(\text{acac})$  complex under ethylene reduction from 0 to 9 h.

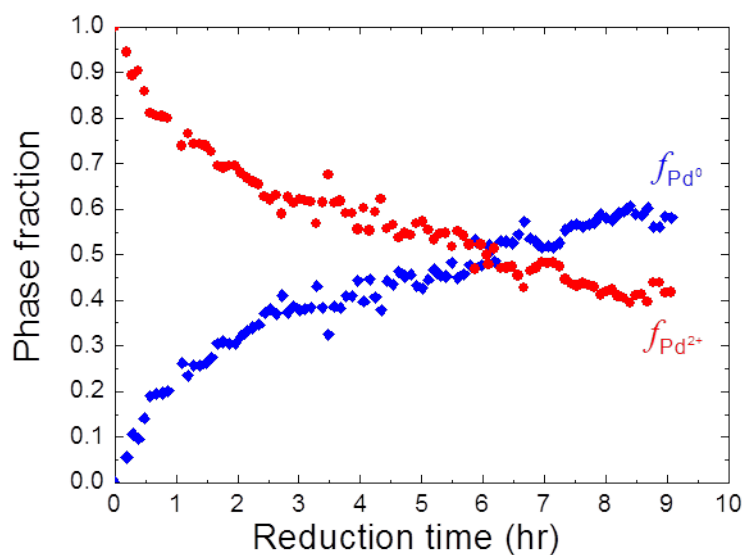


Figure 7.4 The evolution of  $f_{\text{Pd}^0}$  and  $f_{\text{Pd}^{2+}}$  with the ethylene reduction time. The phase fraction of Pd was obtained from the linear combination fitting of the  $\text{Pd}(\text{acac})_2$  and Pd foil reference XANES spectra.

## 7.5 Summary

The reduction process of the  $(-\text{AlO}_x)\text{Pd}(\text{acac})$  surface complex supported on  $\gamma\text{-Al}_2\text{O}_3$  under ethylene was analyzed by in-situ XAS. The result shows that Pd gradually reduces from  $\text{Pd}^{2+}$  to  $\text{Pd}^0$  from the 0 - 9 h time span, with fraction of  $\text{Pd}^0$  approaching ~60%. More efforts have to be spent in the future to analyze the reaction kinetics.

## Chapter 8: Conclusions and Future Directions

### 8.1 Conclusions

This dissertation discusses the morphology and CO oxidation activity of 1, 5, and 10c ALD-Pd nanoparticles supported on TiO<sub>2</sub>-(001)-STO nanocuboids, SrO-(001)-STO nanocuboids, and (110)-STO nanododecahedra synthesized by three separate hydrothermal processes.

TEM images show that ALD-Pd nanoparticles are well dispersed on the STO supports. The Pd nanoparticles have uniformly dispersed sizes between 2 to 5 nm depending on the number of ALD cycles. The nanoparticles show distinct morphology and growth modes on the three types of STO nanopolyhedra. The Pd nanoparticles on SrO-(001)-STO surface exhibit a lower degree of wetting and wider size distribution compared to the other two types of surfaces. On the TiO<sub>2</sub>-(001)-STO nanocuboids, Pd follows the nucleation and growth model and grows in size. In contrast, Pd nanoparticles on both SrO-(001)-STO nanocuboids and (110)-STO nanododecahedra grow in number density. HREM images show that single crystalline and twinned Pd nanoparticles co-exist on the TiO<sub>2</sub>-(001)-STO nanocuboids and (110)-STO nanododecahedra. However, more analysis has to be carried out to obtain the morphological information of the Pd nanoparticles, including the Winterbottom shape, twinning, and in-plane epitaxial relationship between Pd and STO. Additionally, XRF, ICP-AES, and XAS show that the loading of Pd and atomic fraction of Pd<sup>0</sup> increase monotonically with the number of ALD cycles on all of the STO supports.

The CO oxidation reaction was employed as a probe reaction to determine and compare the catalytic activity of Pd on TiO<sub>2</sub>-(001)-STO nanocuboids and (110)-STO nanododecahedra. The activity of CO oxidation is dependent on the proportion of the facets of Pd rather than the shape. TOF of CO oxidation shows that the smallest Pd nanoparticles (~ 1.7 nm) on TiO<sub>2</sub>-(001)-STO

have the highest CO oxidation activity, while the larger Pd nanoparticles (~ 3 nm) on both types of supports exhibit equivalent lower CO oxidation activity. The phenomenon is explained by DRIFTS analysis: For larger Pd nanoparticles, the activity is lower due to CO poisoning on the facet sites, thus the absorption of O<sub>2</sub> is prohibited. In contrast, the higher proportion of edge and corner sites on smaller nanoparticle allows O<sub>2</sub> absorption occurs more easily, leading to a higher activity.

Overall, this dissertation demonstrates the feasibility of applying STO nanopolyhedra system to bridge the surface science studies on single crystal supports and catalytic reaction studies on powder catalyst supports. This nanopolyhedra support approach has great potential to be further employed in other metal/support oxide systems.

## 8.2 Future Directions

### 8.2.1 Pd Supported on SrTiO<sub>3</sub> Single Crystal Surface

While the facets of STO nanopolyhedra supports resemble the surface of single crystal supports, X-ray scattering measurements are not applicable to the nanopolyhedra as with single crystal surfaces. The randomly aligned facets of STO nanopolyhedra supports cause difficulties in utilizing X-ray scattering techniques to obtain the structural information at the Pd/STO interface. To gain a full view of the interface structure, studying the Pd/STO single crystal system is required as a complement to the Pd/STO nanopolyhedra system. Previously, X-ray standing wave (XSW) and X-ray scattering (GISAXS) were employed to analyze the Pt/STO single crystal system. X-ray standing wave (XSW) is capable of probing the interface at the level of element-specific and atomic-scale imaging [147,148]. As demonstrated in Refs. [34,35], bonding configurations were resolved at the interface between sub-monolayer Pt and STO(001) by using XSW. In addition to XSW, grazing incident small angle X-ray scattering (GISAXS) provides information about morphological properties as a representative global average of nanostructured surfaces and thin films [149,150]. Refs. [31–33] demonstrated how GISAXS can be used to analyze the radius, height, and interparticle distance of ALD-Pt nanoparticles on STO(001) surface as a function of the number of ALD cycles.

Scanning probe microscopy is another surface science technique that only applies to flat surfaces. As demonstrated by Castell et al. [37,38], and Cuenya et al. [151], scanning tunneling microscopy (STM) and atomic force microscopy (AFM) identify the shape and orientation of the Pd nanoparticles supported on the single crystal STO substrates.

Furthermore, single crystal STO surfaces exhibit more than one types of reconstruction under different annealing conditions [79,152,153], which leads to various shapes of supported Pd

[37,38] nanoparticles due to the difference in interfacial crystallography (also see Section 2.2.3). Therefore, the Pd/STO single crystal system provides additional characterization platforms.

By studying Pd on STO single crystal surfaces with advanced X-ray characterization and surface science techniques, the atomic structures at the interface can be further established. The structural information obtained from the Pd/STO single crystal system can be combined with the catalytic information from Pd/STO nanopolyhedra system to gain a deeper understanding of the interface effect on catalytic performance.

### **8.2.2 Various Metal/ABO<sub>3</sub> Nanopolyhedra Catalytic System**

The interface epitaxy between the metal and oxide can provide extra stabilization of heterogeneous catalysts in catalytic reactions. For the Pt/STO nanopolyhedra system, STO has a nearly matching lattice constant with Pt, resulting in cube-on-cube epitaxy at the interface. This prevents particle sintering as shown in Refs. [10,25]. Substituting Sr with Ca or Ba into the STO structure is expected to cause the expansion of the lattice constant of STO. This increases the mismatch between Pt and the support. A similar argument can be applied to other metals (e.g. Pd, Au, or Ag) and other rare earth perovskite materials (e.g. LnScO<sub>3</sub>, LnGaO<sub>3</sub>). If the hydrothermal synthesis of rare earth perovskite nanopolyhedra supports is made possible, a series of lattice match and mismatch metal/oxide pairs can be created. Thus, the influence of interface epitaxy on catalytic activity can be investigated.

## APPENDIX

### Appendix A: An Operation Manual for XAS Measurements

#### A.1 XAS Measurement at the 5BM-D Beamline at the APS

##### A.1.1 Introduction

The DuPont-Northwestern-Dow (DND) 5BM-D beamline at the Advanced Photon Source (APS) of Argonne National Laboratory (ANL) is a bending magnet beamline that contains a dedicated extended X-ray absorption fine structure (EXAFS) setup. The energy range of 5BM-D is 4.5-80 keV with a beamsize of 15 mm wide by 5 mm high. This beamline is particularly well suited for *in situ* studies. In-situ flow cells and a gas manifold system are available at the beamline.

Appendix A serves as a general guide for XAS measurements at 5BM-D. A.1.2 through A.1.6 describe the measurement setups and operation procedures will be presented in detail. This appendix focuses on the preparation and measurements of powder samples. In A.1.5, common commands for the SPEC software control system are listed. SPEC is a UNIX-based software package for collecting X-ray data. A.1.6 introduces the procedure for file retrieval at 5BM-D. Basic XAS data reduction procedures will be presented in A.2. A.3 gives a brief introduction of the flow cells for *in-situ* XAS measurements. To learn further details of the theory, sample preparation, data reduction and analysis of XAS, readers are highly encouraged to read the following books and articles:

- Scott, C., (2013). *XAFS for Everyone*. Taylor & Francis Group.
- Bunker, G., (2010). *Introduction to XAFS: A Practical Guide to X-ray Absorption Fine Structure Spectroscopy*. Cambridge University Press.

- Newville. M., (2004). *Fundamentals of XAFS*.

### A.1.2 XAS Sample Preparation

There are several methods to prepare XAS powder samples. The method used should be determined by the concentration of the element(s) of interest, the nature of the sample itself, and the amount of the sample. Before sample preparation, the X-ray absorption length of the sample should be estimated from the composition of the sample. Hephaestus [118] is a program incorporated in the ATHENA software package for computing approximate X-ray absorption lengths ( $1/\mu$ ) for common or user-specified materials. One can also determine  $1/\mu$  from the CXRO web-site calculator [http://henke.lbl.gov/optical\\_constants/atten2.html](http://henke.lbl.gov/optical_constants/atten2.html). The thickness of the sample in the direction along the X-ray traveling path should not exceed one absorption length, or the data will suffer from self-absorption in fluorescence mode. Self-absorption diminishes the oscillating features in the EXAFS region, and thus causes difficulties in analyzing the data. When working with powder samples like supported catalysts, the size of the grains in the sample might exceed one absorption length, and procedures must be taken to ensure the grain sizes are smaller than the absorption length. Usually, grinding the sample with mortar and pestle is an effective way to reduce the grain size. Another method is using a sieve to select smaller particles. This also ensures a more uniform sample distribution. Also note that if two edges in the same material are measured, one should recalculate the absorption length and prepare samples accordingly.

The following are two sample preparation methods that are the most commonly used to prepare an XAS sample. 5-BMD provides sample holders compatible with either of the methods:

- Spreading the powder onto Scotch or Kapton tape.
- Pressing the powder into a self-supporting pellet.

The Scotch tape method is the easiest and most straightforward way to prepare the sample. Samples uniformly spread on multiple pieces of Scotch (3M) tape are stacked together to reach the desired thickness. However, in this case, the powder cannot be retrieved after the measurement for further studies. The pellet method allows the sample to be retrieved after the measurement, but when the concentration of the element of interest is high, the thickness of a self-supporting pellet usually exceeds the absorption length. A common solution is to add an X-ray-inert filler such as boron nitride (BN) as a spacer to help dilute the sample. The filler material must be X-ray-inert and non-interacting with the sample itself.

### A.1.3 Measurement Setup

XAFS measurement can be completed with transmission or fluorescence modes, which are referred to Section 3.3.3. Figure A1 presents photos taken during the measurement at 5BM-D.

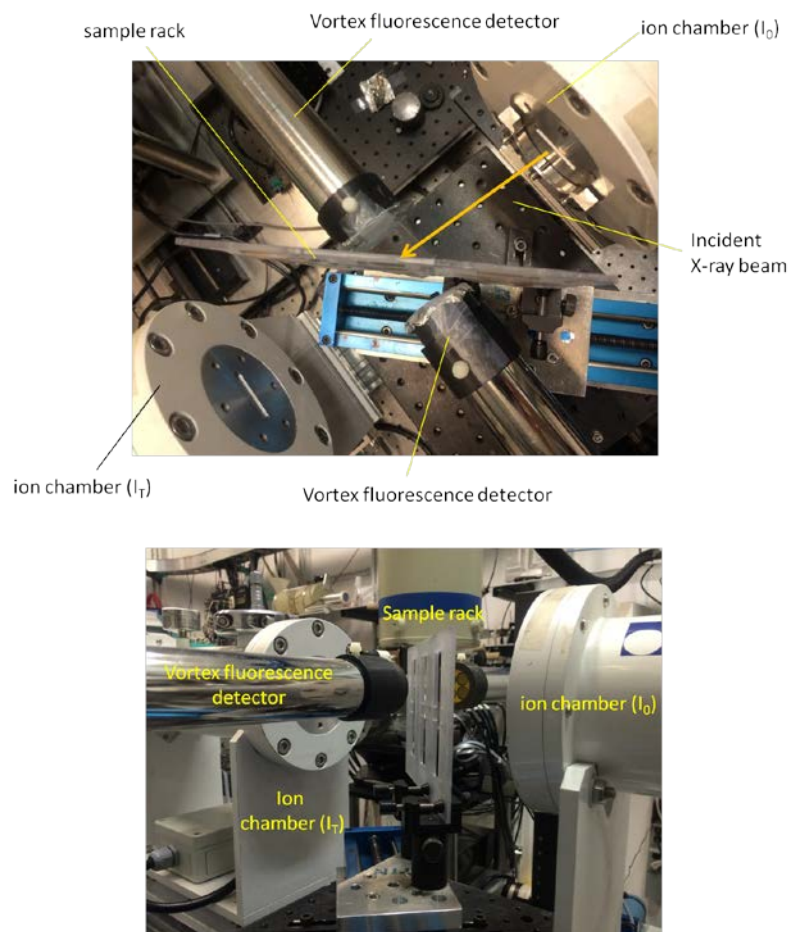


Figure A1: (Top) Top-view with sample held at  $45^\circ$  relative to the incident beam and XRF detector and (Bottom) side-view of the setup for fluorescence mode XAS measurements at 5BM-D. The fluorescence detector is usually set up at a  $90^\circ$  angle to the incident beam because the X-rays generated by the synchrotron radiation source are polarized in that direction. This reduces the inelastic and elastic scattering into the XRF detector. The sample rack is placed at  $45^\circ$  to maximize solid angle.

#### A.1.4 Beam Alignment and Data Acquisition

This is a guide for beam alignment and XAS data acquisition in fluorescence mode. Two Vortex-ME4 four-element silicon drift detectors (SDD)<sup>a</sup> are available at 5BM-D.

1. Adjust the position of the fluorescence detector to optimize the count rate. Make sure the detector dead time<sup>b</sup> is  $< 30\%$ . The dead time can be reduced by reducing the input count rate (ICR) or by reducing the peaking time<sup>c</sup> of the pulse height analysis system<sup>d</sup>. The input count rate and the output count rate (OCR) for each element of the Si drift diode fluorescence detector should not exceed  $10^5$  cps.
2. To avoid unwanted counts from low energy X-ray emission peaks, low-Z foil like Al can be inserted between the sample and detector to selectively absorb the lower energy photons. Consider the example of the sample: when measuring around the Pd  $K\alpha$  edge, the strong Sr  $K\alpha$  emission can be suppressed by inserting layers of Al foil in front of the four element detector.
3. Perform a transmission scan along the y- and z- axes across the sample to find the spot that maximizes the intensity. Move the sample holder to the optimized (y, z) spot.
4. Adjust the XAS scan parameters within the SPEC software control system. The parameters will influence the scan time and data quality. Typically, the scan time is adjusted such that the statistical error is less than 0.5% ( $\sim 100,000$  counts/energy value). The following is a list of commonly used scan parameters.

<b>Parameter</b>	<b>XANES scan</b>	<b>EXAFS scan</b>
Background start energy offset (eV)	-150	-250
Pre-edge start energy (eV)	-30	-30
EXAFS start $k$ ( $1/\text{\AA}$ )	3	3
EXAFS end $k$ ( $1/\text{\AA}$ )	10	13
Background energy increment (eV)	10	10
Pre-edge energy increment (eV)	2	2
$k$ increment ( $1/\text{\AA}$ )	0.07	0.07
Base count time (s)	1	1
Final $k$ count time (s)	1	15
$k$ weight in counting	1.5	1.5
Dark current time (s)	5	5
Monochromator setting time (s)	1000	1000
Estimated scan time (min)	5-7	20-30

5. Multiple scans are averaged to improve the quality of the data. One may average the scans during data acquisition and determine if more scans should be acquired.

<sup>a</sup>SDD is an energy-dispersive detector. It measures the energy of fluorescent X-ray photons by the amount of ionization produced when the photons interact with the high purity Si in the SDD. The number of electron-hole pairs produced is proportional to the X-ray photon energy.

<sup>b</sup>SDD requires a certain amount of time to process the incoming photons. The dead time is the time period during which the detector is unable to respond to further excitations.

<sup>c</sup> Peaking time is the time interval that is required for a pulse to go from the baseline to the peak.

<sup>d</sup> Pulse height analysis system processes the pulse created by the incoming X-ray photon. The height of the pulse is directly proportional to the energy of the X-ray photon.

### A.1.5 Common SPEC Commands

The following is a table listing the most commonly used SPEC commands for data acquisition at 5BM-D. The exact syntax for these commands can be found by typing these commands in SPEC.

<b>Command</b>	<b>Action</b>
<i>wu</i>	Show the position of all motors
<i>ct</i>	Count
<i>vortex_save</i>	Save the spectrum file as a .mcaspm text file
<i>umv</i>	Move the motor to the absolute coordinate
<i>umvr</i>	Move the motor with respect to the current position
<i>zsamp</i>	Move sample along z axis
<i>CEN</i>	Move the motor to the center of the peak.
<i>dscan</i>	Perform a scan that begins and ends at positions defined relative to the current motor position (see Eg. 1 below)
<i>ascan</i>	Perform a scan that begins and ends at defined absolute positions (See Eg. 2 below)

Example 1: *dscan Zsamp -1 1 30 2*. Here, the start and end positions are 1 mm below and above the current motor position. The Zsamp motor in this case is moved between the start and end points in 30 intervals, and the detector count time at each of these points is 2 s.

Example 2: *ascan Zsamp -5 5 30 2*. Here, the start and end positions are -5 mm and 5 mm with respect to the beam center that defined as  $z = 0$ . The Zsamp motor in this case is moved between the start and end points in 30 intervals, and the detector count time at each of these points is 2 s.

#### A.1.6 File Structure at 5-BMD

The acquired XAS data is a .dat file, which can be retrieved in real-time directly from the computer at 5BM-D through an Ethernet connection. The following is a guide to synchronizing the data with a MacOS system using Unix commands in the Mac:

Open Terminal (Application>>Utilities>>Terminal)

```
>> ping oyster1
```

```
>> cd desktop
```

```
>> cd file directory: folder
```

```
>> sftp user5bmd@oyster1
```

```
>> pw: Ilikefleas
```

```
sftp >> cd yyyy-m
```

```
sftp >> cd nu
```

```
sftp >> cd foldername
```

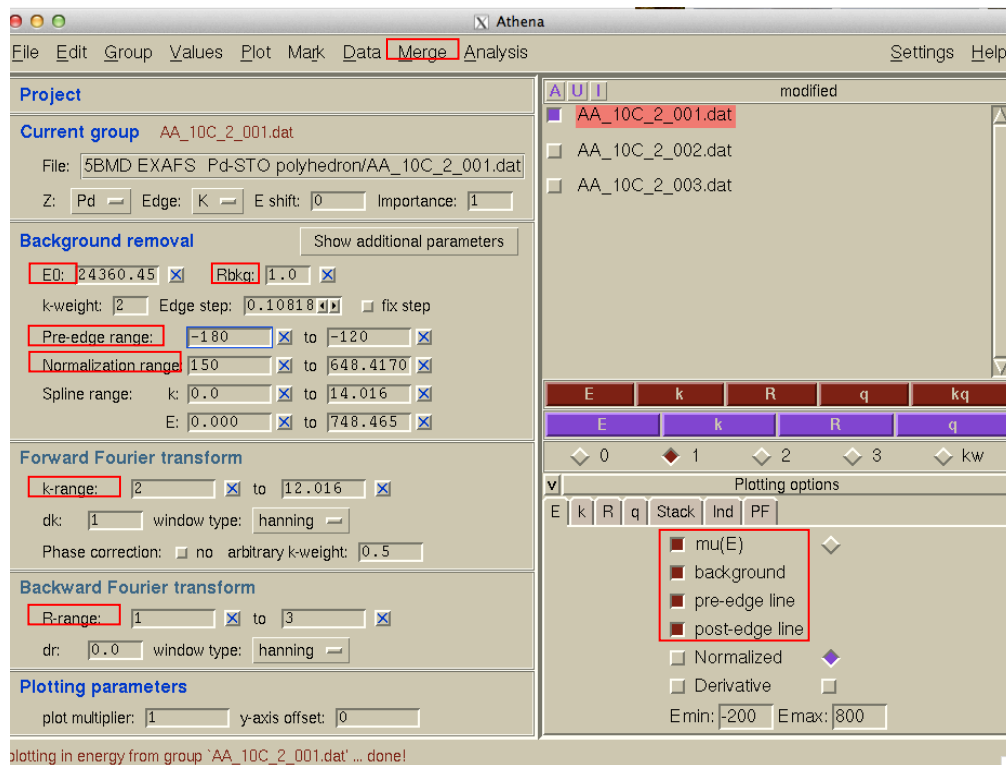
```
sftp >> ls /* view the contents in the folder
```

```
sftp >> mget (filename)* /* download all the file start with (filename)
```

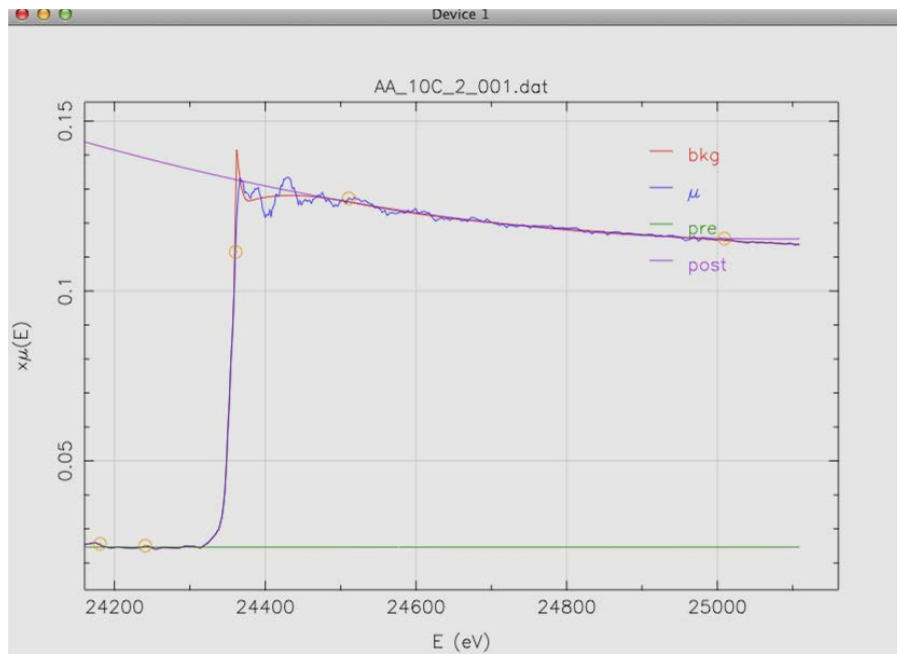
```
sftp >> mget *(.filetype) /* download all the file with a specific filename extension
```

#### A.2 Data Reduction Procedures

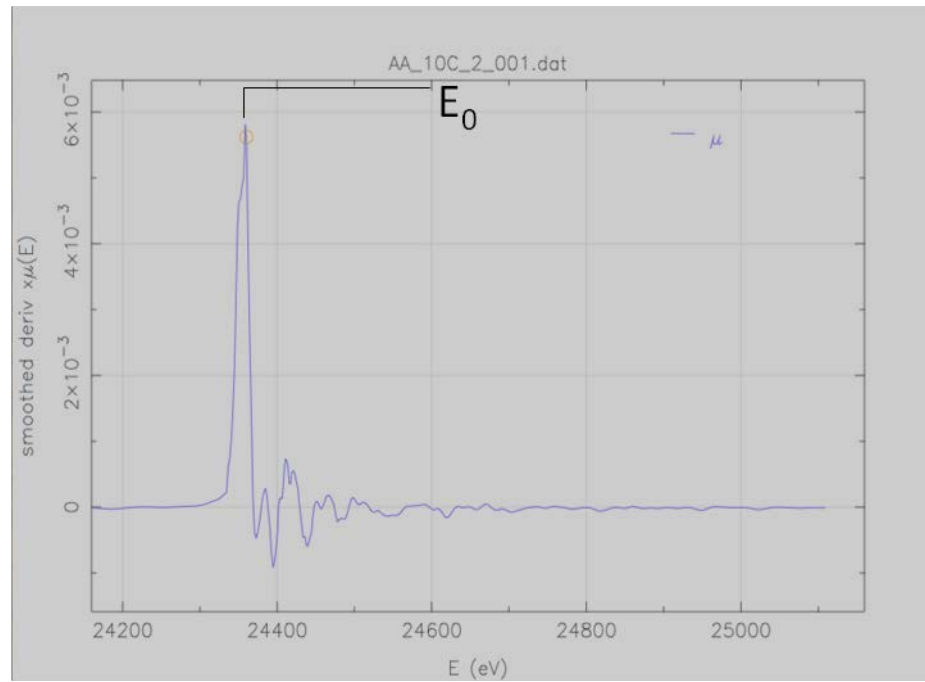
This is a step-by-step guide for data reduction using the ATHENA software package [118]. The following screen-shot shows the main window of ATHENA. Basic functions that will be introduced in the guide are marked in red frames.



1. Import the data and merge the multiple scan files by clicking **Merge** >> **Merge marked data in  $\mu(E)$** .
2. Adjust the pre-edge line by changing the values in the **Pre-edge range** function tab to the right of the main window. As shown in the following screen-shot, an ideal pre-edge line (green line) is horizontal. A typical energy range for the pre-edge line is -180 eV to -100 eV with respect to the edge position.



3. Adjust the post-edge line by changing the values in the **Normalization range** function tab below the **Pre-edge range** tab. The line shape of the post edge line reflects  $\mu \propto 1/E^3$ .
4. Determine the edge position ( $E_0$ ) by identifying the first maximum in the derivative of the absorption spectrum  $\mu(E)$ , which can be calculated via the **Derivative** function tab located at the lower right of the window. An example is shown in the following screen-shot.



5. Check the background. The background should follow through the center of the wiggling of the EXAFS range in a straight line. If the background mimics the oscillations too closely, some of the features of the spectra will be subtracted out.

### A.3 In-situ Flow Cells and the Gas Manifold System

A couple of in-situ flow cells are available at the 5BM-D beamline. Figure A2 to Figure A5 are images of the different types of flow cells.

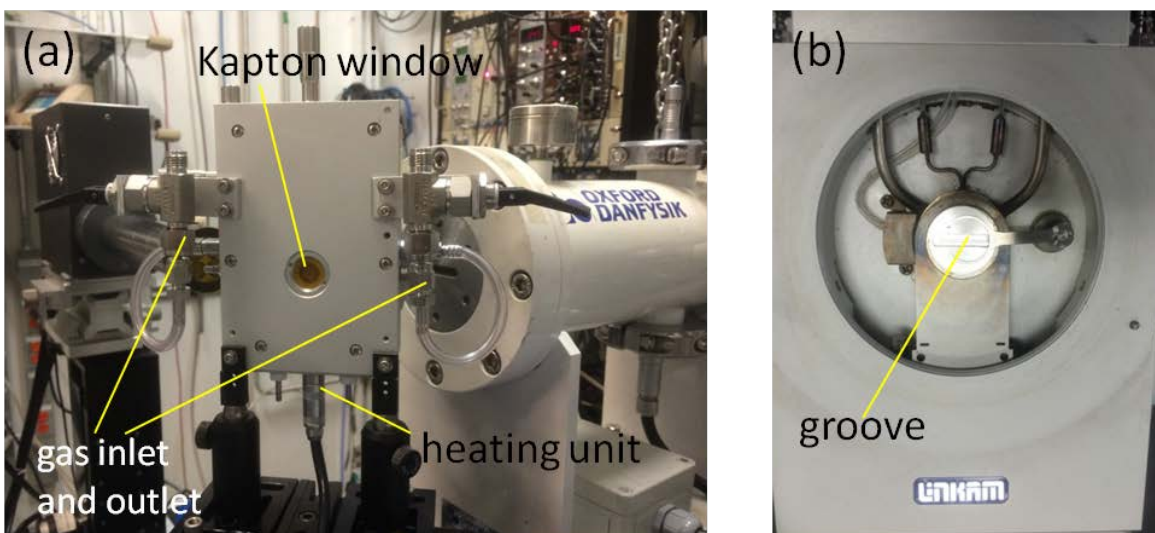


Figure A2: Images of a Linkam Cell. (a) Set up of the Linkam cell at the 5BM-D beamline and (b) close-up of the sample stage. The groove on the sample holder shown in (b) allows powder samples to be packed inside. Self-supported pellets are also compatible with the cell. The cell only supports measurements in fluorescence mode. The maximum temperature that can be reached within this cell is 250 °C.

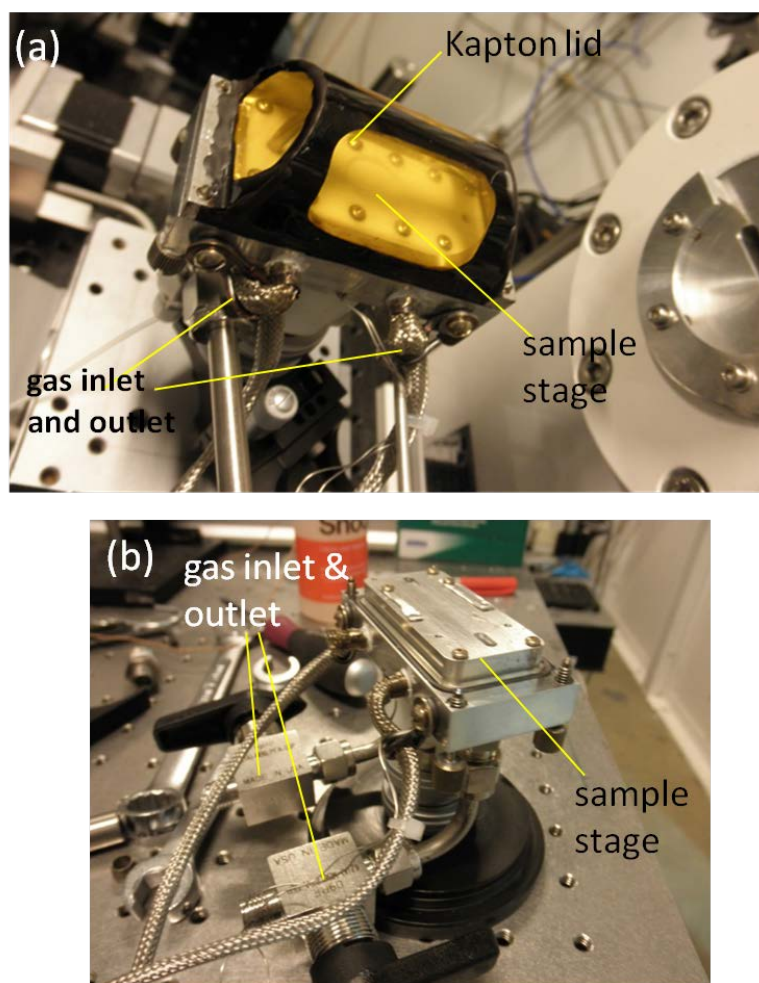


Figure A3: (a) A home-made flow cell suitable for pellet or substrate samples to be measured in fluorescence mode. (b) The sample stage is made of aluminum, with heating units buried under the stage. The maximum temperature that can be reached within this cell is 250 °C.

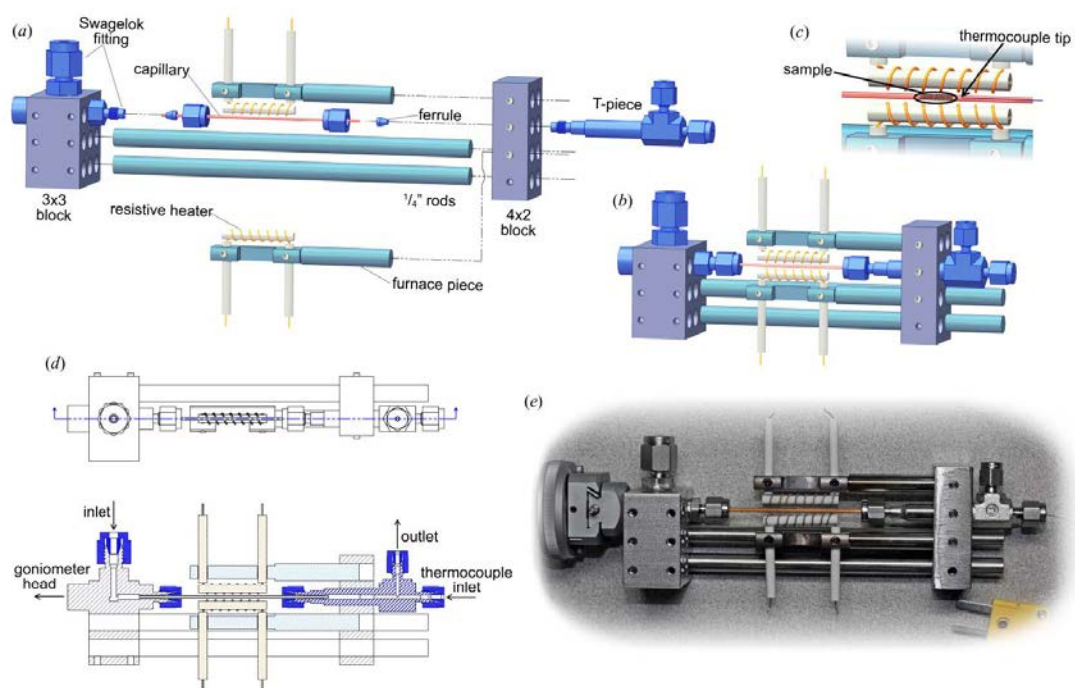


Figure A4: A Kapton flow cell for nonambient X-ray experiments (Source: Ref. [119]). The cell incorporates a furnace which can reach temperatures up to 1000 °C. The compact design and ability of the cell to mount directly on a standard goniometer head allows its use at different beamlines around the APS. The cell can be used for either X-ray diffraction or X-ray absorption measurements.

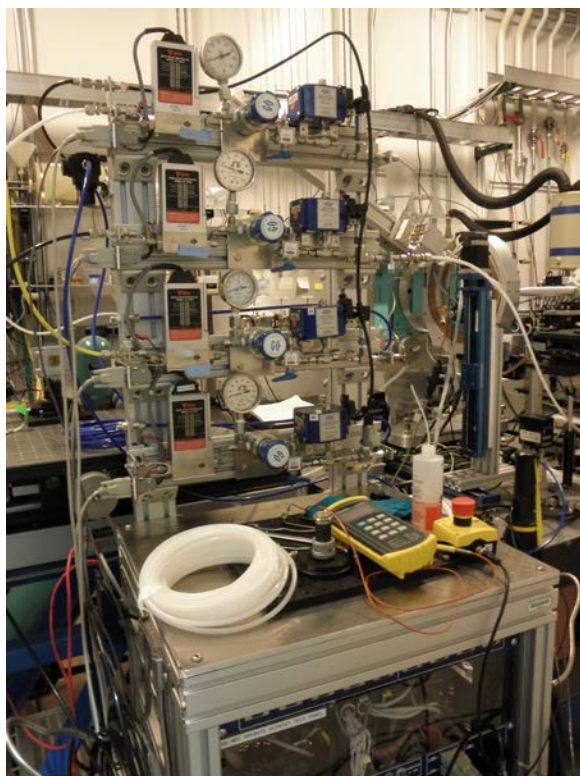


Figure A5: The gas manifold system at 5-BMD. The system has the ability to control the flow rate of reaction gases and to blend up to four different gases.

## Appendix B: Data Analysis and Calculations

### B.1 XRF Determined Pd/Sr Atomic Ratio

The XRF measurements of Pd/STO were performed at beamline 5BM-D at the Advanced Photon Source (APS) of Argonne National Laboratory (ANL). XRF data were collected at an incident photon energy of 24.40 keV by using two Vortex-ME4 four-element silicon drift detectors (SDD) (see Figure A6 for the setup).

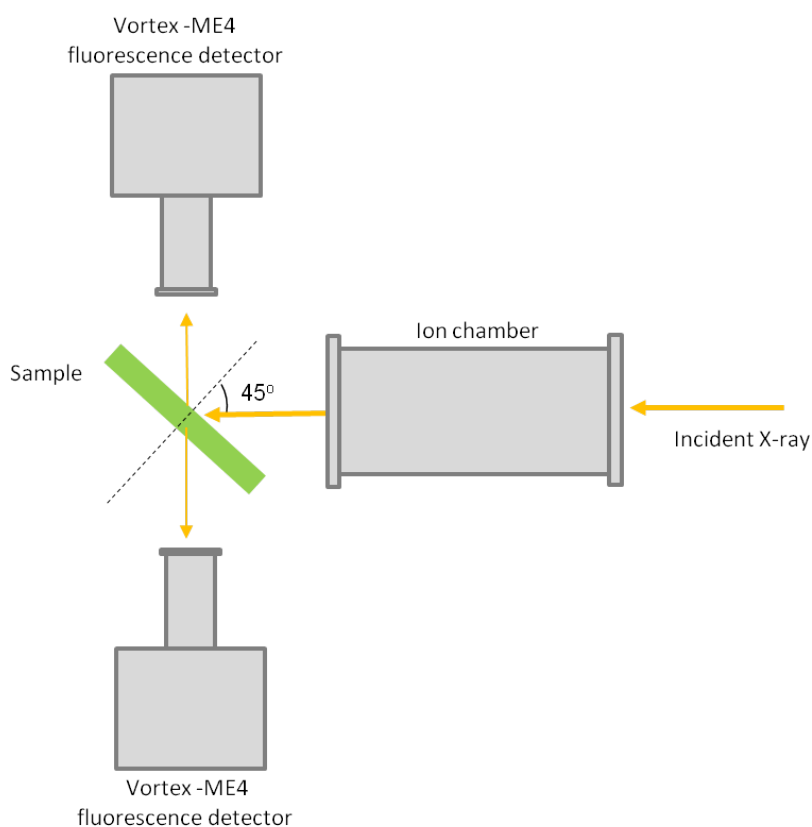


Figure A6: Top view of the XRF measurement setup at beamline 5BM-D of the APS.

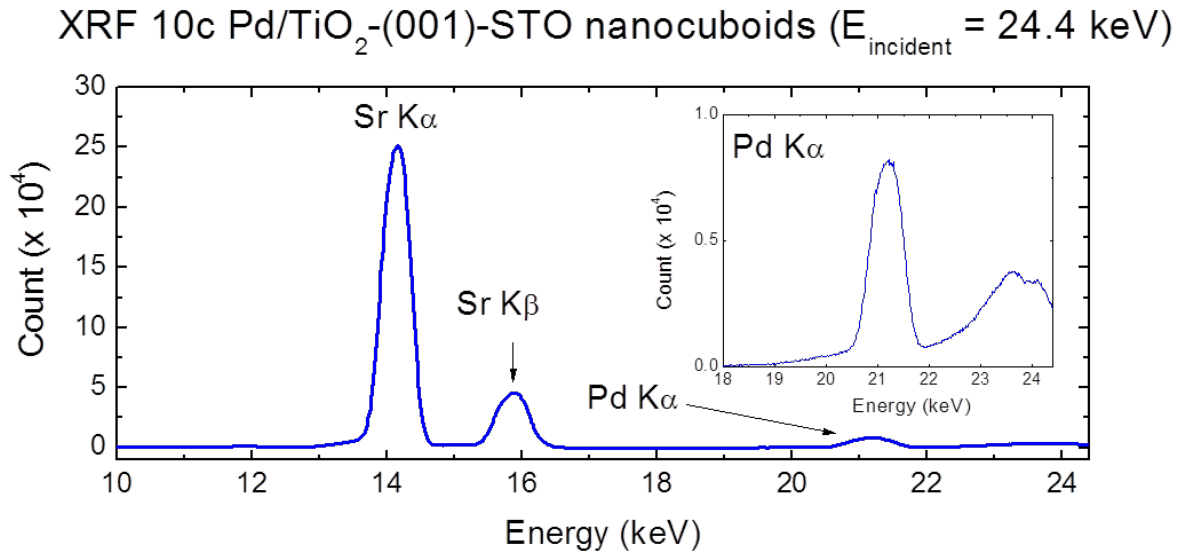


Figure A7: XRF spectra of 10c Pd/TiO<sub>2</sub>-(001)-STO nanocuboids with an incident X-ray energy of 24.40 keV. A 400 micron thick Al filter was in between the sample and detector. The identities of the emission peaks are marked accordingly. XRF collection time was 120 s .

Figure A7 is a typical XRF spectrum for the Pd/STO samples. Atomic ratios of Pd to Sr ( $N_{\text{Pd}}/N_{\text{Sr}}$ ) in the Pd/STO samples were determined by comparing the X-ray fluorescence yields ( $Y_x$ ) of Pd K $\alpha$  (21.18 keV) to Sr K $\alpha$  (14.16 keV) as:

$$\frac{N_{\text{Pd}}}{N_{\text{Sr}}} = \frac{Y_{\text{Pd}}}{Y_{\text{Sr}}} \frac{\sigma_{\text{Sr}}}{\sigma_{\text{Pd}}} \frac{\eta_{\text{Sr}}}{\eta_{\text{Pd}}} \frac{T_{\text{Sr}}}{T_{\text{Pd}}}, \quad (\text{A.1})$$

where  $\sigma_x$  is the XRF cross-section,  $\eta_x$  is the detector efficiency, and  $T_x$  is the transmission factor as the X-ray emission passes from the sample to detector (approximated as 1 in air).  $\sigma$  of Sr K $\alpha$  and Pd K $\alpha$  peaks are  $2.6 \times 10^3$  and  $5.8 \times 10^3$  barns/atom, respectively.  $\sigma$  can be calculated from the XRF\_XSECT program [110]. The efficiency of the Vortex-ME4 Si drift detector is equivalent to the X-ray absorption of the  $t = 0.35 \text{ mm}$  thick Si detector:  $\eta = 1 - e^{-\mu t}$ . Therefore,  $\eta$  is

calculated to be 0.61 for Sr  $K\alpha$  and 0.25 for Pd  $K\alpha$  from the linear absorption coefficients ( $\mu$ ) listed in the CXRO database [154].

X-ray fluorescence yields of Pd  $K\alpha$  and Sr  $K\alpha$  are the background subtracted areas under the corresponding fluorescent peaks. The area under an individual emission peak is obtained by summing up the counts in the channels under the peak, following by subtracting the right trapezoid-shaped background area (assuming a linear background) from the sum, as shown in Figure A8.

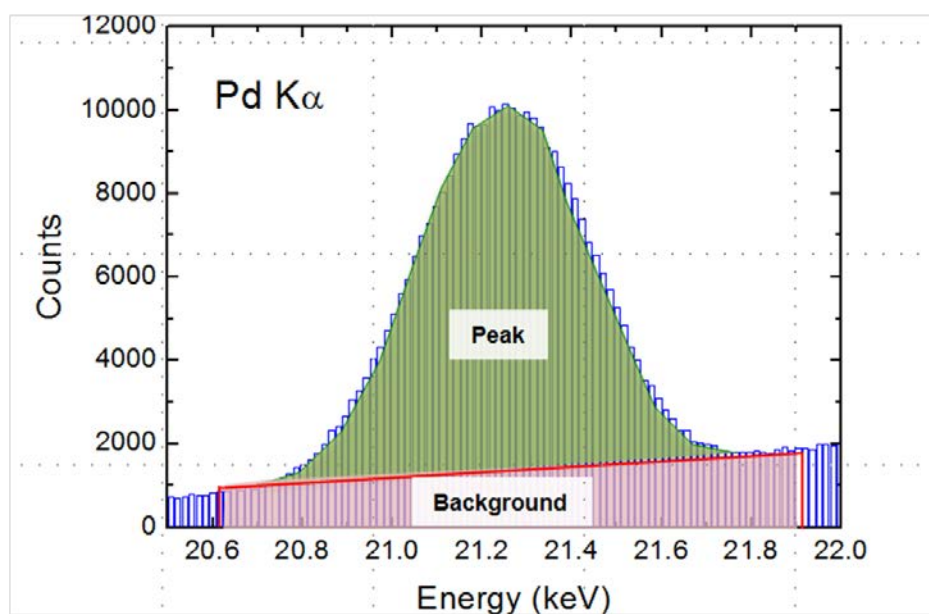


Figure A8: An example of background subtraction for the Pd  $K\alpha$  peak. The area shaded in green and the trapezoid-shaped in red represent the fluorescence yield and background, respectively.

After obtaining  $N_{Pd}/N_{Sr}$  from eq. (A.1), wt% Pd can be calculated from the following equation by assuming stoichiometric STO nanopolyhedra:

$$wt\% \text{ of Pd} = \frac{106.42 \times \frac{N_{Pd}}{N_{Sr}}}{183.49 + 106.42 \times \frac{N_{Pd}}{N_{Sr}}} \times 100\% \quad , \quad (\text{A.2})$$

where 106.42 is atomic mass (g/mol.) of Pd and 183.49 is the molecular mass (g/mol.) of STO.

The coverage (atom/nm<sup>2</sup>) of Pd on STO nanopolyhedra is calculated as:

$$\text{Coverage} = \frac{\frac{N_{Pd}}{N_{Sr}} \times \frac{1}{183.49} \times N_A}{SSA} \quad , \quad (\text{A.3})$$

where  $N_A$  is the Avogadro's number, 183.49 is the molecular mass of STO, and  $A$  is the specific surface area (nm<sup>2</sup>/g) of the STO nanopolyhedra.

## B.2 Pd/STO Surface Composition Determined from XPS

To estimate the amount of the surface F species on the STO nanopolyhedra after Pd ALD deposition, XPS is applied to analyze the atomic ratio of F to surface Sr. The atomic ratio was obtained by analyzing the peak area covered by F 1s and Sr 3d core level photoelectron peaks.

The atomic ratio ( $N_1/N_2$ ) between elements 1 and 2 can be calculated as

$$\frac{N_1}{N_2} = \frac{I_1/S_1}{I_2/S_2} \quad , \quad (\text{A.4})$$

where  $N$  is the number of atoms of the element of interest within the sampling volume,  $I$  is the intensity of the core level peak of interest, and  $S$  is the atomic sensitivity factor\*. The signal of Sr under Pd nanoparticles is attenuated. To calculate the attenuation, it is assumed that the STO surface is covered by an "equivalent Pd coverage," as described in Section 4.3.2. The thickness

of one equivalent Pd layer can be estimated by the height of one Pd atom (0.245 nm)<sup>\*\*</sup>. Based on this estimation, the intensity of Sr ( $I_{Sr}$ ) as it penetrates through the Pd layer can be expressed as:

$$I_{Sr} = I_{Sr^0} e^{-\frac{x}{\lambda}} \quad , \quad (\text{A.5})$$

where  $x$  is the thickness of the equivalent Pd layer,  $\lambda$  is the electron inelastic mean free path (1.67 nm)<sup>\*\*\*</sup> of Sr photoelectron (kinetic energy = 1357 eV) traveling in Pd, and  $I_{Sr^0}$  is the Sr intensity without Pd attenuation.

\* Atomic sensitivity factor of F 1s and Sr 3d were obtained from the database provided in CasaXPS (Source: <http://www.casaxps.com/>).

\*\* Estimated by assuming that every Pd atom occupies a cubic shaped space in a Pd FCC unit cell.  $x = \sqrt[3]{0.389^3/4}$ , where  $x$  is the height of one Pd atom, 0.389 is the lattice constant of Pd (nm), and 4 is the number of Pd atoms in an FCC unit cell.

\*\*\* Obtained from the database of electron inelastic mean free path for elemental solids provided by National Institute for Materials Science (NIMS).

(Source: <https://www.nist.gov/sites/default/files/documents/srd/SRD71UsersGuideV1-2.pdf>)

### B.3 XAS Determined Pd to PdO Ratio

The atomic fraction of Pd in the Pd<sup>0</sup> and Pd<sup>2+</sup> chemical states, namely  $f_{Pd^0}$  and  $f_{Pd^{2+}} = 1 - f_{Pd^0}$ , can be calculated from the linear combination fitting of the XANES and the first shell coordination numbers ( $N$ ) of Pd–Pd and Pd–O bonding fitted from the EXAFS.

#### (a) The XANES method

The XANES spectra of Pd/STO samples were fitted by using the linear combination of standard spectra of Pd<sup>0</sup> (Pd foil) and Pd<sup>2+</sup> (PdO(II), Sigma Alderich) by the ATHENA software.

The edge energies of the XANES spectra were corrected by a standard Pd foil. The fitting range is in between -20 eV to +30 eV from the Pd K-edge position.

(b) The EXAFS method

This simple partitioning between Pd<sup>0</sup> and Pd<sup>2+</sup> is based on our XANES spectra in Figure 4a, which only show Pd<sup>0</sup> and Pd<sup>2+</sup> oxidation states. The EXAFS measured value for  $N$  is the average number of the nearest neighbors from all the individual Pd atoms in the nanoparticle. The  $N_{\text{Pd-Pd}}$  and  $N_{\text{Pd-O}}$  are smaller than their bulk structure counterparts (12 and 4, respectively) due to undercoordination of surface atoms. The ratio between our measured  $N$  and the maximum  $N$  in bulk structures indicates to what degree the Pd is bonded to another atom, either Pd or O. From the argument above, the ratio between  $f_{\text{Pd}^0}$  and  $f_{\text{Pd}^{2+}}$  is equal to the ratio between the measured  $N$  divided by the maximum  $N$  in the bulk structure. The atomic fraction of Pd<sup>0</sup> in each Pd/STO sample can be estimated from  $N_{\text{Pd-Pd}}$  and  $N_{\text{Pd-O}}$  by using the following linear combination relationship:

$$f_{\text{Pd}^0} = \frac{N_{\text{Pd-Pd}}}{12} \bigg/ \left( \frac{N_{\text{Pd-Pd}}}{12} + \frac{N_{\text{Pd-O}}}{4} \right) \quad (\text{A.6})$$

#### B.4 SAXS Determined Pd Interparticle Distance

The positions of interference peaks ( $q_p$ ) in the SAXS profile for Pd NPs on both types of STO nanopolyhedra were determined by the following procedure: The contribution from blank STO nanopolyhedra (0c) was subtracted from the Pd/STO scattering intensity to reveal the interference peak, which was fitted by a Gaussian function on a power-law background, as

shown in Figure A9. The fitted peaks (green) show good agreement with the measured interference peaks (red).

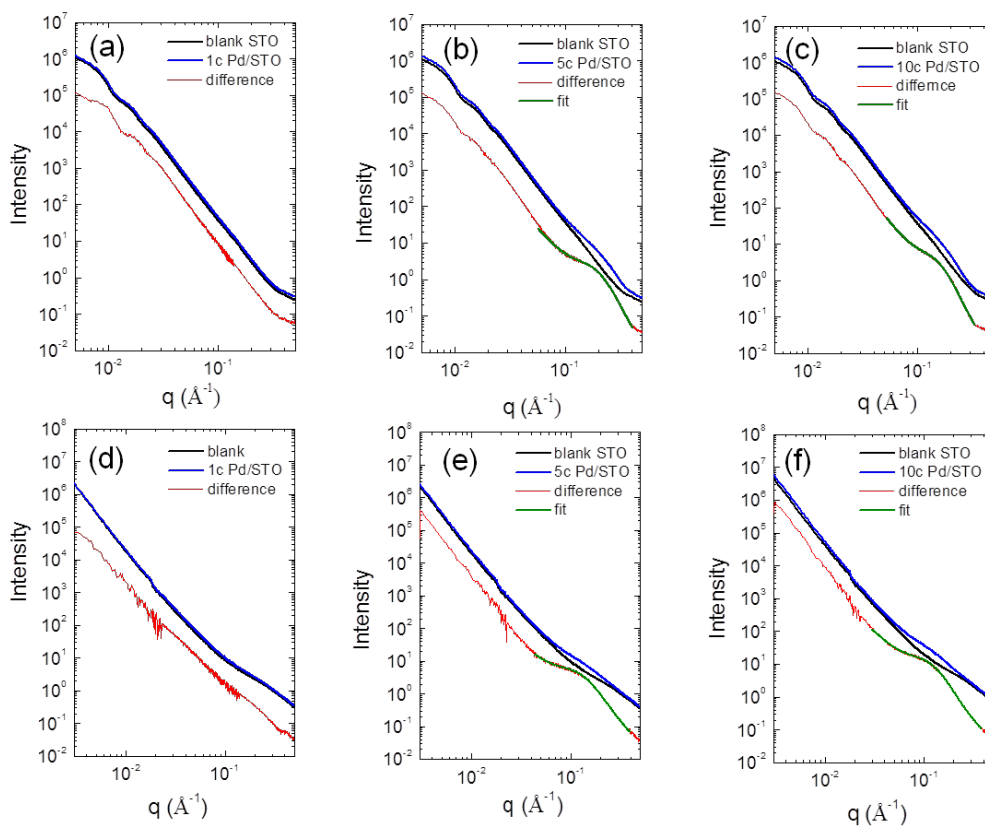


Figure A9: SAXS data analysis of (a) 1c, (b) 5c, (c) 10c Pd supported on  $\text{TiO}_2$ -(001)-STO nanocuboids and (d) 1c, (e) 5c, (f) 10c Pd on (110)-STO nanododecahedra. The interparticle interference peaks (red) are more apparent after subtracting the scattering intensity of blank STO nanopolyhedra (black) from the intensity of Pd/STO samples (blue). The subtracted profiles and fits (green) are shown accordingly in the figure. Meaningful fitting results could not be obtained from the 1c samples due to the low intensity of the interference peaks, as shown in (a) and (d).

The number density (particle/nm<sup>2</sup>) of Pd supported on (110)-STO nanododecahedra was extracted from large representative groups of Pd nanoparticles from multiple TEM images.

Table A1: Number density (particle/nm<sup>2</sup>) of Pd supported on (110)-STO nanododecahedra.

	Number density (particle/nm <sup>2</sup> )
1c Pd/(110)-STO	0.007
5c Pd/(110)-STO	0.019
10c Pd/(110)-STO	0.020

### B.5 Metal Dispersion of Pd Nanoparticles

The metal dispersion (*Disp.*) of ALD-Pd nanoparticles can be obtained from the average Pd diameter by making the assumption on the nature of the crystal planes exposed on the surface [113]. The volume occupied by an atom in the bulk of crystalline metal ( $v_m$ ) is

$$v_m = \frac{M}{\rho N_A} \quad , \quad (\text{A.7})$$

,where  $M$  is the atomic mass,  $\rho$  is the density of the bulk metal, and  $N_A$  is the Avogadro's number. Through equation S5,  $v_m$  for Pd is calculated to be 0.0147 nm<sup>3</sup>/atom. The surface area occupied by an atom ( $a_m$ ) is calculated from the number of atoms per unit surface area in the proportion of certain crystalline planes, depending on the faceting shape of the nanoparticle. Assuming equal amounts of (111) and (001) planes on an FCC Pd nanoparticle,  $a_m$  is 0.0704 nm<sup>2</sup>/atom [113]. Thus, *Disp.* is calculated by further assuming that all of the Pd nanoparticles are

hemispheres with diameter  $d$ . From the information above,  $D$  can be calculated using the following equation:

$$D = \frac{N_S}{N_T} = \frac{\frac{A}{a_m}}{\frac{V}{v_m}} = \frac{6}{d} \left( \frac{v_m}{a_m} \right) \quad (\text{A.8})$$

where  $N_S$  is the number of Pd atoms on the surface,  $N_T$  is the total number of Pd atoms in the nanoparticle.  $A$  and  $V$  are the surface area and volume of a hemisphere with diameter  $d$ , respectively. Figure A10 shows the calculated Pd dispersion as a function of diameter ( $d$ ).

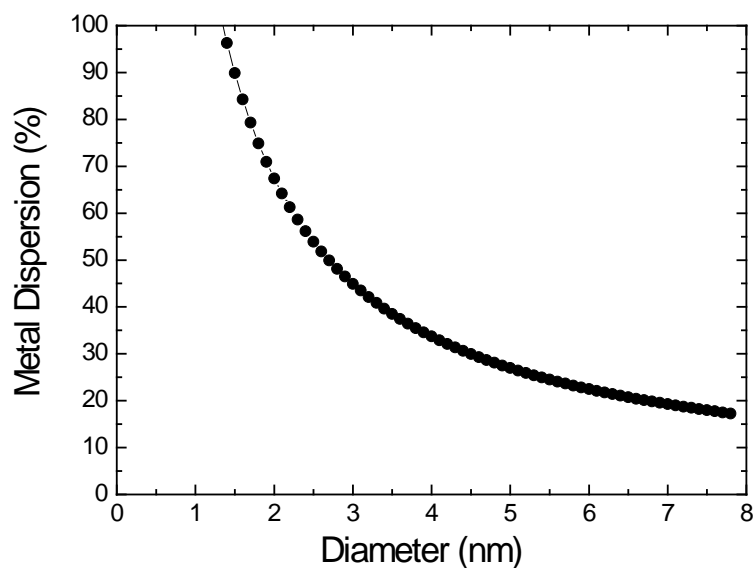


Figure A10: Plot of metal dispersion calculated as a function of Pd diameter, assuming equal amounts of (111) and (001) surface facets.

## B.6 CO Oxidation Turnover Frequency Calculation

TOF was defined as the frequency of CO conversion by surface Pd, in units of  $s^{-1}$ . As shown in Table A2, surface dispersion of Pd can be determined directly from CO pulse chemisorption or calculated from the average diameter and wt% of Pd. Meanwhile, wt% Pd can either be obtained from ICP or XRF. Table A3 compares TOF calculated from three different combinations of characterization methods. The relative trends of TOF between different Pd/STO samples are consistent with each other.

Table A2: The wt% and dispersion of Pd obtained from different characterization techniques.

	ICP wt%	XRF wt%	TEM Dispersion (%) <sup>a</sup>	CO chemisorp. Dispersion (%) <sup>b</sup>
1c/TiO <sub>2</sub> -(001)-STO	0.22	0.26	73.8	84.6
5c/TiO <sub>2</sub> -(001)-STO	1.00	0.99	69.7	-
10c/TiO <sub>2</sub> -(001)-STO	1.20	1.2	48.2	60.8
1c/(110)-STO	0.14	0.17	48.2	72.1
5c/(110)-STO	0.78	0.75	43.2	-
10c/(110)-STO	1.10	0.92	39.2	-

<sup>a</sup> Dispersion estimated by using the average Pd diameter obtained from multiple TEM images.

<sup>b</sup> Some of the CO pulse chemisorption dispersion data were not measured due to limited amount of Pd/STO sample.

Table A3: TOF of Pd/STO samples calculated based on three combinations of characterization methods.

		TOF 80 °C (s <sup>-1</sup> )	TOF 100 °C (s <sup>-1</sup> )	TOF 120 °C (s <sup>-1</sup> )
1c/TiO <sub>2</sub> -(001)-STO	ICP/TEM <sup>a</sup>	2.9×10 <sup>-3</sup>	1.1×10 <sup>-2</sup>	4.1×10 <sup>-2</sup>
	XRF/TEM <sup>b</sup>	2.4×10 <sup>-3</sup>	9.3×10 <sup>-3</sup>	3.4×10 <sup>-2</sup>
	CO chemisorp. <sup>c</sup>	2.1×10 <sup>-3</sup>	8.1×10 <sup>-3</sup>	3.0×10 <sup>-2</sup>
5c/TiO <sub>2</sub> -(001)-STO	ICP/TEM	1.0×10 <sup>-3</sup>	4.9×10 <sup>-3</sup>	3.0×10 <sup>-2</sup>
	XRF/TEM	8.1×10 <sup>-4</sup>	3.8×10 <sup>-3</sup>	2.4×10 <sup>-2</sup>
	CO chemisorp.	-	-	-
10c/TiO <sub>2</sub> -(001)-STO	ICP/TEM	8.5×10 <sup>-4</sup>	4.1×10 <sup>-3</sup>	2.1×10 <sup>-2</sup>
	XRF/TEM	9.3×10 <sup>-4</sup>	4.5×10 <sup>-3</sup>	2.3×10 <sup>-2</sup>
	CO chemisorp.	7.3×10 <sup>-4</sup>	3.5×10 <sup>-3</sup>	1.8×10 <sup>-2</sup>
1c/(110)-STO	ICP/TEM	8.5×10 <sup>-4</sup>	5.1×10 <sup>-3</sup>	2.9×10 <sup>-2</sup>
	XRF/TEM	7.0×10 <sup>-4</sup>	4.2×10 <sup>-3</sup>	2.4×10 <sup>-2</sup>
	CO chemisorp.	3.9×10 <sup>-4</sup>	2.4×10 <sup>-3</sup>	1.3×10 <sup>-2</sup>
5c/(110)-STO	ICP/TEM	9.0×10 <sup>-4</sup>	5.1×10 <sup>-3</sup>	2.8×10 <sup>-2</sup>
	XRF/TEM	9.3×10 <sup>-4</sup>	5.3×10 <sup>-3</sup>	2.9×10 <sup>-2</sup>
	CO chemisorp.	-	-	-
10c/(110)-STO	ICP/TEM	3.8×10 <sup>-4</sup>	1.9×10 <sup>-3</sup>	1.2×10 <sup>-2</sup>
	XRF/TEM	4.4×10 <sup>-4</sup>	2.2×10 <sup>-3</sup>	1.4×10 <sup>-2</sup>
	CO chemisorp.	-	-	-

Number of Pd atoms on the surface determined by:

<sup>a</sup> wt% measured by ICP and dispersion estimated by the average diameter of Pd from TEM

<sup>b</sup> wt% measured by XRF and dispersion estimated by the average diameter of Pd from TEM

<sup>c</sup> CO pulse chemisorption

**REFERENCES**

- [1] S.J. Tauster, Strong metal-support interactions, *Acc. Chem. Res.* 20 (1987) 389–394.  
doi:10.1021/ar00143a001.
- [2] M.G. Willinger, W. Zhang, O. Bondarchuk, S. Shaikhutdinov, H.J. Freund, R. Schlögl, A case of strong metal-support interactions: Combining advanced microscopy and model systems to elucidate the atomic structure of interfaces, *Angew. Chemie - Int. Ed.* 53 (2014) 5998–6001. doi:10.1002/anie.201400290.
- [3] P. Ajayan, L. Marks, Evidence for sinking of small particles into substrates and implications for heterogeneous catalysis, *Nature.* 338 (1989) 139–141.  
doi:10.1038/338139a0.
- [4] L. Marks, P. Ajayan, Equilibrium shape of a buoyant particle, *J. Mater. Res.* 60208 (1990).  
doi:10.1557/JMR.1990.1496.
- [5] Q. Fu, T. Wagner, Interaction of nanostructured metal overlayers with oxide surfaces, *Surf. Sci. Rep.* 62 (2007) 431–498. doi:10.1016/j.surfrep.2007.07.001.
- [6] H.-J. Freund, N. Nilius, T. Risse, S. Schaueremann, A fresh look at an old nano-technology: catalysis, *Phys. Chem. Chem. Phys.* 16 (2014) 8148–8167. doi:10.1039/C3CP55231D.
- [7] M.M. Schubert, S. Hackenberg, A.C. van Veen, M. Muhler, V. Plzak, R.J. Behm, CO

- Oxidation over Supported Gold Catalysts—"Inert" and "Active" Support Materials and Their Role for the Oxygen Supply during Reaction, *J. Catal.* 197 (2001) 113–122. doi:10.1006/jcat.2000.3069.
- [8] D. Widmann, R.J. Behm, Activation of molecular oxygen and the nature of the active oxygen species for co oxidation on oxide supported au catalysts, *Acc. Chem. Res.* 47 (2014) 740–749. doi:10.1021/ar400203e.
- [9] K. An, S. Alayoglu, N. Musselwhite, S. Plamthottam, G. Melaet, A.E. Lindeman, G. a Somorjai, Enhanced CO Oxidation Rates at the Interface of Mesoporous Oxides and Pt Nanoparticles Enhanced CO Oxidation Rates at the Interface of Mesoporous Oxides and Pt Nanoparticles, (2013). doi:10.1021/ja4088743.
- [10] J.A. Enterkin, W. Setthapun, W. Elam, S.T. Christensen, F. a Rabu, L.D. Marks, P.C. Stair, K.R. Poeppelmeier, C.L. Marshall, Propane Oxidation over Pt/SrTiO<sub>3</sub> Nanocuboids, *ACS Catal.* 1 (2011) 629. doi:10.1021/cs200092c.
- [11] E.J. Peterson, A.T. DeLaRiva, S. Lin, R.S. Johnson, H. Guo, J.T. Miller, J. Hun Kwak, C.H.F. Peden, B. Kiefer, L.F. Allard, F.H. Ribeiro, A.K. Datye, Low-temperature carbon monoxide oxidation catalysed by regenerable atomically dispersed palladium on alumina., *Nat. Commun.* 5 (2014) 4885. doi:10.1038/ncomms5885.

- [12] G. Ertl, Elementary Steps in Heterogeneous Catalysis, *Angew. Chemie Int. Ed. English*. 29 (1990) 1219–1227. doi:10.1002/anie.199012191.
- [13] D.W. Goodman, Catalysis: from single crystals to the “real world,” *Surf. Sci.* 299–300 (1994) 837–848. doi:10.1016/0039-6028(94)90701-3.
- [14] D.W. Goodman, Correlations between Surface Science Models and “Real-World” Catalysts, *J. Phys. Chem.* 100 (1996) 13090–13102. doi:10.1021/jp953755e.
- [15] C.T. Campbell, Ultrathin metal films and particles on oxide surfaces: structural, electronic and chemisorptive properties, *Surf. Sci. Rep.* 27 (1997) 1–111. doi:10.1016/S0167-5729(96)00011-8.
- [16] C.R. Henry, Surface studies of supported model catalysts, *Surf. Sci. Rep.* 31 (1998) 231–325. doi:10.1016/S0167-5729(98)00002-8.
- [17] M. Bäumer, H.-J. Freund, Metal deposits on well-ordered oxide films, *Prog. Surf. Sci.* 61 (1999) 127–198. doi:10.1016/S0079-6816(99)00012-X.
- [18] T.P.S. Clair, D.W. Goodman, Metal nanoclusters supported on metal oxide thin films : bridging the materials gap, *Top. Catal.* 13 (2000) 5–19. doi:10.1023/A:1009020502894.
- [19] H.J. Freund, H. Kühlenbeck, J. Libuda, G. Rupprechter, M. Baumer, H. Hamann, Bridging the pressure and materials gaps between catalysis and surface science: clean and modified

- oxide surfaces, *Top. Catal.* 15 (2001) 201–209. doi:10.1023/A:1016686322301.
- [20] G.A. Somorjai, K.R. McCrea, J. Zhu, Active sites in heterogeneous catalysis: Development of molecular concepts and future challenges, *Top. Catal.* 18 (2002) 157–166. doi:10.1023/A:1013874202404.
- [21] G.A. Somorjai, R.L. York, D. Butcher, J.Y. Park, The evolution of model catalytic systems ; studies of structure , bonding and dynamics from single crystal metal surfaces to nanoparticles , and from low pressure ( $<10^{-3}$  Torr ) to high pressure ( $>10^{-3}$  Torr ) to liquid interfaces, *Phys. Chem. Chem. Phys.* 9 (2007) 3500–3513. doi:10.1039/b618805b.
- [22] F. Gao, D.W. Goodman, Model Catalysts: Simulating the Complexities of Heterogeneous Catalysts, *Annu. Rev. Phys. Chem.* 63 (2012) 265–286. doi:10.1146/annurev-physchem-032511-143722.
- [23] H.J. Freund, Models for heterogeneous catalysts: studies at the atomic level, *Rend. Lincei.* (2016). doi:10.1007/s12210-016-0560-4.
- [24] S.T. Christensen, J.W. Elam, F.A. Rabuffetti, Q. Ma, S.J. Weigand, B. Lee, S. Seifert, P.C. Stair, K.R. Poepelmeier, M.C. Hersam, M.J. Bedzyk, Controlled growth of platinum nanoparticles on strontium titanate nanocubes by atomic layer deposition, *Small.* 5 (2009) 750–757. doi:10.1002/sml.200801920.

- [25] J.A. Enterkin, R.M. Kennedy, J. Lu, J.W. Elam, R.E. Cook, L.D. Marks, P.C. Stair, C.L. Marshall, K.R. Poeppelmeier, Epitaxial stabilization of face selective catalysts, *Top. Catal.* 56 (2013) 1829–1834. doi:10.1007/s11244-013-0118-y.
- [26] C. Wang, *Atomically-Precise Synthesis and Design of Platinum catalysts on Strontium Titanate using Atomic Layer Deposition*, Northwestern University, 2014.
- [27] R.G. Carr, G.A. Somorjai, Hydrogen production from photolysis of steam adsorbed onto platinumized SrTiO<sub>3</sub>, *Nature*. 290 (1981) 576–577. doi:10.1038/290576a0.
- [28] A.D. Polli, T. Wagner, T. Gemming, M. Rühle, Growth of platinum on TiO<sub>2</sub>- and SrO-terminated SrTiO<sub>3</sub>(100), *Surf. Sci.* 448 (2000) 279–289. doi:10.1016/S0039-6028(99)01233-9.
- [29] H. Iddir, V. Komanicky, S. Ogut, H. You, P. Zapol, Shape of platinum nanoparticles supported on SrTiO<sub>3</sub>: Experiment and theory, *J. Phys. Chem. C*. 111 (2007) 14782–14789. doi:10.1021/jp073041r.
- [30] V. Komanicky, H. Iddir, K.C. Chang, A. Menzel, G. Karapetrov, D. Hennessy, P. Zapol, H. You, Shape-dependent activity of platinum array catalyst, *J. Am. Chem. Soc.* 131 (2009) 5732–5733. doi:10.1021/ja900459w.
- [31] S.T. Christensen, J.W. Elam, B. Lee, Z. Feng, M.J. Bedzyk, M.C. Hersam, *Nanoscale*

- Structure and Morphology of Atomic Layer Deposition Platinum on SrTiO<sub>3</sub> (001), *Chem. Mater.* 21 (2009) 516–521. doi:10.1021/cm8026863.
- [32] S.T. Christensen, B. Lee, Z. Feng, M.C. Hersam, M.J. Bedzyk, Hierarchical nanoparticle morphology for platinum supported on SrTiO<sub>3</sub> (0 0 1): A combined microscopy and X-ray scattering study, *Appl. Surf. Sci.* 256 (2009) 423–427. doi:10.1016/j.apsusc.2009.06.017.
- [33] Z. Feng, S.T. Christensen, J.W. Elam, B. Lee, M.C. Hersam, M.J. Bedzyk, Thermally induced nanoscale structural and morphological changes for atomic-layer-deposited Pt on SrTiO<sub>3</sub>(001), *J. Appl. Phys.* 110 (2011) 1–8. doi:10.1063/1.3661163.
- [34] Z. Feng, A. Kazimirov, M.J. Bedzyk, Atomic imaging of oxide-supported metallic nanocrystals, *ACS Nano.* 5 (2011) 9755–9760. doi:10.1021/nn203273e.
- [35] S.E. Stoltz, D.E. Ellis, M.J. Bedzyk, Interface of Pt with SrTiO<sub>3</sub>(001): A combined theoretical and experimental study, *Surf. Sci.* 633 (2015) 8–16. doi:10.1016/j.susc.2014.11.011.
- [36] T. Wagner, G. Richter, M. Rühle, Epitaxy of Pd thin films on (100) SrTiO<sub>3</sub>: A three-step growth process, *J. Appl. Phys.* 89 (2001) 2606–2612. doi:10.1063/1.1338987.
- [37] F. Silly, A.C. Powell, M.G. Martin, M.R. Castell, Growth shapes of supported Pd nanocrystals on SrTiO<sub>3</sub>(001), *Phys. Rev. B - Condens. Matter Mater. Phys.* 72 (2005) 1–6.

- doi:10.1103/PhysRevB.72.165403.
- [38] F. Silly, M.R. Castell, Selecting the shape of supported metal nanocrystals: Pd Huts, hexagons, or pyramids on SrTiO<sub>3</sub>(001), *Phys. Rev. Lett.* 94 (2005) 3–6.  
doi:10.1103/PhysRevLett.94.046103.
- [39] W.L. Winterbottom, Equilibrium shape of a small particle in contact with a foreign substrate, *Acta Metall.* 15 (1967) 303–310. doi:10.1016/0001-6160(67)90206-4.
- [40] B.R. Chen, C. George, Y. Lin, L. Hu, L. Crosby, X. Hu, P.C. Stair, L.D. Marks, K.R. Poepelmeier, R.P. Van Duyne, M.J. Bedzyk, Morphology and oxidation state of ALD-grown Pd nanoparticles on TiO<sub>2</sub>- and SrO-terminated SrTiO<sub>3</sub> nanocuboids, *Surf. Sci.* 648 (2016) 291–298. doi:10.1016/j.susc.2015.10.057.
- [41] F.A. Rabuffetti, H.S. Kim, J.A. Enterkin, Y. Wang, C.H. Lanier, L.D. Marks, K.R. Poepelmeier, P.C. Stair, Synthesis-dependent first-order Raman scattering in SrTiO<sub>3</sub> nanocubes at room temperature, *Chem. Mater.* 20 (2008) 5628–5635.  
doi:10.1021/cm801192t.
- [42] F.A. Rabuffetti, P.C. Stair, K.R. Poepelmeier, Synthesis-dependent surface acidity and structure of SrTiO<sub>3</sub> nanoparticles, *J. Phys. Chem. C.* 114 (2010) 11056–11067.  
doi:10.1021/jp101727c.

- [43] L. Hu, C. Wang, S. Lee, R.E. Winans, L.D. Marks, K.R. Poeppelmeier, SrTiO<sub>3</sub>Nanocuboids from a Lamellar Microemulsion, *Chem. Mater.* 25 (2013) 378–384. doi:10.1021/cm303303x.
- [44] L. Hu, C. Wang, R.M. Kennedy, L.D. Marks, R. Kenneth, The Role of Oleic Acid : From Synthesis to Assembly of Perovskite Nanocuboid Two-dimensional Arrays, (2014) 1–2.
- [45] L.A. Crosby, R.M. Kennedy, B.-R. Chen, J. Wen, K.R. Poeppelmeier, M.J. Bedzyk, L.D. Marks, Complex surface structure of (110) terminated strontium titanate nanododecahedra, *Nanoscale.* 8 (2016) 16606–16611. doi:10.1039/C6NR05516H.
- [46] C. Wang, L. Hu, K. Poeppelmeier, P.C. Stair, L. Marks, Nucleation and Growth Process of Atomic Layer Deposition Platinum Nanoparticles on Strontium Titanate Nanocuboids, *Nanotechnology.* (2017) In Press.
- [47] Y. Kang, M. Li, Y. Cai, M. Cargnello, R.E. Diaz, T.R. Gordon, N.L. Wieder, R.R. Adzic, R.J. Gorte, E.A. Stach, C.B. Murray, Heterogeneous catalysts need not Be so “heterogeneous”: Monodisperse Pt nanocrystals by combining shape-controlled synthesis and purification by colloidal recrystallization, *J. Am. Chem. Soc.* 135 (2013) 2741–2747. doi:10.1021/ja3116839.
- [48] X. Liu, R. Wang, L. Song, H. He, G. Zhang, X. Zi, W. Qiu, The oxidation of carbon

- monoxide over the palladium nanocube catalysts: Effect of the basic-property of the support, *Catal. Commun.* 46 (2014) 213–218. doi:10.1016/j.catcom.2013.12.003.
- [49] K.J. Laidler, A. Cornish-bowden, Elizabeth Fulhame and the Discovery of Catalysis: 100 Years Before Buchner, in: A. Cornish-Bowden (Ed.), *New Beer an Old Bottle Eduard Buchner Growth Biochem. Knowl.*, Universitat de València, 1997: pp. 123–126.
- [50] X. Lim, The new breed of cutting-edge catalysts, *Nature.* 537 (2016) 156–158. doi:10.1038/537156a.
- [51] E. Fulhame, *An essay on combustion, with a view to a new art of dying and painting: wherein the phlogistic and antiphlogistic hypotheses are proved erroneous*, Printed for the author, by J. Cooper, London, 1794.
- [52] B. Lindström, L.J. Pettersson, A brief history of catalysis, *Cattech.* 7 (2003) 130–138. doi:10.1023/A:1025001809516.
- [53] A.J.B. Robertson, The Early History of Catalysis, *Platin. Met. Rev.* 19 (1975) 64–69. doi:10.1007/BF03214875.
- [54] F. Bozso, G. Ertl, M. Weiss, Interaction of nitrogen with iron surfaces I. Fe(100) and Fe(111), *J. Catal.* 49 (1977) 18–41. doi:10.1016/0021-9517(77)90237-8.
- [55] G. Ertl, Primary steps in catalytic synthesis of ammonia, *J. Vac. Sci. Technol. A Vacuum*,

- Surfaces, Film. 1 (1983) 1247–1253. doi:10.1116/1.572299.
- [56] J.W. Erisman, M.A. Sutton, J. Galloway, Z. Klimont, W. Winiwarter, How a century of ammonia synthesis changed the world, *Nat. Geosci.* 1 (2008) 636–639. doi:10.1038/ngeo325.
- [57] G. Ertl, Reactions at surfaces: From atoms to complexity (nobel lecture), *Angew. Chemie - Int. Ed.* 47 (2008) 3524–3535. doi:10.1002/anie.200800480.
- [58] J.N. Armor, A history of industrial catalysis, *Catal. Today.* 163 (2011) 3–9. doi:10.1016/j.cattod.2009.11.019.
- [59] M.E. Davis, R.J. Davis, Heterogeneous Catalysis, *Fundam. Chem. React. Eng.* 4 (2012) 133–183. doi:10.1074/jbc.M111.287409.
- [60] Wikipedia: Catalytic Converter, (n.d.). [https://en.wikipedia.org/wiki/Catalytic\\_converter](https://en.wikipedia.org/wiki/Catalytic_converter).
- [61] Platinum group metal recovery from spent catalytic-converters using xrf, (n.d.). <https://www.thermofisher.com/blog/metals/platinum-group-metal-recovery-from-spent-catalytic-converters-using-xrf/>.
- [62] Precious Metals & Currency Rates history, (2016). <https://www.catalyticconverterrecycling.com/metals> (accessed January 1, 2016).
- [63] P. Munnik, P.E. De Jongh, K.P. De Jong, Recent Developments in the Synthesis of

- Supported Catalysts, *Chem. Rev.* 115 (2015) 6687–6718. doi:10.1021/cr500486u.
- [64] Z. Ma, F. Zaera, Heterogeneous Catalysis by Metals. *Encyclopedia of Inorganic Chemistry*, *Encycl. Inorg. Bioinorg. Chem.* (2011) 1–17. doi:10.1002/9781119951438.eibc0079.pub2.
- [65] Y. Lin, Z. Wu, J. Wen, K. Ding, X. Yang, K.R. Poeppelmeier, L.D. Marks, Adhesion and Atomic Structures of Gold on Ceria Nanostructures: The Role of Surface Structure and Oxidation State of Ceria Supports, *Nano Lett.* 15 (2015) 5375–5381. doi:10.1021/acs.nanolett.5b02694.
- [66] Z. Wu, S.H. Overbury, *Catalysis by Materials with Well-Defined Structures*, Elsevier, 2015.
- [67] N. Lopez, T.V.W. Janssens, B.S. Clausen, Y. Xu, M. Mavrikakis, T. Bligaard, J.K. Nørskov, On the origin of the catalytic activity of gold nanoparticles for low-temperature CO oxidation, *J. Catal.* 223 (2004) 232–235. doi:10.1016/j.jcat.2004.01.001.
- [68] B.R. Cuenya, Synthesis and catalytic properties of metal nanoparticles: Size, shape, support, composition, and oxidation state effects, *Thin Solid Films.* 518 (2010) 3127–3150. doi:10.1016/j.tsf.2010.01.018.
- [69] J.A. Enterkin, K.R. Poeppelmeier, L.D. Marks, Oriented catalytic platinum nanoparticles

- on high surface area strontium titanate nanocuboids, *Nano Lett.* 11 (2011) 993–997.  
doi:10.1021/nl104263j.
- [70] Y. Lin, J. Wen, L. Hu, R.M. Kennedy, P.C. Stair, K.R. Poeppelmeier, L.D. Marks, Synthesis-dependent atomic surface structures of oxide nanoparticles, *Phys. Rev. Lett.* 111 (2013) 1–5. doi:10.1103/PhysRevLett.111.156101.
- [71] K. Eisenbeiser, J.M. Finder, Z. Yu, J. Ramdani, J.A. Curless, J.A. Hallmark, R. Droopad, W.J. Ooms, L. Salem, S. Bradshaw, C.D. Overgaard, Field effect transistors with SrTiO<sub>3</sub> gate dielectric on Si, *Appl. Phys. Lett.* 76 (2000) 1324–1326. doi:10.1063/1.126023.
- [72] P. Ye, J. Gu, Y. Wu, M. Xu, Y. Xuan, T. Shen, A. Neal, (Invited) ALD High-k as a Common Gate Stack Solution for Nanoelectronics, in: 2010: pp. 51–68.  
doi:10.1149/1.3372563.
- [73] D.J. Werder, C.H. Chen, H.L. Kao, J. Kwo, Microstructures of thin film La<sub>2-x</sub>Sr<sub>x</sub>CuO<sub>4</sub> on SrTiO<sub>3</sub> and LaAlO<sub>3</sub>, *Phys. C Supercond.* 204 (1992) 155–160.  
doi:10.1016/0921-4534(92)90585-Z.
- [74] F.T. Wagner, G.A. Somorjai, Photocatalytic hydrogen production from water on Pt-free SrTiO<sub>3</sub> in alkali hydroxide solutions, *Nature.* 285 (1980) 559–560. doi:10.1038/285559a0.
- [75] F.T. Wagner, G.A. Somorjai, Photocatalytic and photoelectrochemical hydrogen

- production on strontium titanate single crystals, *J. Am. Chem. Soc.* 102 (1980) 5494–5502.  
doi:10.1021/ja00537a013.
- [76] J.C. Hemminger, R. Carr, G.A. Somorjai, The photoassisted reaction of gaseous water and carbon dioxide adsorbed on the SrTiO<sub>3</sub> (111) crystal face to form methane, *Chem. Phys. Lett.* 57 (1978) 100–104. doi:10.1016/0009-2614(78)80359-5.
- [77] B. Aurian-Blajeni, M. Halmann, J. Manassen, Photoreduction of carbon dioxide and water into formaldehyde and methanol on semiconductor materials, *Sol. Energy.* 25 (1980) 165–170. doi:10.1016/0038-092X(80)90472-7.
- [78] J. a Enterkin, A.K. Subramanian, B.C. Russell, M.R. Castell, K.R. Poeppelmeier, L.D. Marks, A homologous series of structures on the surface of SrTiO<sub>3</sub>(110)., *Nat. Mater.* 9 (2010) 245–248. doi:10.1038/nmat2636.
- [79] B.C. Russell, M.R. Castell, Reconstructions on the polar SrTiO<sub>3</sub> (110) surface: Analysis using STM, LEED, and AES, *Phys. Rev. B.* 77 (2008) 245414.  
doi:10.1103/PhysRevB.77.245414.
- [80] E. Heifets, W.A. Goddard, E.A. Kotomin, R.I. Eglitis, G. Borstel, Ab initio calculations of the SrTiO<sub>3</sub>(110) polar surface, *Phys. Rev. B.* 69 (2004) 35408.  
doi:10.1103/PhysRevB.69.035408.

- [81] U. Diebold, Oxide surfaces: Surface science goes inorganic., *Nat. Mater.* 9 (2010) 185–187. doi:10.1038/nmat2708.
- [82] Z. Wang, F. Yang, Z. Zhang, Y. Tang, J. Feng, K. Wu, Q. Guo, J. Guo, Evolution of the surface structures on SrTiO<sub>3</sub>(110) tuned by Ti or Sr concentration, *Phys. Rev. B - Condens. Matter Mater. Phys.* 83 (2011) 1–9. doi:10.1103/PhysRevB.83.155453.
- [83] Z. Li, J. Zhu, C. Wu, Z. Tang, Y. Kawazoe, Relaxations of TiO<sub>2</sub>- and SrO-terminated SrTiO<sub>3</sub> (001) surfaces, *Phys. Rev. B.* 58 (1998) 8075–8078. [http://prb.aps.org/abstract/PRB/v58/i12/p8075\\_1](http://prb.aps.org/abstract/PRB/v58/i12/p8075_1).
- [84] A. Biswas, P.B. Rossen, C.H. Yang, W. Siemons, M.H. Jung, I.K. Yang, R. Ramesh, Y.H. Jeong, Universal Ti-rich termination of atomically flat SrTiO<sub>3</sub> (001), (110), and (111) surfaces, *Appl. Phys. Lett.* 98 (2011). doi:10.1063/1.3549860.
- [85] A. Hirata, K. Saiki, A. Koma, A. Ando, Electronic structure of a SrO-terminated SrTiO<sub>3</sub>(100) surface, *Surf. Sci.* 319 (1994) 267–271. doi:10.1016/0039-6028(94)90593-2.
- [86] C. Raisch, T. Chassé, C. Langheinrich, A. Chassé, Preparation and investigation of the A-site and B-site terminated SrTiO<sub>3</sub>(001) surface: A combined experimental and theoretical x-ray photoelectron diffraction study, *J. Appl. Phys.* 112 (2012). doi:10.1063/1.4757283.

- [87] S.E. Stoltz, D.E. Ellis, M.J. Bedzyk, Structure and reactivity of zero-, two- and three-dimensional Pd supported on SrTiO<sub>3</sub>(001), *Surf. Sci.* 630 (2014) 46–63. doi:10.1016/j.susc.2014.06.018.
- [88] J. Lu, J.W. Elam, P.C. Stair, Atomic layer deposition - Sequential self-limiting surface reactions for advanced catalyst “bottom-up” synthesis, *Surf. Sci. Rep.* 71 (2016) 410–472. doi:10.1016/j.surfrep.2016.03.003.
- [89] J.W. Elam, A. Zinovev, C.Y. Han, H.H. Wang, U. Welp, J.N. Hryn, M.J. Pellin, Atomic layer deposition of palladium films on Al<sub>2</sub>O<sub>3</sub> surfaces, *Thin Solid Films.* 515 (2006) 1664–1673. doi:10.1016/j.tsf.2006.05.049.
- [90] Y. Lei, B. Liu, J. Lu, R.J. Lobo-lapidus, T. Wu, H. Feng, X. Xia, A.U. Mane, J. a Libera, P. Greeley, T. Miller, W. Elam, Synthesis of Pt – Pd Core – Shell Nanostructures by Atomic Layer Deposition: Application in Propane Oxidative Dehydrogenation to Propylene, *Chemistry (Easton).* 24 (2012) 3525–3533. doi:10.1021/cm300080w.
- [91] A.J.M. Mackus, M.J. Weber, N.F.W. Thissen, D. Garcia-Alonso, R.H.J. Vervuurt, S. Assali, A.A. Bol, M.A. Verheijen, W.M.M. Kessels, Atomic layer deposition of Pd and Pt nanoparticles for catalysis: on the mechanisms of nanoparticle formation., *Nanotechnology.* 27 (2016) 34001. doi:10.1088/0957-4484/27/3/034001.

- [92] W.D. Kaplan, D. Chatain, P. Wynblatt, W.C. Carter, A review of wetting versus adsorption, complexions, and related phenomena: The rosetta stone of wetting, *J. Mater. Sci.* 48 (2013) 5681–5717. doi:10.1007/s10853-013-7462-y.
- [93] L.D. Marks, L. Peng, Nanoparticle shape, thermodynamics and kinetics, *J. Phys. Condens. Matter.* 28 (2016) 53001. doi:10.1088/0953-8984/28/5/053001.
- [94] K. Hansen, T. Worren, S. Stempel, E. Lægsgaard, M. Bäumer, H.-J. Freund, F. Besenbacher, I. Stensgaard, Palladium Nanocrystals on Al<sub>2</sub>O<sub>3</sub>: Structure and Adhesion Energy, *Phys. Rev. Lett.* 83 (1999) 4120–4123. doi:10.1103/PhysRevLett.83.4120.
- [95] R. V. Zucker, D. Chatain, U. Dahmen, S. Hagège, W.C. Carter, New software tools for the calculation and display of isolated and attached interfacial-energy minimizing particle shapes, *J. Mater. Sci.* 47 (2012) 8290–8302. doi:10.1007/s10853-012-6739-x.
- [96] M. Methfessel, D. Hennig, M. Scheffler, Trends of the surface relaxations, surface energies, and work functions of the 4d transition metals, *Phys. Rev. B.* 46 (1992) 4816–4829. doi:10.1103/PhysRevB.46.4816.
- [97] H.J. Freund, G. Meijer, M. Scheffler, R. Schlögl, M. Wolf, CO oxidation as a prototypical reaction for heterogeneous processes, *Angew. Chemie - Int. Ed.* 50 (2011) 10064–10094. doi:10.1002/anie.201101378.

- [98] G. Ertl, P.R. Norton, J. Rüstig, Kinetic Oscillations in the Platinum-Catalysed Oxidation of CO, *Phys. Rev. Lett.* 49 (1982) 177–180.
- [99] T. Engel, G. Ertl, H.P. D.D. Eley, B.W. Paul, Elementary Steps in the Catalytic Oxidation of Carbon Monoxide on Platinum Metals, *Adv. Catal. Volume 28* (1979) 1–78.
- [100] P.J. Berlowitz, C.H.F. Peden, D.W. Goodman, Kinetics of CO Oxidation on Single-Crystal Pd, Pt, and Ir, *J. Phys. Chem.* 92 (1988) 5213–5221. doi:10.1021/j100329a030.
- [101] S. Kunz, F.F. Schweinberger, V. Habibpour, M. Röttgen, C. Harding, M. Arenz, U. Heiz, Temperature dependent CO oxidation mechanisms on size-selected clusters, *J. Phys. Chem. C.* 114 (2010) 1651–1654. doi:10.1021/jp911269z.
- [102] R. Wang, H. He, L.-C. Liu, H.-X. Dai, Z. Zhao, Shape-dependent catalytic activity of palladium nanocrystals for the oxidation of carbon monoxide, *Catal. Sci. Technol.* 2 (2012) 575. doi:10.1039/c2cy00417h.
- [103] K. Byrappa, M. Yoshimura, *Handbook of Hydrothermal Technology: A Technology for Crystal Growth and Materials Processing*, Elsevier, n.d.
- [104] C. Friderichs, N. Zotov, W. Mader, Synthesis of monodisperse  $\text{SrTi}_{1-x}\text{Zr}_x\text{O}_3$  nanocubes in oleate by a two-phase solvothermal method, *Eur. J. Inorg. Chem.* 2015 (2015) 288–295. doi:10.1002/ejic.201402724.

- [105] D.I. Svergun, M.H.J. Koch, Small-angle scattering studies of biological macromolecules in solution, *Reports Prog. Phys.* 66 (2003) 1735–1782. doi:10.1088/0034-4885/66/10/R05.
- [106] J. Als-Nielsen, D. McMorrow, *Elements of Modern X-ray Physics*, 2nd Editio, Wiley, 2011.
- [107] J. Ilavsky, P.R. Jemian, Irena: tool suite for modeling and analysis of small-angle scattering, *J. Appl. Crystallogr.* 42 (2009) 347–353. doi:10.1107/S0021889809002222.
- [108] S.R. Kline, Reduction and analysis of SANS and USANS data using IGOR Pro, *J. Appl. Crystallogr.* 39 (2006) 895–900. doi:10.1107/S0021889806035059.
- [109] A.C.. Thompson, D. Vaughan, *X-ray Data Booklet*, 2nd ed., Lawrence Berkeley National Laboratory, 2009.
- [110] J.A. Klug, *Synchrotron X-ray Studies of Epitaxial Ferroelectric Thin Films and Nanostructures*, Northwestern University, 2010.
- [111] M.B. Mitchell, Fundamentals and Applications of Diffuse Reflectance Infrared Fourier Transform (DRIFT) Spectroscopy, in: *Struct. Relations Polym.*, 1993: pp. 351–375. doi:10.1021/ba-1993-0236.ch013.
- [112] T. Armaroli, T. Bécue, S. Gautier, Diffuse Reflection Infrared Spectroscopy (Drifts): Application to the in Situ Analysis of Catalysts, *Oil Gas Sci. Technol.* 59 (2004) 215–237.

- doi:10.2516/ogst:2004016.
- [113] P. Canton, G. Fagherazzi, M. Battagliarin, F. Menegazzo, F. Pinna, N. Pernicone, Pd/ CO Average Chemisorption Stoichiometry in Highly Dispersed Supported Pd /  $\gamma$ -Al<sub>2</sub>O<sub>3</sub> Catalysts, *Langmuir*. 18 (2002) 6530–6535.
- [114] G.C. Bond, *Small Particles of the Platinum Metals*, (1975) 126–134.
- [115] M. Boudart, Turnover Rates in Heterogeneous Catalysis, *Chem. Rev.* 95 (1995) 661–666.  
doi:10.1021/cr00035a009.
- [116] J.W. Elam, M.D. Groner, S.M. George, Viscous flow reactor with quartz crystal microbalance for thin film growth by atomic layer deposition, *Rev. Sci. Instrum.* 73 (2002) 2981–2987. doi:10.1063/1.1490410.
- [117] C.A. Schneider, W.S. Rasband, K.W. Eliceiri, NIH Image to ImageJ: 25 years of image analysis, *Nat. Methods*. 9 (2012) 671–675. doi:10.1038/nmeth.2089.
- [118] B. Ravel, M. Newville, ATHENA , ARTEMIS , HEPHAESTUS : data analysis for X-ray absorption spectroscopy using IFEFFIT, *J. Synchrotron Radiat.* 12 (2005) 537–541.  
doi:10.1107/S0909049505012719.
- [119] P.J. Chupas, K.W. Chapman, C. Kurtz, J.C. Hanson, P.L. Lee, C.P. Grey, A versatile sample-environment cell for non-ambient X-ray scattering experiments, *J. Appl.*

- Crystallogr. 41 (2008) 822–824. doi:10.1107/S0021889808020165.
- [120] A. Frenkel, Solving the 3D structure of metal nanoparticles, *Zeitschrift Für Krist. - Cryst. Mater.* 222 (2007). doi:10.1524/zkri.2007.222.11.605.
- [121] A.I. Frenkel, C.W. Hills, R.G. Nuzzo, A View from the Inside: Complexity in the Atomic Scale Ordering of Supported Metal Nanoparticles, *J. Phys. Chem. B.* 105 (2001) 12689–12703. doi:10.1021/jp012769j.
- [122] J.A. McCaulley, In-situ x-ray absorption spectroscopy studies of hydride and carbide formation in supported palladium catalysts, *J. Phys. Chem.* 97 (1993) 10372–10379. doi:10.1021/j100142a018.
- [123] M.W. Tew, J.T. Miller, J.A. van Bokhoven, Particle Size Effect of Hydride Formation and Surface Hydrogen Adsorption of Nanosized Palladium Catalysts: L 3 Edge vs K Edge X-ray Absorption Spectroscopy, *J. Phys. Chem. C.* 113 (2009) 15140–15147. doi:10.1021/jp902542f.
- [124] M.W. Tew, M. Janousch, T. Huthwelker, J.A. van Bokhoven, The roles of carbide and hydride in oxide-supported palladium nanoparticles for alkyne hydrogenation, *J. Catal.* 283 (2011) 45–54. doi:10.1016/j.jcat.2011.06.025.
- [125] J. Wang, Q. Wang, X. Jiang, Z. Liu, W. Yang, A.I. Frenkel, Determination of Nanoparticle

- Size by Measuring the Metal–Metal Bond Length: The Case of Palladium Hydride, *J. Phys. Chem. C*. 119 (2015) 854–861. doi:10.1021/jp510730a.
- [126] D.N. Goldstein, S.M. George, Surface poisoning in the nucleation and growth of palladium atomic layer deposition with Pd(hfac)<sub>2</sub> and formalin, *Thin Solid Films*. 519 (2011) 5339–5347. doi:10.1016/j.tsf.2011.02.037.
- [127] Y. Lei, J. Lu, H. Zhao, B. Liu, K.-B. Low, T. Wu, J.A. Libera, J.P. Greeley, P.J. Chupas, J.T. Miller, J.W. Elam, Resolving Precursor Deligation, Surface Species Evolution, and Nanoparticle Nucleation during Palladium Atomic Layer Deposition, *J. Phys. Chem. C*. 117 (2013) 11141–11148. doi:10.1021/jp401196f.
- [128] A. Gharachorlou, M.D. Detwiler, A. V. Nartova, Y. Lei, J. Lu, J.W. Elam, W.N. Delgass, F.H. Ribeiro, D.Y. Zemlyanov, Palladium Nanoparticle Formation on TiO<sub>2</sub> (110) by Thermal Decomposition of Palladium(II) Hexafluoroacetylacetonate, *ACS Appl. Mater. Interfaces*. 6 (2014) 14702–14711. doi:10.1021/am504127k.
- [129] W. Lin, B.C. Wiegand, R.G. Nuzzo, G.S. Girolami, Mechanistic Studies of Palladium Thin Film Growth from Palladium(II)  $\beta$ -Diketonates. 1. Spectroscopic Studies of the Reactions of Bis(hexafluoroacetylacetonato)palladium(II) on Copper Surfaces, *J. Am. Chem. Soc.* 118 (1996) 5977–5987. doi:10.1021/ja944130h.

- [130] S.G. Rosenberg, M. Barclay, D.H. Fairbrother, Electron Induced Surface Reactions of Organometallic Metal(hfac) 2 Precursors and Deposit Purification, *ACS Appl. Mater. Interfaces*. 6 (2014) 8590–8601. doi:10.1021/am501457h.
- [131] G. Bergeret, P. Gallezot, Particle Size and Dispersion Measurements, in: *Handb. Heterog. Catal.*, Wiley-VCH Verlag GmbH & Co. KGaA, Weinheim, Germany, 2008: pp. 738–765. doi:10.1002/9783527610044.hetcat0038.
- [132] T. Lear, R. Marshall, J.A. Lopez-Sanchez, S.D. Jackson, T.M. Klapötke, M. Bäumer, G. Rupprechter, H.J. Freund, D. Lennon, The application of infrared spectroscopy to probe the surface morphology of alumina-supported palladium catalysts, *J. Chem. Phys.* 123 (2005). doi:10.1063/1.2101487.
- [133] A.K. Santra, D.W. Goodman, Catalytic Oxidation of CO by Platinum Group Metals: From Ultrahigh Vacuum to Elevated Pressures, *Electrochim. Acta*. 47 (2002) 3595–3609. doi:10.1016/S0013-4686(02)00330-4.
- [134] K. Wolter, O. Seiferth, H. Kühlenbeck, M. Bäumer, H.-J. Freund, Infrared spectroscopic investigation of CO adsorbed on Pd aggregates deposited on an alumina model support, *Surf. Sci.* 399 (1998) 190–198. doi:10.1016/S0039-6028(97)00817-0.
- [135] T. Engel, G. Ertl, A molecular beam investigation of the oxidation of CO on Pd(111), *J.*

- Chem. Phys. 69 (1978) 1267–1281. doi:10.1063/1.440501.
- [136] I. Meusel, J. Hoffmann, J. Hartmann, M. Heemeier, M. Bäumer, J. Libuda, H.J. Freund, The interaction of oxygen with alumina-supported palladium particles, *Catal. Letters*. 71 (2001) 5–13. doi:10.1023/A:1016635804185.
- [137] M. Peter, S. Adamovsky, J.M. Flores Camacho, S. Schaueremann, Energetics of elementary reaction steps relevant for CO oxidation: CO and O<sub>2</sub> adsorption on model Pd nanoparticles and Pd(111), *Faraday Discuss.* 162 (2013) 341. doi:10.1039/c3fd00001j.
- [138] T.J. Cassidy, M.D. Allen, Y. Li, M. Bowker, From surface science to catalysis: Surface “explosions” observed on Rh crystals and supported catalysts, *Catal. Letters*. 21 (1993) 321–331. doi:10.1007/BF00769484.
- [139] B.S. Mhatre, V. Pushkarev, B. Holsclaw, T.J. Lawton, E.C.H. Sykes, A.J. Gellman, A window on surface explosions: Tartaric acid on Cu(110), *J. Phys. Chem. C*. 117 (2013) 7577–7588. doi:10.1021/jp3119378.
- [140] L. Crosby, J. Enterkin, F. Rabuffetti, K. Poeppelmeier, L. Marks, Wulff shape of strontium titanate nanocuboids, *Surf. Sci.* 632 (2015) 3–6. doi:10.1016/j.susc.2014.10.014.
- [141] G.D. Rees, B.H. Robinson, Microemulsions and organogels: Properties and novel applications, *Adv. Mater.* 5 (1993) 608–619. doi:10.1002/adma.19930050903.

- [142] I. Danielsson, B. Lindman, The definition of microemulsion, *Colloids and Surfaces*. 3 (1981) 391–392. doi:10.1016/0166-6622(81)80064-9.
- [143] G.H. Brown, ed., *Advances in Liquid Crystals*, Elsevier, 1975.
- [144] L. Dong, H. Shi, K. Cheng, Q. Wang, W. Weng, W. Han, Shape-controlled growth of SrTiO<sub>3</sub> polyhedral submicro/nanocrystals, *Nano Res.* 7 (2014) 1311–1318. doi:10.1007/s12274-014-0495-y.
- [145] B.E. Warren, *X-Ray Diffraction*, Dover Publications, New York, 1990.
- [146] C. Weidenthaler, Pitfalls in the characterization of nanoporous and nanosized materials, *Nanoscale*. 3 (2011) 792. doi:10.1039/c0nr00561d.
- [147] L. Cheng, P. Fenter, M.J. Bedzyk, N.C. Sturchio, Fourier-Expansion Solution of Atom Distributions in a Crystal Using X-Ray Standing Waves, *Phys. Rev. Lett.* 90 (2003) 255503. doi:10.1103/PhysRevLett.90.255503.
- [148] J.S. Okasinski, C.-Y. Kim, D.A. Walko, M.J. Bedzyk, X-ray standing wave imaging of the 1/3 monolayer Sn/Ge(111) surface, *Phys. Rev. B.* 69 (2004) 41401. doi:10.1103/PhysRevB.69.041401.
- [149] N. Chaâbane, R. Lazzari, J. Jupille, G. Renaud, E. Avellar Soares, CO-Induced Scavenging of Supported Pt Nanoclusters: A GISAXS Study, *J. Phys. Chem. C.* 116 (2012)

- 23362–23370. doi:10.1021/jp306496t.
- [150] G. Renaud, R. Lazzari, F. Leroy, Probing surface and interface morphology with Grazing Incidence Small Angle X-Ray Scattering, *Surf. Sci. Rep.* 64 (2009) 255–380. doi:10.1016/j.surfrep.2009.07.002.
- [151] M. Ahmadi, F. Behafarid, B.R. Cuenya, Size-dependent adhesion energy of shape-selected Pd and Pt nanoparticles, *Nanoscale*. 8 (2016) 11635–11641. doi:10.1039/C6NR02166B.
- [152] B.C. Russell, M.R. Castell,  $(13\times 13)R13.9^\circ$  and  $(7\times 7)R19.1^\circ$  reconstructions of the polar SrTiO<sub>3</sub> (111) surface, *Phys. Rev. B - Condens. Matter Mater. Phys.* 75 (2007) 1–7. doi:10.1103/PhysRevB.75.155433.
- [153] M.R. Castell, Scanning tunneling microscopy of reconstructions on the SrTiO<sub>3</sub>(001) surface, *Surf. Sci.* 505 (2002) 1–13. doi:10.1016/S0039-6028(02)01393-6.
- [154] B.L. Henke, E.M. Gullikson, J.C. Davis, X-Ray Interactions: Photoabsorption, Scattering, Transmission, and Reflection at  $E = 50\text{--}30,000$  eV,  $Z = 1\text{--}92$ , *At. Data Nucl. Data Tables*. 54 (1993) 181–342. doi:10.1006/adnd.1993.1013.